

Integrated Nonlinear Photonic Devices

Thesis by
Dong Yoon Oh

In Partial Fulfillment of the Requirements for the
degree of
Doctor of Philosophy

The logo for the California Institute of Technology (Caltech), featuring the word "Caltech" in a bold, orange, sans-serif font.

CALIFORNIA INSTITUTE OF TECHNOLOGY
Pasadena, California

2018
Defended August 11, 2017

© 2018

Dong Yoon Oh

ORCID: 0000-0001-6716-1851

All rights reserved

ACKNOWLEDGEMENTS

Thank you Jesus, my Lord and my Savior, for saving me and bringing me to your light during my senior year at Caltech. Once you met me, I could never be the same person. Thank you for letting me taste the abundant life in you and the joy of following you. I also thank you for carrying me through the years of graduate school, during which I barely scratched the surface of the field of optics and photonics, but I was tremendously blessed to see your wonder. All the praise and glory belong to you.

I thank my advisor Professor Kerry Vahala for his guidance and mentorship throughout my graduate study. In mid-March of 2012, I had the first meeting with Kerry in Watson 234 at Caltech. After praying through the week, I decided to stay at Caltech for another 5 years. Even though his schedule was often filled with meetings, trips and classes, Kerry has always made himself available whenever I wanted to discuss about research with him. It has also been also a privilege for me to work on some of the most exciting photonic devices operating in the nonlinear optics regime. Being involved in a team of research groups developing system-level applications like an optical synthesizer and a two-photon optical clock broadened my views on photonics. One of the highlights at the end of graduate school was the opportunity of visiting the Mauna Kea summit and Keck Observatory with Kerry, his son Jonathan, Seung Hoon and Greg before my postdeadline talk at the 2017 Nonlinear Optics Meeting. Thank you for making my graduate school journey an unforgettable one.

I am very thankful for the opportunities I had to work with Dr. Scott Diddams. I benefited a lot from the breadth and depth of his knowledge in various experiments. I appreciated all his advice, comments and suggestions that he kindly provided. I thank him for having me visit his lab in early 2016 and the privilege to see our silica ridge waveguides in action as well.

I also thank Professor Andrei Faraon and Professor Oskar Painter for their interests and the valuable time to serve in my dissertation committee. Their research contributes to making Caltech one of the most exciting places to do applied physics for graduate students. I also thank Professor Axel Scherer for being my undergraduate thesis advisor in 2010-2011 and serving as a member of the committee. My time in his group was a turning point for me and led me to continue exploring the field of optics and photonics in graduate school.

My gratitude goes out to all my labmates in the Vahala group. Over the past years, I worked closely with Ki Youl Yang on several projects. I learned a lot from his in-depth knowledge of microfabrication and the discussions we had. I thank Seung Hoon Lee for building the first butt-coupling setup in our lab and all the other contributions he made in the integrated UHQ resonator project and the visible soliton project. I would also like to thank Boqiang Shen, who worked together with me in various measurements, modeling and layout designs towards the end of my graduate school years. Yu-Hung Lai has generously spent time to fabricate new taper fibers when I needed them. The advice from Xu Yi and Qi-Fan Yang were helpful for my soliton experiments. I thank Hansuek Lee for fabricating the spiral wedge waveguides and David Sell for his contribution as a SURF student in our first supercontinuum generation project. I thank Myoung-Gyun Suh, Xinbai Li and Heming Wang for being great colleagues.

I thank Pastor Ray and Jackie, who have walked alongside me and always encouraged to seek Jesus above all else. Daniel, Sora, Matthew and Emma have been role models for me as a young believer. The verse "Iron sharpens iron, and one man sharpens another" applies to my friendship with Andre. I praise God for giving me a brother to pray with in the ups and downs. Joel has always been an encouraging brother to me. I'm truly thankful to brother David, Seongho, Peter, Jimmy and John.

I cannot describe with words how blessed I am to be on this journey together with my wife Elaine. I am deeply grateful for her whose love and prayers supported me throughout the years. A few months ago, God gifted us a new life yet to be born. We thank God for his tremendous blessings in our lives.

Lastly, I wouldn't be here today if it weren't for my parents who raised me up with their love and sacrifice. I thank God for my dad and my mom. I also thank God for Siyoon, my one and only sibling and a life-long friend.

ABSTRACT

Chip-scale nonlinear optics can provide important new functions in communications, frequency metrology and spectroscopy. Optical microcavities enhance nonlinear optical effects through resonant recirculation. This recirculation dramatically reduces the required power in applications and also lowers signal noise. A key figure-of-merit is the optical Q factor, which provides a dimensionless scale of optical storage time within the microcavity. In this thesis, a novel integrated ultra-high-Q microcavity with Q as high as 230 million is presented. The device is applied to demonstrate multiple functions including electronic-rate soliton microcomb generation and stimulated Brillouin laser operation. For soliton generation, the resonator must be engineered to produce optical mode families that feature anomalous dispersion. This engineering is applied to generate solitons at wavelengths of 1064 nm and 778 nm. Systems-on-a-chip applications of these devices are discussed including compact optical synthesizers, optical clocks and rotation sensors. Finally, a compact array of silica ridge waveguides is described and applied for efficient and coherent ultraviolet-to-visible comb generation by dispersive-wave generation. Unlike other devices used to broaden spectra such as micro-structured fibers, these arrays provide a wide range of emission wavelength choices on a single chip. The arrays can also enable mode-locked lasers to attain greatly extended spectral reach for spectroscopy, bioimaging, tomography and metrology.

PUBLISHED CONTENT AND CONTRIBUTIONS

- [1] **D. Y. Oh***, K. Y. Yang*, C. Fredrick*, G. Ycas, S. A. Diddams, and K. J. Vahala. “Coherent ultra-violet to near-infrared generation in silica ridge waveguides”. In: *Nature Communications* 8 (2017).
D.Y.O participated in conception of the project, performed the modeling, designed mask layouts, did SEM characterization, assisted in the fabrication, built the 830 nm setup, measured the devices, co-demonstrated the shortest-wavelength-to-date on-chip UV dispersive wave generation, prepared the data and participated in the writing of the manuscript., p. 13922. DOI: 10.1038/ncomms13922.
- [2] S. H. Lee*, **D. Y. Oh***, Q.-F. Yang*, B. Shen*, H. Wang*, K. Y. Yang, Y. H. Lai, X. Yi, X. Li, and K. Vahala. “Towards visible soliton microcomb generation”. In: *Nature Communications* 8 (2017).
D.Y.O participated in the conception of the project, contributed in the modeling and fabrication of devices, built the 778 nm testing setup, measured the devices, demonstrated the soliton microcombs operating at the shortest-wavelength-to-date, prepared the data and participated in the writing of the manuscript. DOI: 10.1038/s41467-017-01473-9.
- [3] D. T. Spencer et al. “An Integrated-Photonics Optical-Frequency Synthesizer”. In: *arXiv preprint arXiv:1708.05228* (2017).
D.Y.O co-invented and developed integrated ultra-high-Q resonators generating electronically-compatible-rate soliton microcombs for optical synthesizer.
- [4] K. Y. Yang*, **D. Y. Oh***, S. H. Lee*, Q.-F. Yang, X. Yi, and K. Vahala. “Bridging ultra-high-Q devices and photonic circuits”. In: *arXiv preprint arXiv:1702.05076* (2017).
D.Y.O participated in the conception of the project, designed mask layouts, contributed to the modeling, measured the devices, co-demonstrated an integrated optical resonator with highest-Q-to-date, the soliton microcomb and stimulated Brillouin laser operation using the integrated devices, prepared the data and participated in the writing of the manuscript.
- [5] **D. Y. Oh**, D. Sell, H. Lee, K. Y. Yang, S. A. Diddams, and K. J. Vahala. “Supercontinuum generation in an on-chip silica waveguide”. In: *Optics letters* 39.4 (2014).
D.Y.O participated in the conception of the project, performed the modeling and the measurement, prepared the data, and participated in the writing of the manuscript., pp. 1046–1048. DOI: 10.1364/OL.39.001046.

*These authors have made equal contributions to the work.

PUBLISHED CONTENT - CONFERENCE PAPERS

- [2] D. Y. Oh*, Q.-F. Yang*, S. H. Lee*, H. Wang*, B. Shen*, K. Y. Yang, Y.-H. Lai, X. Yi, and K. J. Vahala. “Towards Visible Soliton Microcomb Generation”. In: *Nonlinear Optics*. Optical Society of America. 2017, NTh3A–3.
- [3] S. H. Lee*, D. Y. Oh*, K. Y. Yang*, Q.-F. Yang, X. Yi, and K. J. Vahala. “Integrable Soliton Microcomb at Microwave Repetition Rates”. In: *Nonlinear Optics*. Optical Society of America. 2017, NM1A–2.
- [4] C. Frederick, D. Y. Oh, K. Y. Yang, G. Ycas, K. J. Vahala, and S. Diddams. “Silica-Chip-Based Continuum Generation for Frequency Comb Self-Referencing”. In: *Frontiers in Optics*. Optical Society of America. 2016, FTh5G–3.
- [5] D. Y. Oh*, K. Y. Yang*, and K. J. Vahala. “On-chip UV dispersive wave generation”. In: *CLEO: Science and Innovations*. Optical Society of America. 2016, SF2O–4.
- [6] K. Y. Yang*, D. Y. Oh*, S. H. Lee*, and K. J. Vahala. “Ultra-high-q silica-on-silicon ridge-ring-resonator with an integrated silicon nitride waveguide”. In: *CLEO: QELS Fundamental Science*. Optical Society of America. 2016, JTh4B–7.
- [7] D. Y. Oh, D. Sell, H. Lee, K. Y. Yang, S. A. Diddams, and K. J. Vahala. “Supercontinuum generation in a silica spiral waveguide”. In: *CLEO: Science and Innovations*. Optical Society of America. 2014, STh1I–3.

The presenters are underlined.

TABLE OF CONTENTS

Acknowledgements	iii
Abstract	v
Table of Contents	viii
List of Illustrations	x
Chapter I: Introduction	1
1.1 Thesis outline	2
1.2 Nonlinear response of dielectric materials	3
1.3 Pulse propagation in waveguides	5
Chapter II: Integrated Ultra-High-Q Optical Resonators	9
2.1 Abstract	9
2.2 Introduction	9
2.3 Silica ridge resonator design	12
2.4 Design of a single mode silicon nitride waveguide phase-matched to a silica ridge resonator	16
2.5 Fabrication process	19
2.6 Experimental demonstration of waveguide-resonator coupling	21
Chapter III: Demonstration of Nonlinear Optics in Integrated Ultra-High-Q Resonators	24
3.1 Abstract	24
3.2 Introduction	24
3.3 Soliton comb generation	26
3.4 Stimulated Brillouin laser operation	28
3.5 Summary	29
Chapter IV: Towards Visible Microresonator-Based Soliton Frequency Combs	30
4.1 Abstract	30
4.2 Introduction	30
4.3 Dispersion engineering of silica microresonators	35
4.4 Design of soliton devices at pump wavelength 1550 nm, 1064 nm and 778 nm	37
4.5 Soliton frequency comb generation using 1 μ m pump	39
4.6 Soliton frequency comb generation using 778 nm pump	43
4.7 Summary	46
Chapter V: Supercontinuum Generation in Ultra-Low-Loss Silica Waveguides	50
5.1 Abstract	50
5.2 Introduction	50
5.3 Experimental demonstration of supercontinuum generation	50
5.4 Modeling ultra-low-loss silica spiral waveguides	52
Chapter VI: Dispersion-Engineered Photonic Waveguides for Supercontinuum Generation	56

6.1	Abstract	56
6.2	Introduction	56
6.3	Silica ridge waveguide array	59
6.4	Dispersive wave generation	63
6.5	Application: self-referencing of a frequency comb	68
6.6	Spectral measurements	71
6.7	Summary	77
	Bibliography	79

LIST OF ILLUSTRATIONS

<i>Number</i>	<i>Page</i>
2.1 State-of-the-art ultra-high-Q optical microresonator platforms Review of the optical microresonators that have demonstrated highest Q. The intrinsic quality factors (Q_{int}) are plotted versus free spectral range for various resonator material platforms and coupling schemes. The orange background represents the ultra-high-Q regime ($> 10^8$), which previously have been accessible only by prism- or taper-coupled resonators.	11
2.2 Integration of chemically etched silica resonator with a waveguide (a) Schematics of silica wedge resonator. Taper fiber is used for coupling of light into the resonator. (b) Schematics of silica ridge resonator integrated with silicon nitride waveguide. Because of the base silica layer, a waveguide can be monolithically integrated with the resonator.	13
2.3 Calculated quality factor of a wedge resonator as a function of the resonator thickness (a) Intrinsic quality factor (Q_{int}) versus the resonator thickness (t , indicated by the arrows in b) of a silica wedge resonator for the fundamental TE and TM mode families. (b) The fraction of electric field energy near the surface (defined in the text). Calculated mode profiles of the fundamental modes are shown as an inset. The arrows at the electric field intensity maximum represent the direction of the electric field. In general, the TM_1 mode has higher Q factor than the TE_1 mode due to the weaker electric field at the silica-air boundary	14
2.4 Optimization of base silica layer thickness (a) Intrinsic quality factor (Q_{int}) versus base layer thickness (t_2 , indicated by the arrows in b) of a silica ridge resonator for the fundamental TE and TM mode families. (b) Calculated mode profiles of the fundamental modes at $t_2 = 2.5 \mu\text{m}$ and $t_2 = 3.6 \mu\text{m}$	15

- 2.5 **Effective index of the TE₁₁ mode of the silicon nitride waveguide**
 (a) Calculated mode profile of the TE₁₁ mode of the SiN waveguide.
 (b) Calculated effective index (n_{eff}) of the TE₁₁ mode as a function of the waveguide width W and thickness T denoted in **a**. The white solid line indicates the pairs (W, T) for which the effective index of the SiN waveguide matches the effective index (1.438) of the TM1 mode of the silica ridge resonator. 19
- 2.6 **Design of the single mode SiN waveguide** (a) Effective indices of the SiN waveguide modes are plotted as functions of the waveguide width W . The waveguide thickness T is 250 nm. (b) The calculated mode profiles of low-order modes (TE₁₁, TE₂₁, TE₃₁) for the waveguide with $W = 4 \mu\text{m}$ are shown as inset 20
- 2.7 **Fabrication process for integrated ultra-high-Q microresonator**
 (a) Silica disk is defined on silicon by photolithography and HF etching of an initial silica layer. (b) Thermal oxidation grows a second oxide layer beneath the etched silica disk. (c) PECVD silicon nitride is deposited. (d) Silicon nitride waveguide is defined on silica layer by lithography and etching. (e) Lithography and wet etch of the silica define a ring aperture to the silicon substrate. (f) XeF₂ etches the silicon through the ring aperture. 21
- 2.8 **Integrated ultra-high-Q microresonator** (a) Rendering showing silica ridge resonator with nearby silicon nitride waveguide. Fundamental spatial mode is illustrated in color. (b) SEM image of three ridge resonators with a common silicon nitride waveguide (false red color). White arrows show the direction of circulation within the center resonator for the corresponding direction of coupling from the waveguide. Dashed white box is the region for the zoom-in image in 1d. Dashed white line segment gives the location of cleavage plane used for preparation of the SEM image in 1e. (c) Photograph of a single resonator with endfire coupling provided by a lensed fiber (left) and aspheric lens (right). (d) SEM zoom-in image of the waveguide-resonator coupling region shown within the dashed white box in 1b. (e) SEM image of resonator cross section prepared by cleaving at the dashed white line in 1b. 22

2.9	Spectral scan of integrated ridge resonator and ring-down measurement (a) Spectral scan encompassing two free-spectral-ranges. (b) High resolution zoom-in scan for the TM1 and TE1 modes with intrinsic (Q_o) and loaded (Q) quality factors, as well as the linewidth ($\kappa/2\pi$) indicated (M = million). The green sinusoidal signal is a frequency calibration scan using a radio-frequency calibrated fiber Mach-Zehnder interferometer (free-spectral range is 5.979 MHz). (c) Superposition of 10 cavity-ringdown signal scans for the TM1 mode with the corresponding decay time and the loaded and intrinsic Q factors.	23
3.1	Demonstration of detectable repetition rate temporal solitons in an integrated optical microresonator (a) Photograph of a silicon chip with two integrated silica ridge resonators. (b) Measured mode frequencies plotted versus mode number for all the waveguide-coupled cavity modes with linear dispersion removed. (b) Optical spectrum of soliton with pump line indicated. Inset shows the electrical spectrum of the detected soliton pulse stream (RBW: resolution bandwidth) (c) FROG scan of single soliton state in 3b showing the single pulse signal with pulse period of 66.5 ps corresponding to resonator round-trip time.	27
3.2	Demonstration of Brillouin lasing in an integrated optical microresonator Optical spectrum of Brillouin laser. The left inset demonstrates the output laser power vs. input coupled power. These data shows laser threshold behavior and the measured threshold power is as low as 250 μW . The right inset shows RF beat of the back-reflected pump and lasing signal.	28
4.1	Clock wavelengths of single ions and many neutral atoms used in optical clocks. Wavelengths of optical transitions used in the state-of-the-art optical atomic clocks. Two-photon absorption wavelength (778 nm) of rubidium is also indicated, as the wavelength that is being explored for compact secondary time standards.	31

- 4.2 **Effective index of fundamental TM mode (TM1) of silica wedge resonators for various thickness t** Effective index of TM1 mode of the resonator versus wavelength is plotted for various thickness t . The dashed line is the refractive index of fused silica based on the Sellmeier equation. A schematics of silica wedge resonator is shown as an inset to the figure. 34
- 4.3 **Calculated dispersion of the TM1 mode** (a) Total dispersion(β_2) is plotted versus wavelength for various t . The dashed line indicates the material dispersion of silica (b) Geometrical dispersion($\beta_{2,geo}$), defined as the total dispersion(β_2) subtracted by the material dispersion of silica dispersion(β_{2,SiO_2}) 34
- 4.4 **Calculated electric field intensity of TM1 mode of the resonator for various thickness t and wavelengths λ** . Mode field intensity for $t = 8, 4, 2 \mu\text{m}$ and $\lambda = 400, 600, 800, 1000 \text{ nm}$ is shown. The wedge angle is fixed at 30 degree for these simulations. At small t and/or large λ , the radial position of the mode intensity maximum moves out of the wedge, and its vertical position does not change any more. In this regime, the geometrical dispersion of the mode is anomalous (See the main text for further details). 36
- 4.5 **Fabricated silica wedge resonator devices that feature anomalous dispersion at pump wavelength 1550 nm, 1064 nm and 778 nm.** (a) Regions of normal and anomalous dispersion are shown versus silica resonator thickness (t) and pump wavelength. The zero dispersion wavelength (λ_{ZDW}) for the TM1 mode appears as a blue curve. Plot is made for a 3.2-mm-diameter silica resonator. Three different device types I, II and III (corresponding to three oxide thicknesses) are indicated for soliton generation at 1550 nm, 1064 nm and 778 nm. (b) Cross-sectional SEM images of the fabricated resonators. White scale bar is $5 \mu\text{m}$ 38
- 4.6 **Measured Q factors and comb threshold powers versus thickness and pump wavelength for the three device types.** Effective mode area (A_{eff}) of the TM1 mode family is also plotted as a function of wavelength and thickness. 39

- 4.7 **Soliton frequency combs at pump wavelength 1550 nm, 1064 nm and 778 nm** Soliton frequency comb spectra measured using device types I, II and III designed for pump wavelengths 1550 nm, 1064 nm, and 778 nm, respectively. Pump frequency location is indicated by a dashed vertical line. The soliton pulse repetition rate of all devices is about 20 GHz. Insets: cross-sectional SEM images of the fabricated resonators. White scale bar is 5 μm 40
- 4.8 **Microresonator dispersion engineering at 1064 nm.** (a) Simulated dispersion (GVD) of TM mode families versus resonator thickness. The angle of the wedge ranges from 30° to 40° in the colored regions. Measured data points are indicated and agree well with the simulation. (b) Measured relative mode frequencies (blue points) plotted versus relative mode number of a soliton-forming TM1 mode family in a 3.4 μm thick resonator. The red curve is a parabolic fit yielding $D_2/2\pi=3.3$ kHz. 41
- 4.9 **Experimental setup for soliton generation.** A continuous-wave (CW) fiber laser is modulated by an electro-optic phase modulator (PM) before coupling to a ytterbium-doped-fiber-amplifier (YDFA). The pump light is then coupled to the resonator using a tapered fiber. Part of the comb power is used to servo-lock the pump laser frequency. FBG: fiber Bragg grating. PD: photodetector. PC: polarization controller. 42
- 4.10 **Soliton generation at 1064 nm.** Optical spectra of solitons at 1064 nm generated from the mode family shown in 4.8 (b). The two soliton spectra correspond to different power levels with the blue spectrum being a higher power and wider bandwidth soliton. The dashed vertical line shows the location of the pump frequency. The solid curves are sech^2 fittings. Inset: typical detected electrical beatnote showing soliton repetition rate. RBW: resolution bandwidth. 42

- 4.11 **Mode hybridization at 778 nm illustrated by the effective indices of the resonator modes** (a) Calculated effective indices for TE1, TE2, TM1 and TM2 modes at 778 nm plotted versus thickness for a silica resonator with reflection symmetry. The TM1 and TE2 modes cross each other without hybridization. The dashed box is the frame for the panel **b** zoom-in. (b) Zoom-in of the dashed box in panel **a**. Inset shows resonator with reflection symmetry (equivalent to wedge angle $\theta = 90^\circ$). (c) As in **b** but for resonator with $\theta = 40^\circ$. An avoided crossing of TM1 and TE2 occurs due to mode hybridization. 43
- 4.12 **Calculated GVD of the two hybrid modes for $\theta = 40^\circ$.** Hybridization causes a transition in the dispersion around the thickness $t_{tr} = 1.48\mu\text{m}$. The points are the measured dispersion values. 44
- 4.13 **Measured mode frequencies of the hybrid modes** (a) Measured relative mode frequencies of the TM1 and TE2 mode families versus relative mode number μ for devices with $t = 1.47$. The thickness is below the transition thickness t_{tr} and the TM1 mode is anomalous. (b) As in **a** but for $t = 1.49\mu\text{m}$. The thickness is above the transition thickness t_{tr} and the TE2 mode is anomalous. 44
- 4.14 **Experimental setup for soliton generation at 778 nm.** A 1557 nm tunable laser is sent to a quadrature phase shift keying modulator (QPSK) to utilize frequency-kicking[117] and is then amplified by an erbium-doped-fiber-amplifier (EDFA). Then, a periodically poled lithium niobate (PPLN) waveguide frequency doubles the 1557 nm input into 778 nm output. The 778 nm pump light is coupled to the resonator for soliton generation. A servo loop is used to maintain pump locking[78]. 45

- 4.15 **First soliton microcomb demonstration at 778 nm** (a) Measured mode frequencies of the TM1 mode family plotted versus wavelength for a $t = 1.47 \mu\text{m}$ device. The pump wavelength is indicated as a dashed line. The spurs in the data are due to the crossing with other mode families. (b) Optical spectrum of a soliton with pump line (778.7 nm) indicated. The red curve is a simulation using the Lugiato-Lefever equation including the Raman terms, which deviates slightly from the sech^2 envelope due to the higher order dispersion. The spectral location of observed dispersive waves match well with the mode crossing locations in **a**, revealing that the dispersive waves are induced by spatial mode-interactions[[yang2016spatial.](#)] Inset shows the electrical spectrum of the detected soliton pulse stream. 48
- 4.16 **Generation of a soliton microcomb that spans wavelengths 755 - 793 nm.** (a) Measured mode frequencies of the TM1 mode family plotted versus wavelength for a $t = 1.50 \mu\text{m}$ device. (b) Optical spectrum of a soliton with pump line (778.7 nm) indicated. The red curve is a simulation using Lugiato-Lefever equation including the Raman terms. Inset shows the electrical spectrum of the detected soliton pulse stream. 49
- 5.1 **Low-loss, silica-on-silicon waveguide and experimental setup.** (a) Photograph of the sample showing four, cascaded spiral waveguides. (b) Experimental setup for supercontinuum generation and characterization using the silica waveguide. OPO: optical parametric oscillator; OSA: optical spectrum analyzer. (c) Close-up view of the optical coupling stage, imaging objectives and spiral waveguide chip. 51
- 5.2 **Spectral broadening in the fundamental TM mode measured at a series of pulse energies.** The blue curves are measured spectra, and the dashed curves in light blue are spectra from the simulation. . 53
- 5.3 **Calculated dispersion and nonlinearity of the fundamental TM mode at a series of bending radii that occur at the inner and outer waveguides within each spiral.** 54
- 6.1 **Overview of on-chip waveguide platforms for supercontinuum generation.** The spectral extents of supercontinua of light generated in various waveguide platforms are shown. It does not include all the supercontinuum waveguides reported in the literature as the body of the work in the field continues to grow. 57

- 6.2 **Silica ridge waveguide structure.** Scanning electron microscope images of an array of silica ridge waveguides on a silicon chip. Silicon pillars support silica layers containing waveguides. The red box in panel (a) contains a silica waveguide whose cross section is shown as the inset. The cross section shows the calculated mode profile of the TM mode at wavelength 830 nm superimposed. Scale bar is 100 μm for (a) and 1 μm for the inset. 58
- 6.3 **Ridge waveguide array microfabrication process.** (a) Photolithography on thermal silica layer. Mask width is denoted by the double-arrow line. (b) HF wet-etching to define silica ridge. (c) Additional oxide layer is grown by thermal oxidation. (d) Supporting structure is patterned by photolithography. (e) HF wet-etching creates striped openings in the silica layer. (f) Isotropic etching of the silicon (XeF_2) is performed to undercut the silica layer. (g) Rendering of final ridge waveguide array structure. Dependence of ridge dimension on mask width is shown in Figure 6.4. 60
- 6.4 **Dependence of ridge dimension on mask width** (a) SEM images of a series of ridges in a fabricated silica waveguide array. The thickness of the base silica layer is 0.45 μm . Scale bar is 1 μm . The definition of ridge height(H) and ridge width(w) is shown in the panel. (b) Measured ridge dimensions based on SEM images as a function of mask width 61
- 6.5 **Dispersion engineering of ridge waveguides.** (a) Calculated mode area and zero dispersion wavelength (λ_{ZDW}) are plotted versus the ridge base width. (b) Calculated mode area and zero dispersion wavelength (λ_{ZDW}) are plotted versus the ridge base width. Calculated group velocity dispersion (GVD, dashed lines) and phase-matching parameter $\Delta\beta$ (solid lines) for dispersive wave generation in TM polarization are plotted versus wavelength. Blue, red and yellow solid and dashed lines correspond to mode areas of 0.83 μm^2 , 1.03 μm^2 , 1.69 μm^2 respectively. The phase matching condition $\Delta\beta = \frac{1}{2}\gamma P_p$ (830 nm pump) is satisfied at the intersections of the colored solid lines and the black dashed line. The points with error bars are measured dispersion values obtained from sets of ten scans of spectral fringes measured using a Mach-Zehnder interferometer (see the text). 62

- 6.6 **Phase-matching dispersive wave wavelength in a waveguide array.** Calculated TM dispersive wave wavelength (λ_{DW}) as a function of pump wavelength and ridge width is plotted as a colormap for the waveguide array chip used in Figure 6.8e. The black lines are the zero crossing of the group velocity dispersion ($\lambda_{ZDW,1}$ and $\lambda_{ZDW,2}$). The white area is where dispersive waves do not exist. 64
- 6.7 **Experimental setup for supercontinuum generation using a titanium sapphire laser centered at 830 nm.** The pulses entering the ridge waveguides have FWHM temporal width of 60 fs. 65
- 6.8 **Direct observation of dispersive wave generation** UV-visible dispersive wave generation in a silicon chip containing an array of waveguides with varying mode area (322 nm emission has area of $0.83 \mu\text{m}^2$ and 545 nm emission has area of $2.09 \mu\text{m}^2$) is directly observed. Image represents a photographs of scattered light taken from above the 1.5 cm long chip in which infrared pulses are launched at the left side of each waveguide. Pulse energies are set to the threshold pulse energy for dispersive wave generation. The color emission at the left side of the image is dispersive wave emission that has been reflected at the far right facet of the chip. The initial spectral broadening of the input pulse can be seen as the orange-red emission that gradually shifts diagonally upward right. The visible scattered light shown in the figure is a very small amount of the total generated. The vast majority of the light is forward propagating and collected into a multimode fiber (not shown). 66

- 6.9 Numerical simulation of pulse propagation in the waveguide and comparison with measurement.** (a) Calculated continuum spectra as a function of waveguide position at a coupled pulse energy of 330 pJ. The pulse is launched in the TM mode of the waveguide with mode area $0.76 \mu\text{m}^2$. The color bar (inset) applies to panels (a), (c), (d) and (e). (b) Top-view photographs of scattered light from the surface of the waveguide. The photographs were taken at pulse energies ranging from 330 pJ to 1100 pJ (left to right side). As indicated by the dashed line, the pulse travels in the waveguide from the bottom to the top of the image. Dispersive wave generation occurs in the UV and is therefore not visible in the image. The grey line superimposed on the photographs is the length at which dispersive wave generation occurs as predicted by the simulation. The spectral breathing of the input pulse results in a periodically visible orange-red emission that correlates with the calculation. (c) Calculated continuum spectra as a function of waveguide position at a pulse energy of 1100 pJ. (d-e) Calculated spectrograms of the optical pulse propagating in the waveguide corresponding to (c). The spectrogram in (d) is at waveguide position 0.16 cm where dispersive wave is generated. The spectrogram in (e) is at the waveguide output. 67
- 6.10 Application of dispersive wave engineering to self-referencing a Yb fiber laser frequency comb.** (a) Experimental setup for measuring f_{ceo} of the Yb fiber laser. The ridge waveguide has a mode area $3.13 \mu\text{m}^2$ and length 1.50 cm. (b) Photograph of the emitted light dispersed through a prism and reflected on a white screen. Scale bar is 5 cm. (c) Measured optical spectrum of the collimated beam at the output facet of the waveguide. The coupled pulse energy is 2300 pJ and the input spectrum is shown in black. (d) Spectra of the dispersive wave (DW, blue) and second harmonic light (SH, black) filtered by a bandpass filter. (e) Radio-frequency spectrum measured with an electrical spectrum analyzer (ESA) shows the pulse repetition rate f_{rep} and the carrier-envelope-offset beat frequency $f_{\text{ceo},1}$ and $f_{\text{ceo},2}$. The resolution bandwidth (RBW) is 300 kHz. 68

- 6.11 **Calculated temporal delay of the pulse used for f-2f measurement.**
 (a) Relative group delay between TE and TM mode at the end of the waveguide of length 1.5 cm. Delay is set to 0 for TE mode at the pump wavelength of 1064 nm. The dashed line is located at the pump wavelength of 1064 nm. (b) Spectrogram of the TE portion of the pulse at the end of the waveguide. As in panel (a), y-axis represents the relative group delay with respect to the group delay at the pump wavelength 1064 nm 70
- 6.12 **Supercontinuum spectra generated in the TE and TM mode of the waveguides.** Supercontinuum spectra for a series of ridge waveguides on a single waveguide array chip shown in Figure 6.8 when the titanium sapphire laser pulse is coupled to the TM mode (blue line) and TE mode (red line) of the waveguides. The coupled pulse energy is 1000 pJ. The mode area of the waveguide is indicated in the panel. All the continuum spectra are normalized such that the areas under the spectra are the same. 72
- 6.13 **Precisely tuned and efficient emission of dispersive waves in the UV-visible wavelengths.** (a) Measured tuning of the dispersive wave peak wavelength (λ_{DW}) by lithographic control of the waveguide mode effective area. The data are taken for a pulse energy at the dispersive wave generation threshold. The solid line is the phase matching condition obtained from FEM simulations. (b) Scatter plot of measured conversion efficiency (left axis) and dispersive-wave average power (right axis) versus the dispersive wave peak wavelength for the waveguide array in Figure 6.8. Blue and red markers correspond to the TM mode and the TE mode. The coupled pulse energy is 1000 pJ. 73
- 6.14 **Measured UV dispersive wave spectra and the conversion efficiency.** The TM mode dispersive wave spectra(lines) and the conversion efficiency (solid circles) are shown for the waveguides of various mode area in a waveguide array chip with the under layer thickness 310 nm 74

- 6.15 **Waveguide deformation and its remedy by annealing (a-c)** SEM images showing the deformation at the position where soliton fission point occurs. The waveguide of mode area $0.86 \mu\text{m}^2$ was used and the dispersive wave peak was located at 345 nm. **(d)** Continuous measurement of UV power generated from an annealed waveguide of similar dimension as in **a-c**. A fresh waveguide without deformation was annealed at 1000 degree for 24 hr. The average coupled power was 41 mW. 75
- 6.16 **265 nm generation.** Measured dispersive wave spectra in deep UV when the Yb laser pulse is launched into the TM mode of 0.75 cm-long ridge waveguides having mode areas of $1.09 \mu\text{m}^2$ (green) and $1.12 \mu\text{m}^2$ (black). The coupled pulse energy is 2000 pJ. 76
- 6.17 **Spiral silica ridge waveguides.** **(a)** Photographs of silica ridge waveguides of various lengths (from the bottom left to the bottom right: 10 cm, 15 cm, 40 cm). **(b)** Photograph of a 40 cm-long spiral ridge waveguide generating a white-light supercontinuum. **(c)** The spectrum of the generated supercontinuum using the device shown in **b**. 77

Chapter 1

INTRODUCTION

From the birth of computers in the late 1930s, the evolution of the electronics and the communication systems has dramatically affected people's lives in the past century. The time period is marked by the invention of transistors in 1947, the integrated circuit in 1958, the beginning of the world wide web in 1990 and is now facing the dawn of 5th generation wireless systems (5G). The impact of the photonics on the society has also significantly grown since the invention of laser in the 1960. In areas like biomedical imaging, medical surgery or manufacture, lasers have often found unprecedented applications due to the high coherence, directionality and power of the light they produce and the fact that their wave properties can be precisely controlled. The photonics also played a crucial role in the aforementioned historical advances. For instance, the birth of the fiber-optic communication in 1966 eventually led to the global deployment of fiber optic cables serving as the backbone of the high speed internet in the world wide web era.

An optical frequency comb (OFC), which emerged in 1999 - 2000 as a result of the union of ultrafast and ultra-stable laser technology, is a set of optical frequencies with equidistant spacing sharing the common phase and thereby producing temporal pulses in the time domain. It can be viewed as the collection of thousands of laser lines with constant spectral separation having coherent oscillations. Those laser lines are provided by a single laser consisting of a broadband gain medium, an optical cavity and a saturable absorber providing a mode-locking mechanism. OFCs have revolutionized the precision metrology and proven to enable the most precise time-keeping system on earth, the optical atomic clock. The fractional uncertainties of the best optical atomic clocks now reach the level of 1 over 10^{17} [1]. Such precise clocks can be used in geodesy and high resolution global positioning system (GPS). OFCs also bring critical advances in many of the areas where optics and photonics have traditionally played vital roles including spectroscopy, astronomy, bioimaging and high-speed telecommunications. Furthermore, it works as a gear box between the microwave and the optical frequencies, providing the ability to control and synthesize the optical frequencies using the electronics[2].

While the conventional OFCs are still pushing the boundary of the fundamental

science and optical technologies, the past decade has seen the rise of keen interests in miniaturizing such systems to chip-scale. Integrated photonic and optoelectronic chips have potentials for low-cost, scalable production as well as ready controls by users and will bring the diverse functionalities of OFCs out of labs. A powerful smartphone-size device that has various precision sensing capabilities and time-keeping function in the absence of GPS reception can be envisioned. Miniaturized combs can also be set up in environments that have stringent power and size requirements like telescopes for astronomical calibration[3] or spacecrafts for space-borne measurements[4]. They might also be integrated with the electronics in the data centers for petabit-per-second high-speed data transmission[5], meeting the rising demand from the ever-increasing volumes of data stored and transferred in cloud-based systems.

In this thesis, novel silicon chip-based devices that can serve as parts of the proposed integrated photonic systems are designed and tested.

1.1 Thesis outline

Chapter II introduces an integrated ultra-high-Q resonator achieving the record-high Q factor of 230 million. The silica ridge ring resonator is monolithically integrated with PECVD silicon nitride waveguide using standard microfabrication processes. The design, fabrication and characterization of the device are discussed.

Chapter III shows the multi-functionalities of the integrated UHQ resonator by demonstrating the electronics-compatible-rate (15 GHz) soliton microcomb and low-threshold Brillouin laser operation using the device. Both are the first demonstrations among the integrated microresonator platforms.

Chapter IV focuses on the progress made towards the visible soliton microcomb generation. A simple method of engineering the dispersion of the cavity is used to broaden the window of available pump wavelengths for bright soliton generation. 20 GHz soliton microcombs are generated using the pump at 1 μm and 778 nm. The shortest wavelength soliton-to-date is demonstrated covering the 755 - 790 nm band.

Chapter V shifts the gear to the supercontinuum generation in on-chip silica waveguides. Supercontinuum generation in a 3.5-m long spiral waveguide is demonstrated and modelled using GNLSE.

Chapter VI presents "designer" photonic waveguides for coherent dispersive wave generation from the UV to visible wavelengths. An array of silica ridge wave-

uicides are fabricated in a compact silicon chip, providing hundreds of choices of wavelengths. An application of the device in self-referencing of 1 μm laser comb is demonstrated.

1.2 Nonlinear response of dielectric materials

Nonlinear polarization

When an electric field is applied to a medium, the medium is polarized in the following manner

$$\mathbf{P}(t) = \epsilon_0 \chi_{\text{eff}} \mathbf{E}(t) \quad (1.1)$$

where $\mathbf{E}(t)$ is the electric field, $\mathbf{P}(t)$ is the polarization, ϵ_0 is the vacuum permittivity and χ_{eff} is the effective susceptibility. In the case where the applied electric field is small enough, the polarization is proportional to the electric field and the effective susceptibility simply equals the linear susceptibility ($\chi_{\text{eff}} = \chi^{(1)}$). This is true in the regime of linear optics where the light intensity is small and the media that the light encounters or propagates through respond linearly. In a linear optical system, the frequencies of emitted light remain unchanged as they travel in media. For example, the optical frequency of monochromatic light passing through optical component like an optical lens or beam splitter stays constant.

In general, however, the response of dielectric media to the applied electric field has both the linear and nonlinear part. The nonlinear contribution becomes more pronounced when the electric field is stronger. In the absence of permanent dipole moments, the polarization can be described in the following power series expansion:

$$\begin{aligned} \mathbf{P}(t) &= \epsilon_0 [\chi^{(1)} \mathbf{E}(t) + \chi^{(2)} \mathbf{E}^2(t) + \chi^{(3)} \mathbf{E}^3(t) + \dots] \\ &= \mathbf{P}^{(1)}(t) + \mathbf{P}^{(2)}(t) + \mathbf{P}^{(3)}(t) + \dots \end{aligned} \quad (1.2)$$

where $\chi^{(n)}$ is the n -th order susceptibility represented as a n -th order tensor and $\mathbf{P}^{(n)}(t) \equiv \epsilon_0 \chi^{(n)} \mathbf{E}^n(t)$ is the n -th order nonlinear polarization. Equation 1.2 can be rewritten in terms of components of the electric field, polarization vectors and the nonlinear susceptibility tensors as follows:

$$P_i = \epsilon_0 [\chi_i^{(1)} E_i + \chi_{ij}^{(2)} E_i E_j + \chi_{ijk}^{(3)} E_i E_j E_k + \dots] \quad (1.3)$$

where $\chi^{(n)}$ is the n -th order susceptibility represented as a n -th order tensor.

For a centrosymmetric medium (a material system that has the inversion symmetry), all the even order nonlinear susceptibilities vanish. This can be easily seen by substituting \mathbf{E}, \mathbf{P} by $-\mathbf{E}, -\mathbf{P}$ in Equation 1.2, requiring that the polarization in the opposite direction will result if an electric field of opposite direction is applied. For example, in the case of second-order polarization, the following holds true for a centrosymmetric medium:

$$\begin{aligned} P_i^{(2)} &= \chi_{ij}^{(2)} E_i E_j \\ -P_i^{(2)} &= \chi_{ij}^{(2)} (-E_i)(-E_j) \end{aligned} \quad (1.4)$$

As a result, $\chi^{(2)} = 0$ and the material system cannot exhibit nonlinear optical processes originating from the second order susceptibility, which include second harmonic generation, sum-frequency generation, difference-frequency generation and optical parametric amplification.

Therefore, the third order nonlinearity is the lowest order nonlinearity possessed by a centrosymmetric medium and it is the cause of the most of the observed nonlinear optical processes.

Nonlinear optical processes arising from the third order nonlinearity

To examine the nonlinear optical processes that result from the third order nonlinear susceptibility universally present in most materials, let us examine the third order polarization : $P^{(3)}(t) = \epsilon_0 \chi^{(3)} E^3(t)$. The equation is written in a scalar form for simplicity of the following discussion. Let us assume that the electric field consists of three frequency components $\omega_1, \omega_2, \omega_3$ and can be written as

$$E(t) = \sum_{n=1}^3 [E(\omega_n) e^{-i\omega_n t} + E(\omega_n)^* e^{i\omega_n t}] \quad (1.5)$$

The polarization $P^{(3)}(t)$ then has following terms:

$\chi^{(3)} E(\omega_p) ^2 E(\omega_p) e^{-i\omega_p t}$	Self-phase modulation
$\chi^{(3)} E(\omega_p) ^2 E(\omega_q) e^{-i\omega_q t}$	Cross-phase modulation
$\chi^{(3)} E(\omega_p)^3 e^{-i(3\omega_p)t}$	Third harmonic generation
$\chi^{(3)} E(\omega_p) E(\omega_q) E(\omega_r) e^{-i(\omega_p + \omega_q + \omega_r)t}$	Non-degenerate Four-wave mixing
$\chi^{(3)} E(\omega_p) E(\omega_q) E(\omega_r)^* e^{-i(\omega_p + \omega_q - \omega_r)t}$	Non-degenerate four-wave mixing
$\chi^{(3)} E(\omega_p)^2 E(\omega_q) e^{-i(2\omega_p + \omega_q)t}$	Degenerate four-wave mixing
$\chi^{(3)} E(\omega_p)^2 E(\omega_q)^* e^{-i(2\omega_p - \omega_q)t}$	Degenerate four-wave mixing

where p, q, r can be any integer from 1 to 3 and p, q, r have different values from one another. The corresponding nonlinear optical processes include self-phase modulation, cross-phase modulation, third harmonic generation and four-wave mixing, which are indicated above.

In cases where the frequencies of the applied electric field are far off from the resonance frequencies of atoms or molecules, the components of the third order nonlinear susceptibility tensor in each term above can be calculated in a quantum mechanical model using the Schrödinger equation. There, we consider the interaction Hamiltonian $\hat{V}(t) = -\hat{\boldsymbol{\mu}} \cdot \mathbf{E}(t)$ where $\hat{\boldsymbol{\mu}} = -e\hat{\mathbf{r}}$ is the electric dipole moment. Treating this interaction Hamiltonian as a perturbation, one can derive a recursive series of equations for eigenfunctions. Then, the third order susceptibility can be calculated using the expectation value of the dipole moment per atom correct to the third order in perturbation theory. The formalism describes well the nonlinearities arising from the nonresonant electronic response of bound electrons, which are present in all the dielectric materials.

For a detailed discussion of the tensor nature of the nonlinear susceptibilities and their calculation using the perturbation theory, please see the work by Boyd[6].

1.3 Pulse propagation in waveguides

The derivation of Generalized Nonlinear Schrödinger Equation is taken from Agrawal, 2007.

An optical waveguide is a device in which the optical field is confined and propagates along a certain direction. The propagation of optical fields in waveguides is governed by Maxwell's equation:

$$\begin{aligned}\nabla \times \mathbf{E} &= -\frac{\partial \mathbf{B}}{\partial t}, \\ \nabla \times \mathbf{H} &= \mathbf{J} + \frac{\partial \mathbf{D}}{\partial t}, \\ \nabla \cdot \mathbf{D} &= \rho_f \\ \nabla \cdot \mathbf{B} &= 0\end{aligned}\tag{1.6}$$

where $\mathbf{E}(\mathbf{H})$ is the electric(magnetic) field, $\mathbf{D}(\mathbf{B})$ is the electric(magnetic) field density, \mathbf{J} is the current density and ρ_f is the charge density. In optical waveguides without free carriers, $\mathbf{J} = \rho_f = 0$.

Taking curl of the first equation and substituting \mathbf{D} by $\epsilon_0\mathbf{E} + \mathbf{P}_L + \mathbf{P}_{NL}$ where \mathbf{P}_L and \mathbf{P}_{NL} are the linear and nonlinear part of the polarization, respectively,

$$\nabla \times \nabla \times \mathbf{E} + \frac{1}{c^2} \frac{\partial^2 \mathbf{E}}{\partial t^2} + \mu_0 \frac{\partial^2 \mathbf{P}_L}{\partial t^2} + \mu_0 \frac{\partial^2 \mathbf{P}_{NL}}{\partial t^2} = 0 \quad (1.7)$$

where we used the relation $c^2 = \frac{1}{\epsilon_0\mu_0}$. Now, consider a pulse that propagates in a waveguide mode that is polarized along \hat{x} -axis. Assuming that the pulse width is at least tens of optical cycles, we can use the slowly varying envelope approximation and write the electric field as $\mathbf{E}(\mathbf{r}, t) = \frac{1}{2} \hat{x} [E(\mathbf{r}, t) e^{-i\omega_0 t} + c.c.]$, where $E(\mathbf{r}, t)$ is the slowly varying envelope and ω_0 is the center frequency of the pulse.

Now, we Fourier-transform this equation into the frequency domain to obtain the Helmholtz equation:

$$(\nabla^2 + \epsilon(\omega) \frac{\omega^2}{c^2}) \tilde{E}(\mathbf{r}, \omega) = 0 \quad (1.8)$$

We use the following separation of variables to solve for Equation 1.8.

$$\tilde{E}(\mathbf{r}, \omega - \omega_0) = F(x, y) \tilde{A}(z, \omega - \omega_0) e^{i\beta_0 z} \quad (1.9)$$

where $\beta_0 \equiv \beta(\omega_0)$. Plugging Equation 1.9 into Equation 1.8,

$$\frac{\partial^2 F}{\partial x^2} + \frac{\partial^2 F}{\partial y^2} + 2iF\beta_0 \frac{\partial \tilde{A}}{\partial z} e^{i\beta_0 z} + (\epsilon(\omega) \frac{\omega^2}{c^2} - \beta_0^2) F \tilde{A} e^{i\beta_0 z} \quad (1.10)$$

Dividing Equation 1.10 by $F \tilde{A} e^{i\beta_0 z}$,

$$\frac{1}{F} \left(\frac{\partial^2 F}{\partial x^2} + \frac{\partial^2 F}{\partial y^2} \right) + \frac{2i\beta_0}{\tilde{A}} \frac{\partial \tilde{A}}{\partial z} + \epsilon(\omega) \frac{\omega^2}{c^2} - \beta_0^2 = 0 \quad (1.11)$$

We define $\tilde{\beta}(\omega)$ such that

$$\tilde{\beta}(\omega)^2 = \frac{1}{F} \left(\frac{\partial^2 F}{\partial x^2} + \frac{\partial^2 F}{\partial y^2} \right) + \epsilon(\omega) \frac{\omega^2}{c^2} \quad (1.12)$$

Then, it follows from Equation 1.11 that

$$-\tilde{\beta}(\omega)^2 = \frac{2i\beta_0}{\tilde{A}} \frac{\partial \tilde{A}}{\partial z} - \beta_0^2 \quad (1.13)$$

Equation 1.12 and 1.13 can be rewritten as

$$\begin{aligned} \frac{\partial^2 F}{\partial x^2} + \frac{\partial^2 F}{\partial y^2} + (\epsilon(\omega) \frac{\omega^2}{c^2} - \beta(\tilde{\omega})^2) F &= 0 \\ \frac{2i\beta_0}{\tilde{A}} \frac{\partial \tilde{A}}{\partial z} + (\tilde{\beta}(\omega)^2 - \beta_0^2) \tilde{A} &= 0 \end{aligned} \quad (1.14)$$

The dielectric constant $\epsilon(\omega)$ can be written as $\epsilon(\omega) = (n + \Delta n)^2$ where n is the linear refractive index given by $n = \sqrt{1 + \chi^{(1)}}$. Δn includes contribution from the loss as well as the nonlinearity of the material. We consider the case in which the waveguide is made of $\chi^{(3)}$ -material and make the following approximation: $\Delta n \sim \tilde{n}_2 |E|^2 + i \frac{\alpha(\omega)}{2k_0}$ where $k_0 = \frac{2\pi}{\lambda_0} = \frac{\omega_0}{2\pi c}$ and $\alpha(\omega)$ is the loss of the waveguide at frequency ω . We treat Δn as a small perturbation and use the first-order perturbation theory to find the correction to the eigenvalue : $\beta(\omega) = \beta(\omega) + \Delta(\beta(\omega))$ where the correction is given by

$$\begin{aligned} \Delta\beta(\omega) &= \frac{\omega^2 n(\omega)}{c^2 \beta(\omega)} \frac{\iint_{-\infty}^{\infty} \Delta n(\omega) |F(x, y)|^2 dx dy}{\iint_{-\infty}^{\infty} |F(x, y)|^2 dx dy} \\ &= \frac{\omega}{c} \frac{\iint_{-\infty}^{\infty} \Delta n(\omega) |F(x, y)|^2 dx dy}{\iint_{-\infty}^{\infty} |F(x, y)|^2 dx dy} \\ &= i \frac{\tilde{\alpha}(\omega)}{2} + \frac{\omega \tilde{n}_2}{c} |\tilde{A}(z, \omega - \omega_0)|^2 \frac{\iint_{-\infty}^{\infty} |F(x, y)|^4 dx dy}{\iint_{-\infty}^{\infty} |F(x, y)|^2 dx dy} \end{aligned} \quad (1.15)$$

The second and third line of Equation 1.15 are obtained by using $\beta(\omega) = n(\omega) \frac{\omega}{c}$.

With the approximation $\beta(\tilde{\omega})^2 - \beta_0^2 = (\tilde{\beta}(\omega) + \beta_0)(\tilde{\beta}(\omega) - \beta_0) \sim 2\beta_0(\tilde{\beta}(\omega) - \beta_0)$, it follows that

$$\frac{\partial \tilde{A}}{\partial z} = i(\tilde{\beta}(\omega) - \beta_0) \tilde{A} = i(\beta(\omega) + \Delta\beta(\omega) - \beta_0) \tilde{A} \quad (1.16)$$

Now, Equation 1.15 and lead to

$$\frac{\partial \tilde{A}}{\partial z} = -\frac{\tilde{\alpha}}{2} \tilde{A} + i(\beta(\omega) - \beta_0) \tilde{A} + i\gamma |\tilde{A}|^2 \tilde{A} \quad (1.17)$$

where γ , the nonlinearity of the waveguide, is defined as

$$\gamma(\omega) = \frac{\omega \bar{n}_2 \iint_{-\infty}^{\infty} |F(x, y)|^4 dx dy}{c \iint_{-\infty}^{\infty} |F(x, y)|^2 dx dy} \quad (1.18)$$

So far in our derivation, we have assumed that the nonlinear response of materials to incident optical field is instantaneous. However, in reality, ultrashort pulses cause delayed nonlinear responses from the material due to the Raman effect. The physical origin of the Raman effect is the molecular vibration of materials. Including the Raman response of silica,

$$\frac{\partial \tilde{A}}{\partial z} = -\frac{\tilde{\alpha}}{2} \tilde{A} + i(\beta(\omega) - \beta_0) \tilde{A} + i\gamma \mathcal{F}(\tilde{A} \int_0^{\infty} R(t') |A(z, t - t')|^2 dt') \quad (1.19)$$

where \mathcal{F} denotes the Fourier transform and $R(t)$ is the nonlinear response function given by

$$R(t) = (1 - f_R)(\delta(t)) + f_R h_R (\tau_1^{-2} + \tau_2^{-2}) \tau_1 e^{-t/\tau_2} \sin(t/\tau_1) \quad (1.20)$$

Here, the first term represents the instantaneous electronic response where as the second term is related to the delayed Raman response. f_R is the fractional contribution of delayed Raman response to the nonlinear polarization P_{NL} .

In the case of silica, the following formula agrees well with the experimental observation:

$$h_R = (\tau_1^{-2} + \tau_2^{-2}) \tau_1 e^{-t/\tau_2} \sin(t/\tau_1) \quad (1.21)$$

where $f_R = 0.18$, $\tau_1 = 12.2$ fs and $\tau_2 = 32$ fs.

Equation 1.19 is the Generalized Nonlinear Schrödinger Equation (GNLSE) in the frequency domain.

INTEGRATED ULTRA-HIGH-Q OPTICAL RESONATORS

- [1] K. Y. Yang*, D. Y. Oh*, S. H. Lee*, Q.-F. Yang, X. Yi, and K. Vahala. “Bridging ultra-high-Q devices and photonic circuits”. In: *arXiv preprint arXiv:1702.05076* (2017).

2.1 Abstract

Optical microcavities[7] are essential in numerous technologies[8–12] and scientific disciplines[13, 14]. Applications, including inertial sensors[15–17], microcomb-related systems[8], microwave generation[18–21] and reference cavities/sources[22–25], present challenging combinations of cavity Q-factor performance, phase-matching control and functional requirements. As a result, several critical applications have to date only been demonstrated using discrete ultra-high-Q microcavities. Indeed, finding a scalable microfabrication pathway that preserves ultra-high-Q performance and other device performance metrics while providing access to photonic integration has been a long-term priority of the microcavity field[7]. Here, an integrable ultra-high-Q microcavity is presented. Q factors as high as 230 million are achieved.

2.2 Introduction

Optical microcavities provide diverse functions that include frequency microcombs[8, 26], soliton mode-locked microcombs[27, 28], high-coherence Brillouin lasers[29], bio and nano-particle sensors[10–12], cavity optomechanical systems[14], parametric oscillators[30, 31], Raman lasers[32], and strong-coupling cavity QED systems[33]. A figure of merit used to describe the performance of an optical microcavity is quality factor (Q) of its mode defined as

$$Q \equiv 2\pi \frac{\text{Total energy stored in the cavity}}{\text{Energy dissipated per cycle of light}} \quad (2.1)$$

Here we assume that the optical energy is stored only in a specific mode of the cavity. Using the definition of Q , the temporal decay of energy in the cavity can be written as follows:

$$\frac{dU}{dt} = -\frac{U}{\tau} \quad (2.2)$$

where U is the total energy stored in the cavity, $\tau \equiv Q/\omega_0$ and ω_0 is the resonance frequency of the mode. From Equation 2.2, we find that the stored energy decays as $\sim e^{-t/\tau}$ and the electric field decays as $\sim e^{-t/2\tau}$. As such, we derive the electric field in the frequency domain as

$$E(\omega) = \frac{1}{\sqrt{2\pi}} \int_0^\infty E_0 e^{-t/2\tau + i(\omega - \omega_0)t} dt \quad (2.3)$$

From this equation, the Lorentzian shape of a resonance is derived.

$$|E(\omega)|^2 = \frac{E_0^2}{2\pi[(\frac{1}{2\tau})^2 + (\omega - \omega_0)^2]} \quad (2.4)$$

By defining the linewidth of the cavity $\Delta\omega$ as the full width half maximum of the Lorentzian function, we get $\Delta\omega = 1/\tau$ and $Q = \omega_0/\Delta\omega$. Accordingly, the Q factor of an optical microcavity can be characterized via a temporal scan (ring-down measurement to determine τ) or a spectral scan (linewidth measurement to determine $\Delta\omega$).

$$Q_{\text{total}}^{-1} = Q_{\text{rad}}^{-1} + Q_{\text{abs}}^{-1} + Q_{\text{surf}}^{-1} + Q_{\text{cont}}^{-1} + Q_{\text{ext}}^{-1} \quad (2.5)$$

Key performance metrics scale at least as $1/Q$ and frequently as $1/Q^2$ across all applications areas[7] and have accounted for a sustained period of progress in boosting Q factor by reducing optical loss in micrometer- and millimeter-scale resonators.

Microcavities that have achieved the highest Q factors share a common feature: they are whispering gallery mode (WGM) resonators in which the light is guided through total internal reflection occurring at the boundary of dielectric materials. The round trip optical path length and the group index of a whispering gallery mode determines the free spectral range (FSR), which is the frequency separation between adjacent modes and equals the repetition rate of the pulse in the case of mode-locking.

Figure 2.1 shows Q_{int} plotted versus free spectral range for various material platforms that have demonstrated the highest Q factors so far. The highest Q factor ($Q_{\text{int}} = 3 \times 10^{11}$) was recorded with a 4.5 mm-diameter CaF_2 resonator at wavelength 1550 nm[34, 35]. Fluoride crystalline resonators often exhibit Q factors above 10^9 in near IR wavelengths and also recently showed ultra-high-Q ($> 10^8$) operation in mid-IR wavelengths[36]. Among crystalline materials, not shown in Figure 2.1 is the silicon single-crystal cavity with $Q \sim 2.3 \times 10^{11}$ operated at temperature of 124 K. The

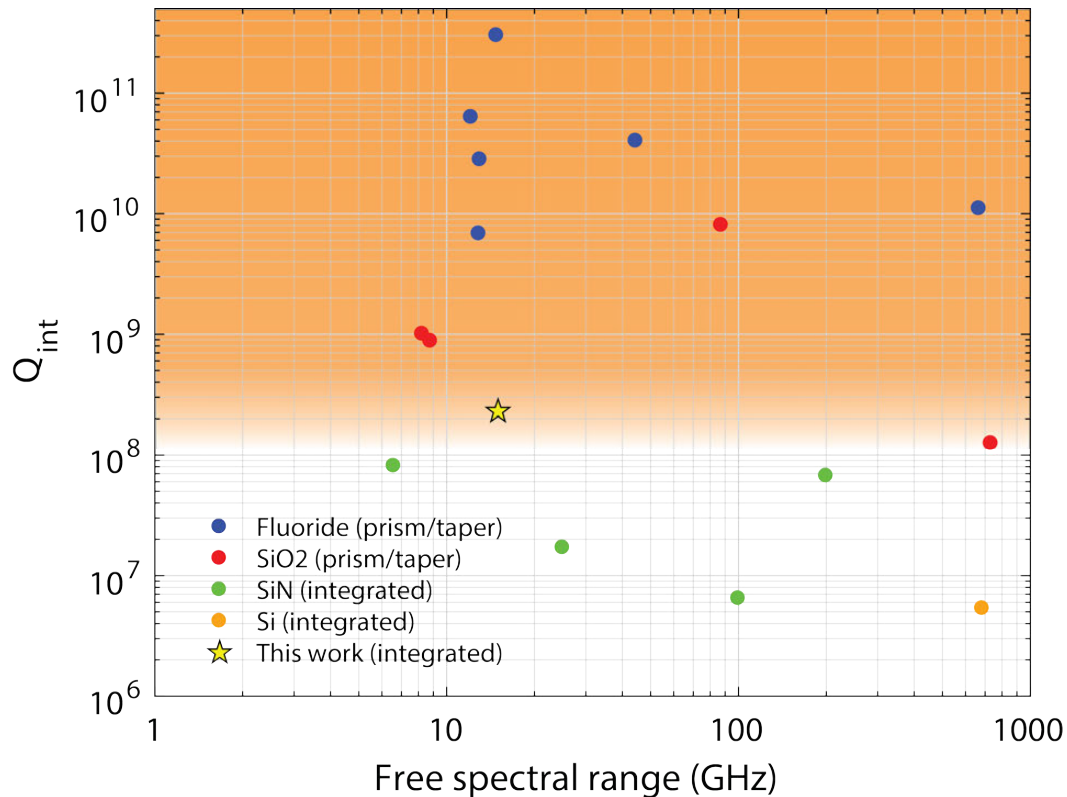


Figure 2.1: **State-of-the-art ultra-high-Q optical microresonator platforms** Review of the optical microresonators that have demonstrated highest Q. The intrinsic quality factors (Q_{int}) are plotted versus free spectral range for various resonator material platforms and coupling schemes. The orange background represents the ultra-high-Q regime ($> 10^8$), which previously have been accessible only by prism- or taper-coupled resonators.

silicon cavity had a round trip length of 210 mm which corresponds to the FSR of 207 MHz. Silica microsphere ($Q = 8 \times 10^9$ [37]), silica microrod ($Q = 10^9$ [38]) and silica microtoroid ($Q = 1.25 \times 10^8$ [39]) are made using heating techniques (hydrogen flame or CO_2 laser) to create a surface-tension-induced smooth and round surface. Silica wedge resonator, fabricated using standard microfabrication process without an additional step of reflow by CO_2 laser, has proven to be a very useful platform because of its high Q (reaching $Q = 8.75 \times 10^8$) and the precise controllability over its FSR usually ranging from ~ 5 to ~ 100 GHz[29].

While the ultra-high-Q regime of optical resonators has easily been accessible using these crystalline or silica-based microresonators, coupling of light into these resonators require a prism or a tapered fiber, an essential component in any experiment using the resonators. Usually, the coupling condition is very sensitive depending on

the relative position of a resonator to the input optical path and has to be controlled through micropositioners and monitored through optical microscopes. This adds a significant complexity to the setup and limits potentials of ultra-high-Q microcavities to be integrated with other on-chip photonic components and reliably deployed in their application areas that require small foot-print devices.

On the other hand, there has been keen interests in developing high Q resonators in integrated platforms. Such a new type of resonator can help realize the promises of optical microresonators to expand the functionalities of photonic integrated circuits (PICs). They can serve as narrowband filters, frequency references or modulators, and become essential building blocks for numerous PIC applications. Ultimately, systems-on-a-chip that have both the electronics and photonic components integrated together will bring significant impact to the landscape of industry. In recent years, a variety of resonator materials have been investigated. One of the most widely used materials is silicon nitride (SiN), which has a wide transparency window and low optical loss from visible to infrared wavelengths. The previous highest Q factor among integrated resonators was achieved in Si_3N_4 [40–43]. Silicon has also been investigated by research groups and showed promising results ($Q_{\text{int}} = 5 \times 10^6$ [44]) However, despite the remarkable progress in boosting the Q factors, there has been no report of integrated resonators whose Q factor exceed 100 million.

In this work, a monolithic microcavity featuring both a Q factor greater than 200 million and an integrated waveguide is demonstrated. The resonator is based on a novel silica ridge fabrication process and the waveguide is composed of plasma-enhanced chemical-vapor-deposited (PECVD) silicon nitride. The structure is fabricated on a silicon wafer using only standard lithography, wet etch, and dry etch steps. The materials, process steps and, in particular, the PECVD silicon nitride waveguide are compatible with other photonic devices. As a result, this process enables full integration of ultra-high-Q devices with other photonic devices on a silicon wafer.

2.3 Silica ridge resonator design

In 2012, Hansuek *et al.* reported a record breaking Q among on-chip resonators of 875 million in a whispering gallery mode silica resonator[29]. The newly developed resonator was a silica wedge disk with air cladding. The disk is mechanically supported by silicon pillar from the bottom. Because the refractive index of silicon is higher than the index of silica, the silicon substrate has to be etched enough so that the optical modes of the wedge resonator don't leak to the substrate. In addition, to

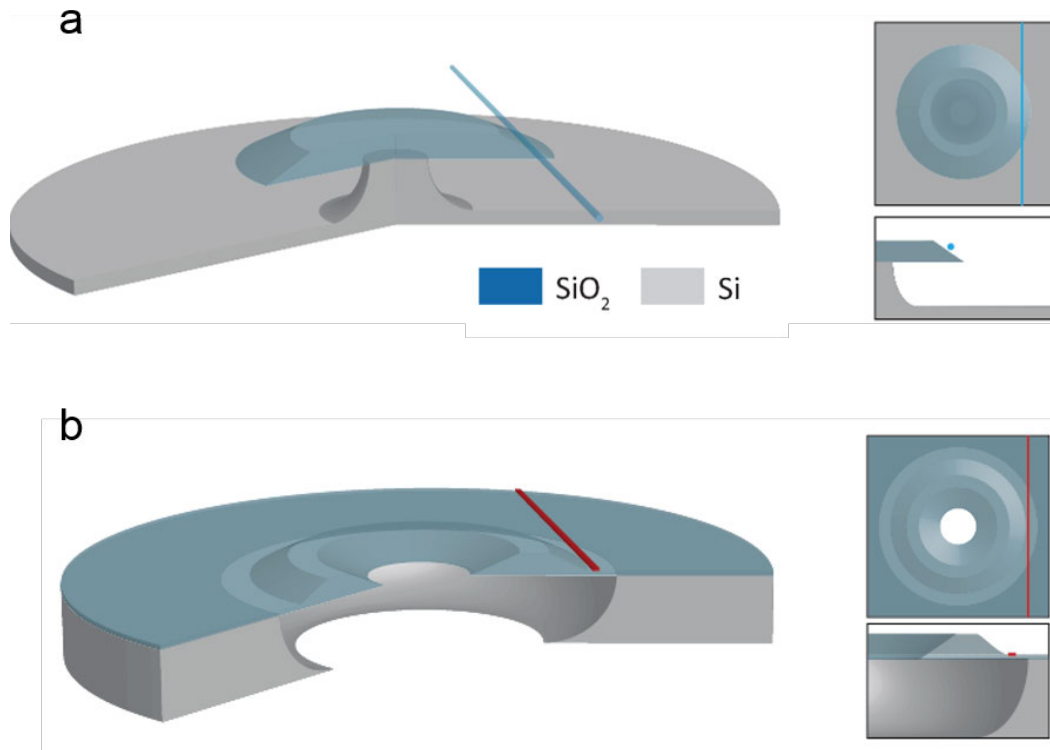


Figure 2.2: **Integration of chemically etched silica resonator with a waveguide**
(a) Schematics of silica wedge resonator. Taper fiber is used for coupling of light into the resonator. **(b)** Schematics of silica ridge resonator integrated with silicon nitride waveguide. Because of the base silica layer, a waveguide can be monolithically integrated with the resonator.

create the smooth silica surface, wet-chemical etch is applied for a long duration to remove the rough line-shape features on silica created during initial wet-etch. As a result, the top of the silica layer retreats by about $12\ \mu\text{m}$ from the edge of the photoresist pattern. The gap between adjacent patterns in silica layer is inevitably enlarged during the wet-etch following the lithography, which makes the integration of the silica wedge resonator with a silica waveguide nearly impossible. Therefore, the coupling to the silica wedge resonators has only been done using tapered fibers (See Figure 2.2a).

Intuitively, the easiest way to monolithically integrate a waveguide with the wet-etched silica resonator is to create a base layer on which both the resonator and the waveguide can be mounted. Fortunately, this base layer can be provided by an additional oxidation of silicon. Furthermore, by patterning a center hole in the silica layer through which XeF₂ gas can flow into and etch away silicon, a silica ridge

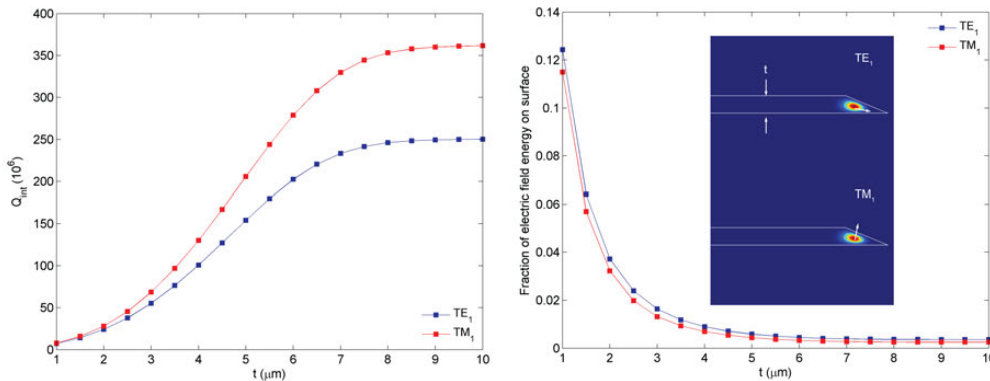


Figure 2.3: Calculated quality factor of a wedge resonator as a function of the resonator thickness (a) Intrinsic quality factor (Q_{int}) versus the resonator thickness (t , indicated by the arrows in b) of a silica wedge resonator for the fundamental TE and TM mode families. (b) The fraction of electric field energy near the surface (defined in the text). Calculated mode profiles of the fundamental modes are shown as an inset. The arrows at the electric field intensity maximum represent the direction of the electric field. In general, the TM_1 mode has higher Q factor than the TE_1 mode due to the weaker electric field at the silica-air boundary

ring resonator that is supported by silicon pillar from the outer side can be made as shown in Figure 2.2b. At the same time, a waveguide of a different material can be deposited, patterned and etched to provide a waveguide channel for coupling light into and out from the resonator. We choose PECVD silicon nitride (SiN) as the waveguide material because it has low optical loss and a wide transparency window from the visible to all across the near IR wavelengths, and it is CMOS-compatible. Its low tensile stress compared to that of LPCVD SiN or stoichiometric Si_3N_4 is the key to the successful deposition of the nitride film on the silica layer with ridge structure. The details of the fabrication procedure are provided in Section 2.5.

To access the ultra-high-Q regime with the integrated silica ridge resonator, the resonator geometry is optimized with the help of Finite Element Method (FEM) simulations. First, we note that the quality factor of a conventional silica wedge resonator is limited by the surface roughness. The surface roughness induces the inhomogeneities of the dielectric constant at the surface from which Rayleigh scattering arises[45]. In numerical simulations, we approximate the surface roughness by a 200 nm - thick absorption layer at the silica-air boundary with the absorption coefficient that yields the calculated Q factor similar to the measured values[46]. Figure 2.3a shows the calculated Q_{int} versus the resonator thickness t_1 for the fun-

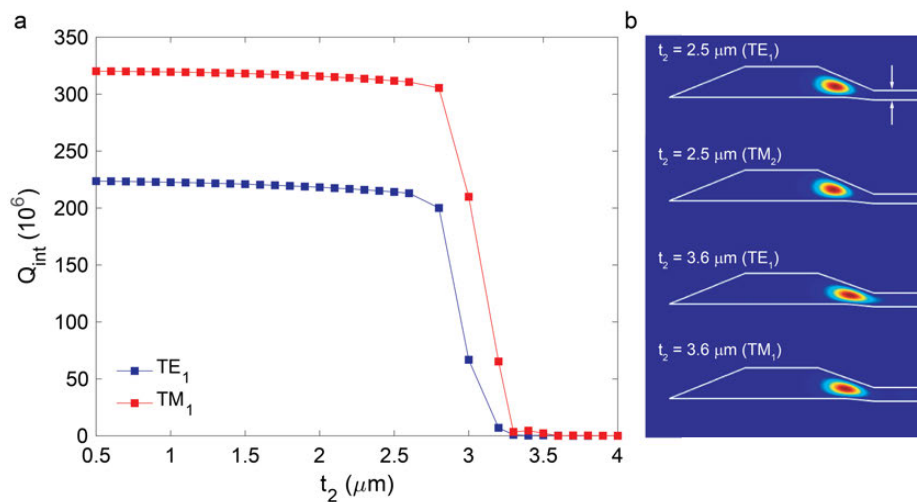


Figure 2.4: **Optimization of base silica layer thickness** (a) Intrinsic quality factor (Q_{int}) versus base layer thickness (t_2 , indicated by the arrows in **b**) of a silica ridge resonator for the fundamental TE and TM mode families. (b) Calculated mode profiles of the fundamental modes at $t_2 = 2.5 \mu\text{m}$ and $t_2 = 3.6 \mu\text{m}$

damental TE and the TM mode of the wedge resonator. As the resonator thickness increases, Q_{int} grows until it starts saturating around $t_1 = 8 \mu\text{m}$. Another interesting thing to note is that the TM mode has higher Q_{int} than the TE mode. Such trends of Q_{int} can be explained by the fraction of electric field energy contained in the surface layer. The electric field of thicker resonator modes are more concentrated inside, away from the silica-air boundary, and TM_1 mode has smaller electric field energy density at the surface than the TE_1 mode.

Taking the hint from the wedge resonator results, we choose the total ridge thickness t_1 to be $8 \mu\text{m}$. The top width of the ridge is set to be $20 \mu\text{m}$ which is large enough to maintain the high Q of the fundamental modes. While the presence of the base silica layer enables the integration, it can also induce the radiation loss of the resonator. To mitigate the radiation loss, the relative thickness of the base layer (t_2 in Figure 2.4) to the total thickness of the ridge (t_1) needs to be kept low. Another set of FEM simulations is performed to find the optimal t_2 value. The calculated intrinsic Q versus t_2 for the fundamental TE mode (TE_1) and the fundamental TM mode

(TM₁) is presented in Figure 2.4, where the TE (TM) mode has its electric field (magnetic field) parallel to the wedge surface. The result shows that as t_2 increases from 0.5 μm to 2.5 μm , the intrinsic Q degrades by 2.6% and 4.2% for the TE₁ and TM₁ mode, respectively. However, when t_2 increases above 2.5 μm , a sudden drop in Q is observed, with Q less than 10^8 at $t_2 = 3.1 \mu\text{m}$ for both modes. The drop in Q is accounted for by the leakage of the electric field into the base silica layer. The calculated mode profiles of the TE₁ and TM₁ mode for the resonator with $t_2 = 2.5 \mu\text{m}$ and 3.6 μm are shown in Figure 2.4b, revealing the mode leakage for the resonator with $t_2 = 3.6 \mu\text{m}$.

While small t_2 is beneficial optically, too small value of t_2 is undesirable for mechanical stability of the silica resonator on silicon. The main issue related to the mechanical stability of the resonator is the buckling of the silica layer that happens when XeF₂ gas etches the silicon above the threshold undercut value. The buckling is induced by the thermal stress between the silica and the silicon layer and has been studied previously[47]. Experimentally, it is observed that the threshold undercut value is about 50 μm for a 2.5- μm thick silica resonator. This shows the possibility that the ridge resonator remains unbuckled for silicon undercut of 50 μm away from the optical mode. Such an undercut value is large enough to ensure that the mode does not interact with the silicon substrate. Therefore, we choose $t_2 = 2.5 \mu\text{m}$ as the base silica layer thickness.

2.4 Design of a single mode silicon nitride waveguide phase-matched to a silica ridge resonator

A heterogeneous integration of a microresonator with an waveguide of another eator that have the same dimension and are made of the same material. Such a design almost guarantees the ideal phase-matching (i.e., effective-index-matching) which is required for an efficient coupling. The homogeneous integration is also easier in the sense of the required fabrication techniques as the resonator and the waveguide can be simultaneously made in their common process steps. In reality, however, homogeneously integrated resonator-waveguide platforms face a fundamental problem that limits their ultra-high-Q operation.

Problems faced by homogeneous integration of multimode waveguide-resonator platforms

High-Q integrated resonators are mostly multi-mode resonators supporting higher order modes. Integrated resonators that are single-mode exist as well, but they often

suffer higher loss ($Q_{s,s}^{-1}$, Q_{cont}^{-1} , Q_{rad}^{-1}) due to their small mode area and enhanced electric field at the resonator surface. The inevitable use of multi-mode resonator structures in the highest-Q integrated platforms is usually accompanied by the multi-mode bus waveguides that are phase-matched to the resonators. The multi-mode nature of the bus waveguide becomes the key to the parasitic loss in the waveguide-resonator coupler commonly observed in the homogeneous integration.

A figure of merit that describes the performance of the coupler is the coupling ideality I defined as follows[48, 49].

$$I = \frac{\kappa_{\text{ex},0}}{\kappa_{\text{ex},0} + \kappa_{\text{p}}} \quad (2.6)$$

Here, $\kappa_{\text{ex},0}$ is the external coupling rate of a resonator mode to the target bus waveguide mode and κ_{p} is the parasitic loss given by $\kappa_{\text{p}} = \kappa_{\text{rad}} + \sum_{n>=1} \kappa_{\text{ex},n}$ where $\sum_{n>=1} \kappa_{\text{ex},n}$ represents the sum of the external coupling rates to the higher order modes. For a device on resonance, the power transmission T can then be expressed as

$$T = \left| 1 - \frac{2}{K^{-1} + I^{-1}} \right|^2 \quad (2.7)$$

where $K = \kappa_{\text{ex},0} / \kappa_0$ is the normalized coupling strength and κ_0 is the intrinsic loss rate of the resonator mode. Equation 2.7 shows that for a critical-coupling condition to be reached where $T = 0$, the coupling strength should satisfy $K = K_{\text{crit}} \equiv 1/(2 - I^{-1})$. The critical coupling cannot be reached for $I \leq 0.5$, and when $I > 0.5$, K_{crit} as a function of I reaches the minimum $K_{\text{crit}} = 1$ at $I = 1$. In reality, the ideality I is less than unity because of the parasitic loss. In the case of a multimode bus waveguide, the sum of the external coupling rates to the higher order modes ($\sum_{n>=1} \kappa_{\text{ex},n}$) reduces I , thereby increasing K_{crit} . As a result, the external coupling rate between the resonator mode and the fundamental mode of the waveguide must increase in order to achieve the critical coupling. This can be done by reducing the gap between the waveguide and the resonator, or by increasing their interaction length.

There are additional problems that are faced by the use of multimode waveguides. First, the coupling of the resonator mode to multiple modes of the waveguides can create an undesirable interference pattern in the resonance spectrum. Secondly,

adjustments of the multimode waveguide cross-section away from the resonator-waveguide coupler can cause power loss in the higher-order modes of the waveguide. For example, if inverse tapers are used at the end of the waveguide to enhance the coupling efficiency to the chip, power transferred through the higher-order modes can be completely lost at the inverse tapers. Such power loss degrades the loaded Q of the resonator.

Heterogeneous integration : a single-mode waveguide integrated with a multi-mode UHQ resonator

Thus, a single-mode waveguide integrated with a multi-mode ultra-high-Q resonator is a highly desirable platform that avoids the penalty of using a multi-mode waveguide. For this end, a waveguide material that has higher refractive index than the resonator material can be chosen. In our case, the waveguide core is made of silicon nitride, which has a refractive index of 1.979 at wavelength 1550 nm. It is surrounded by the air cladding at the top and the lateral sides, and it is supported by the silica - air substrate as shown in Figure 2.5a.

A simple way to describe the requirement for a waveguide mode to be formed is using its effective index (n_{eff}) defined as $n_{\text{eff}} = \beta/k$ where β is the propagation constant and k is the free-space wavenumber. The effective index of the waveguide mode must satisfy the following condition:

$$n_s < n_{\text{eff}} < n_c \quad (2.8)$$

Here, n_s is the effective index of the slab mode in the base silica layer. We consider only the fundamental TE slab mode that has the highest effective index among all the slab modes. n_s is a function of the thickness of the base layer t_2 defined in the previous section. For $t_2 = 2.5 \mu\text{m}$, we have $n_s = 1.42$, which is lower than the refractive index of silica (1.444). Figure 2.6a shows the calculated effective index of the SiN waveguide modes as functions of the waveguide width (W). In this calculation, the waveguide thickness (T) is set to be 250 nm. Note that at $W = 4 \mu\text{m}$, the waveguide supports four transverse modes : namely, TE_{11} , TE_{21} , TE_{31} and TM_{11} (See Figure 2.6b). The polarizations of the TE and the TM mode are parallel and perpendicular to the top surface of the waveguide, respectively. As W decreases, n_{eff} of the higher order modes decreases until it hits the value 1.42 one by one, at which the modes completely leak to the silica slab and are not confined to the silicon nitride core anymore. At $W < 1.2 \mu\text{m}$, the waveguide is single-mode supporting

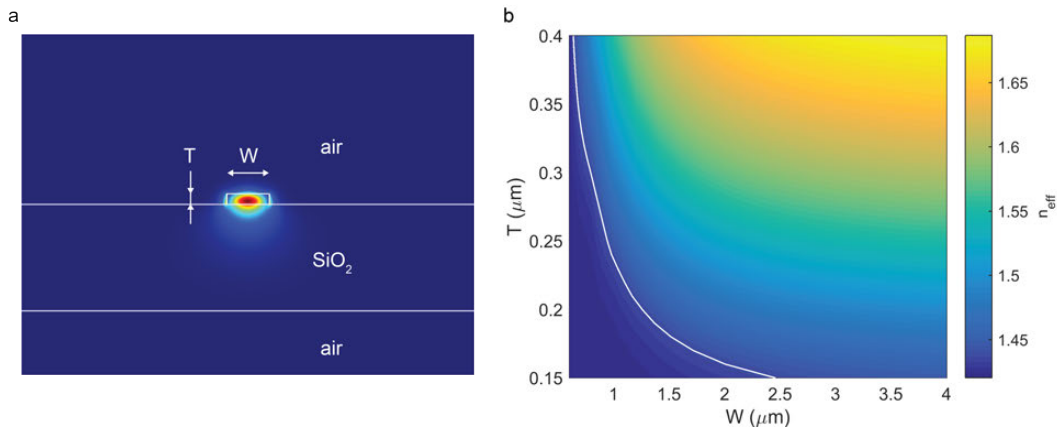


Figure 2.5: **Effective index of the TE₁₁ mode of the silicon nitride waveguide (a)** Calculated mode profile of the TE₁₁ mode of the SiN waveguide. **(b)** Calculated effective index (n_{eff}) of the TE₁₁ mode as a function of the waveguide width W and thickness T denoted in **a**. The white solid line indicates the pairs (W, T) for which the effective index of the SiN waveguide matches the effective index (1.438) of the TM₁ mode of the silica ridge resonator.

only the TE₁₁ mode. Note also that the effective index of the TM₁ mode of the resonator is 1.438 and is indicated in Figure 2.6a. The phase-matching waveguide width is 940 nm at which the waveguide is single-mode.

The color map in Figure 2.5b illustrates the effective index of the TE₁₁ mode for various values of W and T . The white solid line indicates the pairs (W, T) for which the phase-matching occurs. However, too small or large value of W on this curve is undesirable because of the high loss induced by the side-wall roughness and the low coupling efficiency due to the large aspect ratio ($W:T$) of the waveguide, respectively. We choose $W = 940$ nm $T = 250$ nm as our design target.

2.5 Fabrication process

The fabrication process of integrated silica resonators with silicon nitride waveguides is schematically shown in Figure 2.7 It begin by growing a thermal silica layer on a (100) prime-grade float-zone silicon wafer. After silicon wafers are loaded into an oxidation furnace (Tystar Tytan 4600), oxidation time is input to the system. The thickness of the thermally grown silica layer can be precisely controlled by the oxidation time[50]. In this work, the oxidation thickness of 8 μm is chosen as discussed in Section 2.3.

The silica layer is then patterned using standard photolithography process steps. Positive photoresist(Shibley Micropost S1800 series) is spin-coated on the silica

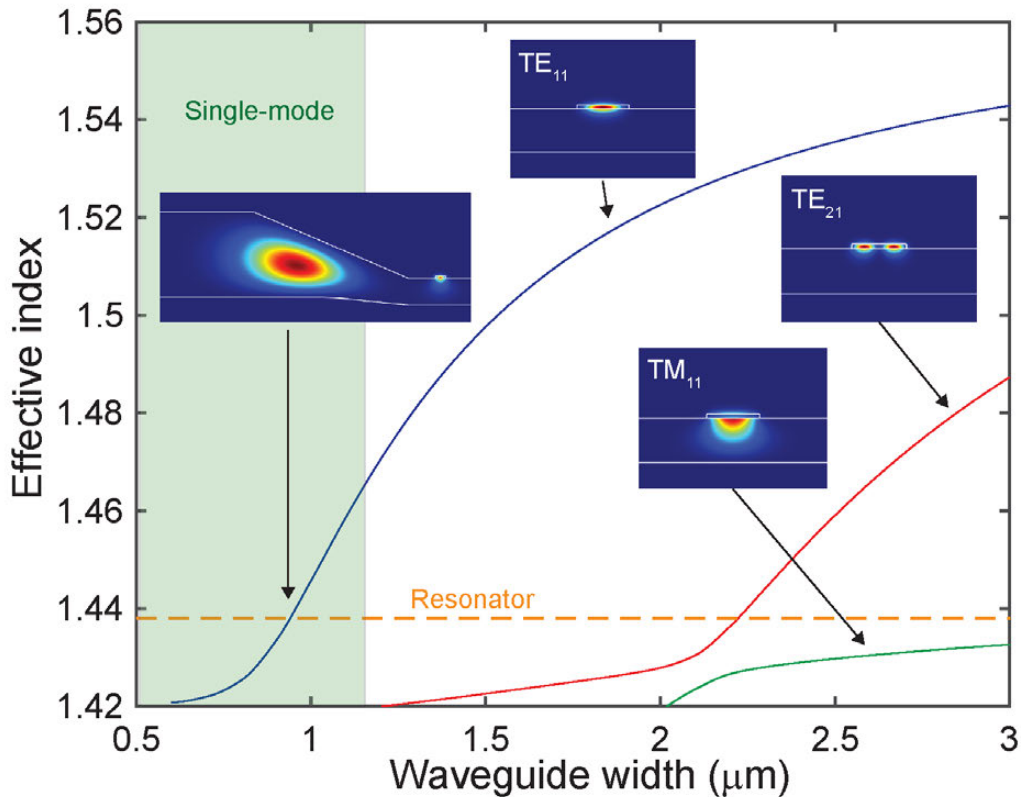


Figure 2.6: **Design of the single mode SiN waveguide** (a) Effective indices of the SiN waveguide modes are plotted as functions of the waveguide width W . The waveguide thickness T is 250 nm. (b) The calculated mode profiles of low-order modes (TE_{11} , TE_{21} , TE_{31}) for the waveguide with $W = 4 \mu\text{m}$ are shown as inset

layer and patterned using GCA 6300 stepper. Here, together with a disk, align marks are also patterned for the alignment of the wafer and the photomask in the second lithography step taking place later. Then, the silica layer is then wet etched using buffered hydrofluoric acid (HF) according to a process used to create wedge resonators[29]. As shown in Figure 2.8a, the resulting etched oxide forms a circular disk structure that defines the exterior of the resonator.

Subsequently, an additional thermal oxidation grows the base oxide layer beneath the oxide disk (See Figure 2.7b). The thickness of the base oxide layer is $2.5 \mu\text{m}$. The oxide layer growth is followed by deposition of 500 nm of plasma-enhanced chemical-vapor-deposited (PECVD) silicon nitride. Lithography and a shallow ICP RIE dry-etch steps are then applied to partially etch the silicon nitride. Phosphoric acid is used to fully define the silicon nitride waveguide. A thin layer (20 nm) of silica is applied by atomic layer deposition to protect the silicon nitride waveguide

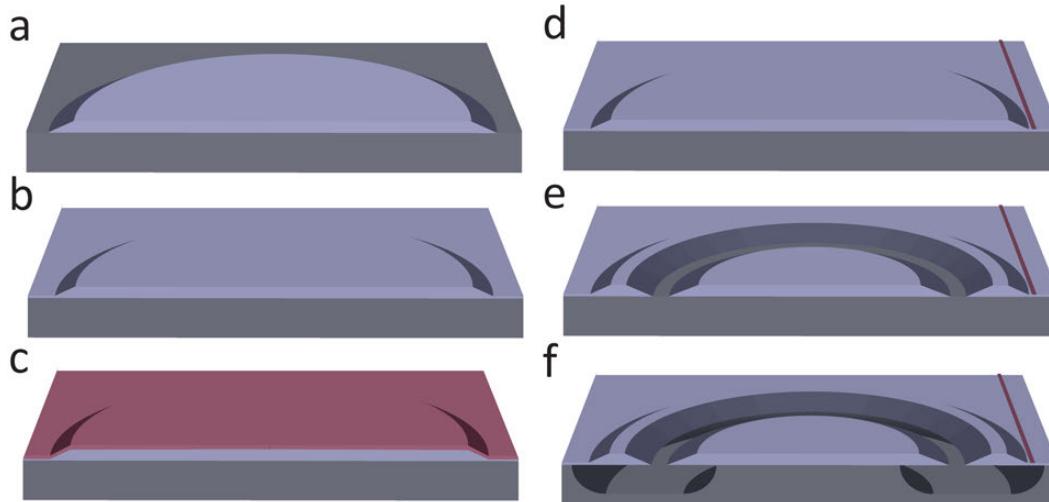


Figure 2.7: **Fabrication process for integrated ultra-high-Q microresonator** (a) Silica disk is defined on silicon by photolithography and HF etching of an initial silica layer. (b) Thermal oxidation grows a second oxide layer beneath the etched silica disk. (c) PECVD silicon nitride is deposited. (d) Silicon nitride waveguide is defined on silica layer by lithography and etching. (e) Lithography and wet etch of the silica define a ring aperture to the silicon substrate. (f) XeF_2 etches the silicon through the ring aperture.

during the final dry etch step below. A lithography/wet-etch step is then used to open an interior, ring aperture to the silicon substrate. In the final step, xenon difluoride (XeF_2) etches the silicon through the interior ring aperture so as to create an optical cavity. The silicon undercut is about $70 \mu\text{m}$. The structure of fabricated resonators is shown in Figure 2.8.

2.6 Experimental demonstration of waveguide-resonator coupling

A cross-sectional rendering of the resonator structure is shown in Figure 2.8a. A mode field is also included. In Figure 2.8b, a scanning electron microscope (SEM) image shows three ridge resonators connected by a common silicon nitride waveguide (false color red in the image). White arrows indicate how light guided in the silicon nitride couples into the ridge resonator where it circulates and then recouples to the waveguide. The silicon nitride waveguide has a thickness of approximately 250 nm. It is initially 3 to 3.5 microns in width at the edge of the wafer and is tapered to about 900 nm near the resonator so as to phase match to the resonator optical mode. The lightwave evanescently couples between the silicon nitride waveguide and the microcavity through the silica layer which supports the waveguide. Shown in Figure 2.8c is a photograph of end-fire coupling to a single

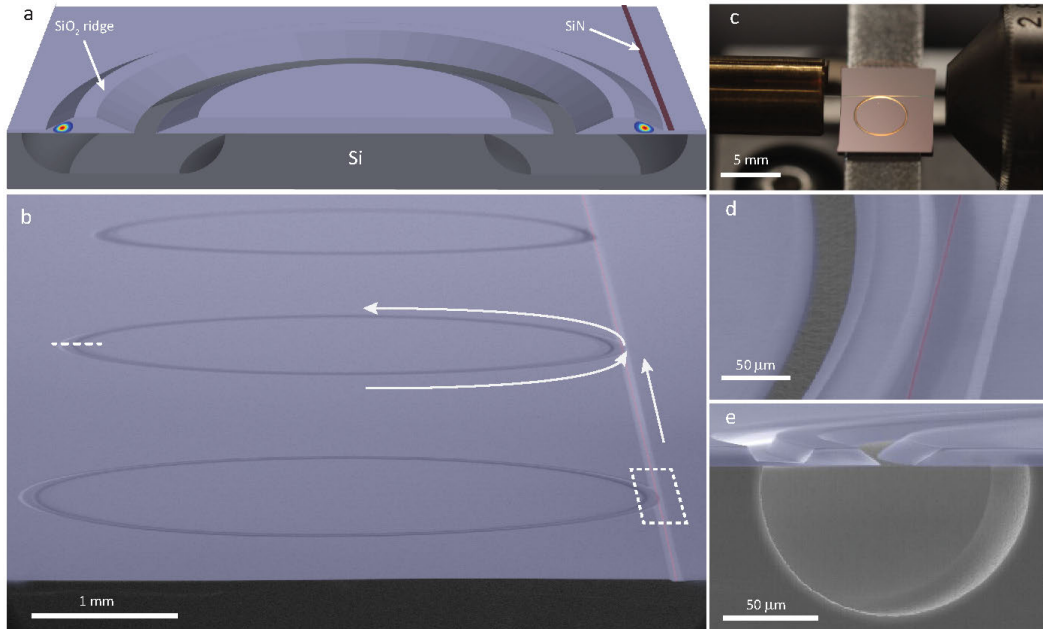


Figure 2.8: Integrated ultra-high-Q microresonator (a) Rendering showing silica ridge resonator with nearby silicon nitride waveguide. Fundamental spatial mode is illustrated in color. (b) SEM image of three ridge resonators with a common silicon nitride waveguide (false red color). White arrows show the direction of circulation within the center resonator for the corresponding direction of coupling from the waveguide. Dashed white box is the region for the zoom-in image in 1d. Dashed white line segment gives the location of cleavage plane used for preparation of the SEM image in 1e. (c) Photograph of a single resonator with endfire coupling provided by a lensed fiber (left) and aspheric lens (right). (d) SEM zoom-in image of the waveguide-resonator coupling region shown within the dashed white box in 1b. (e) SEM image of resonator cross section prepared by cleaving at the dashed white line in 1b.

resonator using a lensed fiber (left) and light collection with an aspheric lens (right). Approximately 25 % of the power could be coupled from the lensed optical fiber to the silicon nitride waveguide. No attempt to improve coupling was made, but in the future a tapered waveguide end can be introduced to improve the coupling efficiency[51]. SEM zoom-in and cross-sectional views are shown in Figure 2.8d and in Figure 2.8e.

Spectral measurements of the integrated microcavity were performed by end-fire coupling to a tunable external cavity laser and monitoring of the transmission through the waveguide-coupled device as the laser is scanned (Figure 2.9). The devices tested had a FSR of approximately 15 GHz (ridge ring diameter of approximately 4.3 mm). Figure 2.9a presents a spectral scan containing over two FSRs. Several

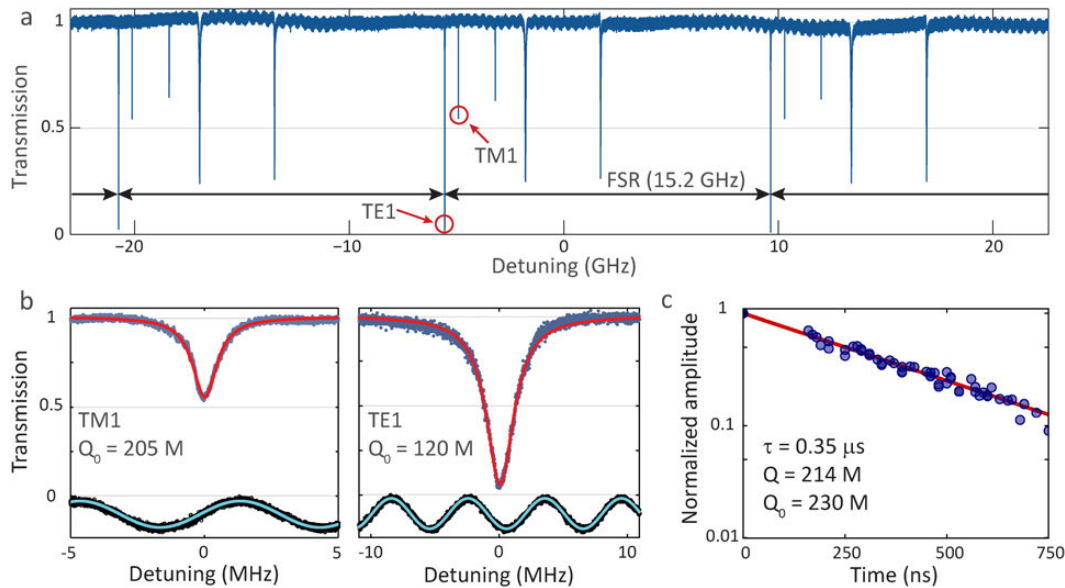


Figure 2.9: Spectral scan of integrated ridge resonator and ring-down measurement (a) Spectral scan encompassing two free-spectral-ranges. (b) High resolution zoom-in scan for the TM1 and TE1 modes with intrinsic (Q_0) and loaded (Q) quality factors, as well as the linewidth ($\kappa/2\pi$) indicated (M = million). The green sinusoidal signal is a frequency calibration scan using a radio-frequency calibrated fiber Mach-Zehnder interferometer (free-spectral range is 5.979 MHz). (c) Superposition of 10 cavity-ringdown signal scans for the TM1 mode with the corresponding decay time and the loaded and intrinsic Q factors.

transverse modes appear in the scan. These transverse mode families were identified by collecting broad dispersion curves for the resonator modes as described below and comparing to numerical modeling. High-resolution scans of the TE1 and TM1 modes are presented in Figure 2.9b. The frequency scales in the scans are calibrated using a fiber Mach-Zehnder interferometer which appears as the green sinusoid at the lower half of each panel. Spectral calibration of the interferometer is performed using microwave sidebands generated by phase modulation of the laser. A linewidth fitting algorithm gives an intrinsic Q factor of 120 million for the TE1 mode and 207 million for the TM1 mode. To further confirm the high optical Q factor of the TM1 mode, cavity ring down was performed[36]. A superposition of ten ring-down traces is presented in Figure 2.9c and gives an intrinsic Q factor of 214 million in close agreement with the linewidth data.

DEMONSTRATION OF NONLINEAR OPTICS IN INTEGRATED ULTRA-HIGH-Q RESONATORS

- [1] K. Y. Yang*, D. Y. Oh*, S. H. Lee*, Q.-F. Yang, X. Yi, and K. Vahala. “Bridging ultra-high-Q devices and photonic circuits”. In: *arXiv preprint arXiv:1702.05076* (2017).

3.1 Abstract

Integrated ultra-high-Q silica ridge resonators combined with performance controls on dispersion and device size enable demonstration of new integrated functionality including soliton generation at electronically-processible rates and high-coherence Brillouin laser oscillation. The device represents a critical advance for miniaturization of optical-synthesizers[52], optical clocks[9, 53, 54], spectroscopy systems[55–57], microwave sources[18–21], and rotation sensors[15–17].

3.2 Introduction

Optical microcavities[7] provide diverse functions that include frequency microcombs[8, 26], soliton mode-locked microcombs[27, 28, 58–60], high-coherence Brillouin lasers[29], bio and nano-particle sensors[10–12], cavity optomechanical systems[14], parametric oscillators[30, 31], Raman lasers[32] and strong-coupling cavity QED systems[33]. Key performance metrics scale at least as $1/Q$ and frequently as $1/Q^2$ across all applications areas[7]. For example, higher Q factors dramatically reduce power consumption as well as phase and intensity noise in signal sources, because these quantities scale inverse quadratically with Q factor. Higher Q also improves the ability to resolve a resonance for sensing or in a frequency-reference-cavity. Such favorable Q scalings have accounted for a sustained period of progress in boosting Q factor by reducing optical loss in micro- and milli-scale resonators across a range of materials[61–65]. Also, system-on-a-chip applications have driven interest in methods to fabricate high-Q integrable resonators[40, 42, 43, 62, 63, 66–68]. Major Q performance gains in silicon nitride, for example, have boosted Q values in waveguide-integrated devices to as high as 80 million[40] and 67 million[68] in strongly-confined devices. Nonetheless, the highest Q-factor resonators remain discrete devices that are crystalline[35] or silica based[7, 29, 39,

69]. They use fiber tapers[49, 70] and prisms[31] for optical coupling. These silica and crystalline-based devices are also the only devices to have so far realized a series of critical functions that include generation of electronic-repetition-rate soliton streams, near-earth-rate rotation measurement, high-performance microwave signal generation and operation as reference cavities and reference sources. These functions are required in a diverse set of new miniature photonic systems and they impose a serious challenge for ultra-high-Q microfabrication through a scalable, integration-ready fabrication process.

As a further complication several functions require performance controls relating to size and dispersion/phase-matching, and these requirements can impose additional demands on the optical Q factor. For example, pulse repetition rates that are both detectable and readily processed by electronics are required in all frequency combs in order to self-reference the comb[71]. To achieve self-referenced octave-span operation in microcombs at practical power levels, frequency comb formation is divided into a THz-rate comb (micrometer-scale resonator diameter) and an electronics-rate comb (centimeter-scale resonator diameter)[52]. While the smaller-diameter, THz-repetition-rate, soliton combs have been demonstrated with integrated waveguides[72, 73], the electronics-rate soliton microcomb has so far only been possible using discrete silica and crystalline devices[27, 28]. Part of the challenge here relates to achieving a high enough Q-factor to overcome the increased pumping volume of the larger electronics-rate soliton comb. Another important consideration is that the soliton mode locking process requires careful resonator design to minimize avoided mode crossings and to create overall anomalous dispersion. Attaining the combined features of ultra-high-Q factor to overcome the large optical pumping volume and resonator-dispersion-management to enable soliton formation while also providing an integrated waveguide has so far not been possible.

Larger resonator designs are also required in optical gyroscopes where they boost the Sagnac effect. For example, centimeter-scale silica and crystalline devices have recently been shown to achieve rotation rate sensitivities near the Earth's rotation rate using passive[17] and active resonators[16]. In addition to the the sensitivity enhancement which results from the ultra-high-Q factors of the silica and crystalline resonators, the active resonator approach uses high-relative-coherence Brillouin lasers to measure rotations. The excellent sub-Hertz linewidths of these lasers result from the inverse quadratic scaling of the Schawlow-Townes phase noise with Q factor[74]. Moreover, ultra-high-Q is essential here to maintain low pumping

power[74] at the larger device diameters used to enhance the Sagnac effect[16, 17]. Similar considerations apply for microwave synthesizers[19] and microwave references[20] based upon high-coherence Brillouin lasers.

Finally, it is noted that performance considerations relating to noise and fluctuations frequently require the combination of high-Q and large mode volume that creates complexities for a scalable fabrication process. Solid-state reference cavities are such an example. These devices require the highest possible Q factors to maximize resolution of the cavity mode by a laser that is to be stabilized. At the same time, the cavities are subject to thermorefractive, photothermal and optomechanical fluctuations[22, 75] that destabilize the cavity frequency. These fluctuations vary inversely with resonator size. Large mode volume designs (including compact, spiraled meter-long cavities[24]) and designs that feature a reduced refractive index dependence on temperature are used to improve stability[23–25]. As a related comment, the fundamental timing jitter noise of a microcomb soliton stream is also predicted to scale as n_2/V where n_2 is the Kerr nonlinear coefficient and V is the mode volume[76]. While current soliton systems are limited by technical noise associated with the pumping laser[77], improved pumping designs may ultimately be limited by this fundamental source of noise. As minimization of this parameter also increases pumping power, ultra-high-Q designs will be required to maintain low pumping power in such low noise designs.

3.3 Soliton comb generation

Dissipative Kerr solitons represent a major advance in the subject of frequency microcombs[27]. They provide highly reproducible optical spectra, have achieved 2/3 and full octave span coverage[58, 73] and exhibit highly stable repetition rates[28]. Importantly, these devices provide a miniature platform for potential full integration of frequency comb systems. However, as noted above, a detectable repetition rate soliton comb using an integrable device platform has not yet been realized. Therefore, as a demonstration of the new performance capability provided by the integrated ridge resonator, a 15 GHz soliton stream was generated.

The TE₁ mode family dispersion was first characterized by measuring the frequency of all modes between 1530 nm and 1580 nm using an external cavity laser calibrated by the Mach-Zehnder interferometer described above. This data was then plotted by removing both an offset frequency (ω_0) and a linear dispersion term proportional to the FSR (D_1) of the TE₁ mode family at ω_0 ($D_1/2\pi = 15.2$ GHz was measured).

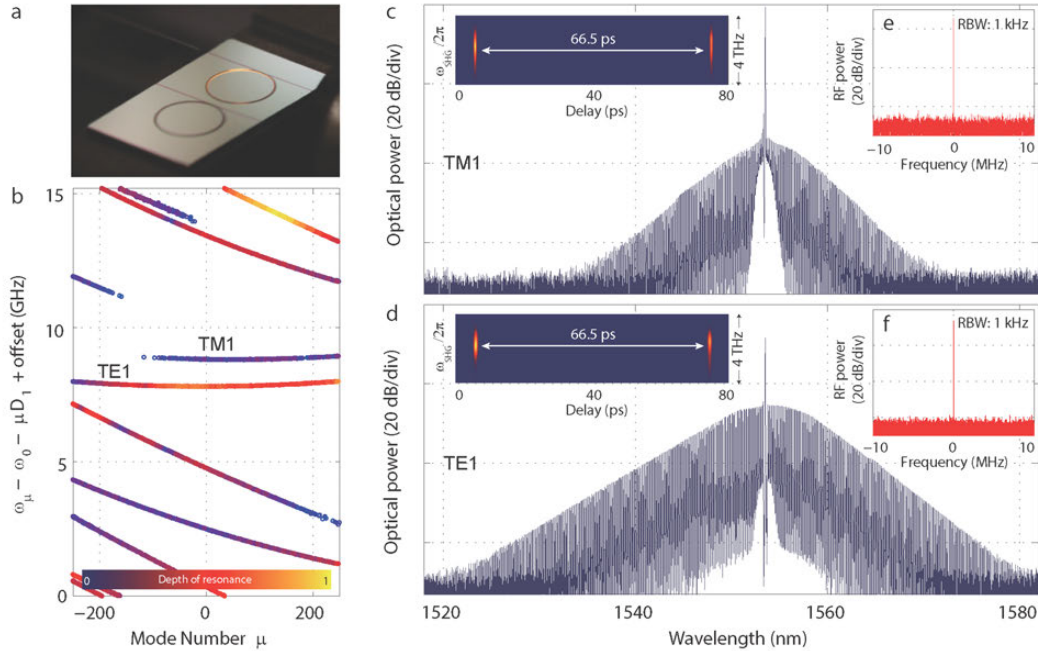


Figure 3.1: **Demonstration of detectable repetition rate temporal solitons in an integrated optical microresonator** (a) Photograph of a silicon chip with two integrated silica ridge resonators. (b) Measured mode frequencies plotted versus mode number for all the waveguide-coupled cavity modes with linear dispersion removed. (b) Optical spectrum of soliton with pump line indicated. Inset shows the electrical spectrum of the detected soliton pulse stream (RBW: resolution bandwidth) (c) FROG scan of single soliton state in 3b showing the single pulse signal with pulse period of 66.5 ps corresponding to resonator round-trip time.

Modes are indexed using the label μ with $\mu = 0$ assigned to the mode at frequency ω_0 , which is also the mode that is pumped to generate the solitons. The resulting data are plotted in Figure 3.1b. The red curve is a parabola showing that the mode family is dominated by second-order dispersion over the range of modes measured. A fitting gives $D_2/2\pi = 6.4$ kHz for the TE mode and $D_2/2\pi = 7.0$ kHz for the TM mode where $\omega_\mu = \omega_0 + D_1\mu + D_2\mu^2/2$. Significantly, there is no observable mode-crossing-induced distortion of both mode families, therefore making the mode families well suited for soliton formation[27, 28]. Solitons were triggered and stabilized using the power kick[58] and capture-lock technique[78]. An optical spectrum is shown for a single soliton state generated in the TM1 mode family in Figure 3.1. Visible in the spectrum is the optical pump wave. To confirm the detectable repetition rate, the soliton pulse stream was directly detected and analyzed on an electrical spectrum analyzer. The electrical spectrum is provided as

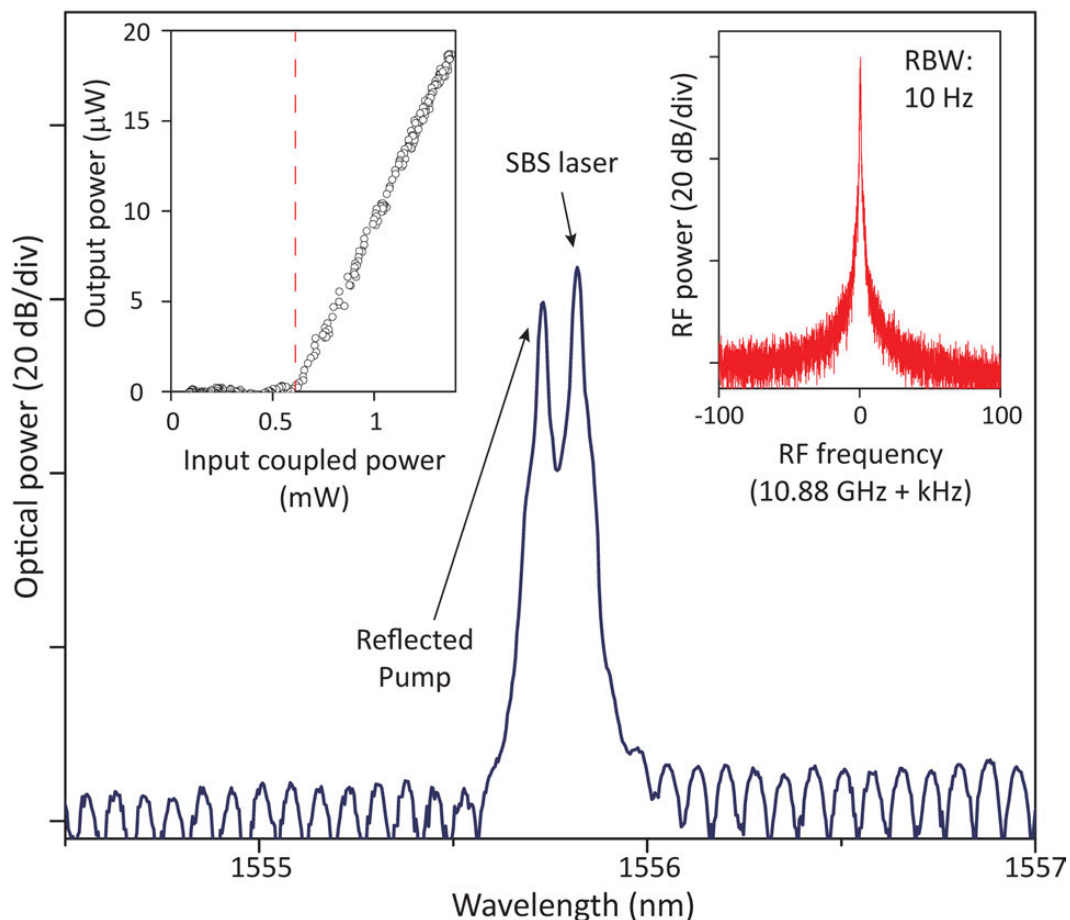


Figure 3.2: **Demonstration of Brillouin lasing in an integrated optical microresonator** Optical spectrum of Brillouin laser. The left inset demonstrates the output laser power vs. input coupled power. These data shows laser threshold behavior and the measured threshold power is as low as $250 \mu W$. The right inset shows RF beat of the back-reflected pump and lasing signal.

the right inset in Figure 3.1c and shows a measured repetition rate near 15.2 GHz. To confirm the pulse nature of the soliton the frequency resolved optical gate (FROG) method was used to measure the pulse train[27]. The FROG data is presented as the left inset in Figure 3.1c. The same types of characterizations were done for the TE1 mode and their results are presented in Figure 3.1d.

3.4 Stimulated Brillouin laser operation

The stimulated Brillouin process has attracted considerable interest in micro devices[79]. Brillouin laser action has been demonstrated in discrete resonators based on silica[25, 29, 74, 80] and CaF_2 [81]. Laser action has also been realized in integrated resonators using silicon[82] and chalcogenide waveguides[83] have also

been realized. However, reference sources[25], microwave synthesizers[84] and Brillouin gyroscopes[16] require the highest possible optical Q factors for generation of narrow-linewidth signals and has so far relied upon discrete devices. As a second demonstration of function, the integrated ridge resonator is applied to generate high coherence Brillouin laser action. Devices were fabricated to phase match the Brillouin process when pumped near 1550 nm. Device diameters of approximately 6.0 mm were fabricated and tested. Figure 3.2 shows the optical spectrum of the lasing Stokes wave. The weak pump signal peak in the spectrum results from the need to collect the lasing Stokes wave in the propagation direction opposite to the pumping direction. Its strength is determined by residual backscattering in the measurement. The upper left insets to Figure 3.2 shows the Stokes power versus pumping and give a threshold of 500 microWatts. The upper right inset is the microwave beat signal between the pump wave and the Stokes wave. It has a high coherence as evidenced by the resolution bandwidth (RBW) or 10 Hz used in the measurement.

3.5 Summary

In summary, we have demonstrated a resonator having an optical Q factor greater than 200 million with a monolithically integrated waveguide. Soliton generation at 15 GHz was also demonstrated to illustrate functionality currently not attainable with other integrated resonator platforms. The waveguide material, PECVD silicon nitride, is among the most widely used waveguide materials in the photonics industry and provides a nearly universal interface to other photonic devices fabricated on a common silicon wafer. In addition to the detectable repetition rate soliton micro-comb, high-coherence Brillouin lasers and Brillouin gyroscopes should be readily transferrable to the process demonstrated here.

TOWARDS VISIBLE MICRORESONATOR-BASED SOLITON FREQUENCY COMBS

- [1] S. H. Lee*, D. Y. Oh*, Q.-F. Yang*, B. Shen*, H. Wang*, K. Y. Yang, Y. H. Lai, X. Yi, and K. Vahala. “Towards visible soliton microcomb generation”. In: *arXiv preprint arXiv:1705.06703* (2017).

4.1 Abstract

Frequency combs have applications that extend from the ultra-violet into the mid infrared bands. Microcombs[8], a miniature and often semiconductor-chip-based device, can potentially access most of these applications, but are currently more limited in spectral reach. Here, we demonstrate mode-locked silica microcombs with emission near the edge of the visible spectrum. By using both geometrical and mode-hybridization dispersion control, devices are engineered for soliton generation while also maintaining optical Q factors as high as 80 million. Electronics-bandwidth-compatible (20 GHz) soliton mode locking is achieved with threshold powers as low as 5.4 mW. These are the shortest wavelength soliton microcombs demonstrated to date and could be used in miniature optical-clocks[53, 54]. The results should also extend to visible and potentially ultraviolet bands.

4.2 Introduction

Soliton microcombs[27, 28, 59, 60, 85] provide a pathway to miniaturize many conventional comb applications. They have also opened investigations into new nonlinear physics associated with dissipative Kerr solitons[27] and Stokes solitons[86]. In contrast to early microcombs, soliton microcombs eliminate instabilities, provide stable (low-phase-noise) mode locking and feature a highly reproducible spectral envelope. Many applications of these devices are being studied including chip-based optical frequency synthesis[52], secondary time standards[54] and dual-comb spectroscopy[55–57]. Also, a range of operating wavelengths is opening up by using several low-optical-loss dielectric materials for resonator fabrication. In the near-infrared (IR), microcombs based on magnesium fluoride[27], silica[28, 87] and silicon nitride[59, 60, 73, 85, 88] are being studied for frequency metrology and frequency synthesis. In the mid-IR spectral region silicon nitride[89],

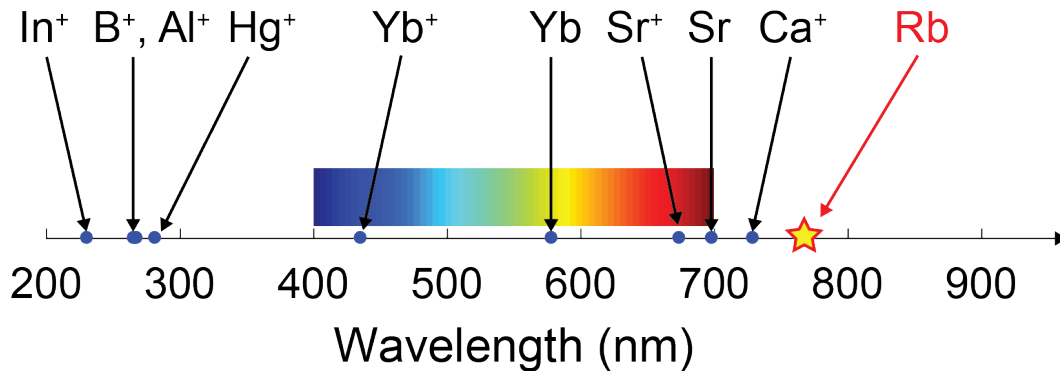


Figure 4.1: **Clock wavelengths of single ions and many neutral atoms used in optical clocks.** Wavelengths of optical transitions used in the state-of-the-art optical atomic clocks. Two-photon absorption wavelength (778 nm) of rubidium is also indicated, as the wavelength that is being explored for compact secondary time standards.

crystalline[90] and silicon-based[91] Kerr microcombs as well as quantum-cascade microcombs[92] are being studied for application to molecular fingerprinting.

At shorter wavelengths below 1 μm , microcomb technology would benefit optical atomic clock technology[93]. In optical atomic clocks, mode-locked laser frequency combs are locked to highly stable clock transitions, providing a pathway to count the optical frequencies and transfer the stability of the optical transitions to the clock rate in the microwave domain. The stability of optical atomic clocks is characterized by the fractional frequency errors ($\frac{\delta f}{f_0}$) of a stabilized local oscillator. Hence, high frequency(f_0) transitions are desirable for the stability of optical clocks. As such, the transitions of a single ion or neutral atoms used the state-of-the-art optical clocks all lie in either the visible or ultra-violet bands as shown in Figure 4.1. The best optical atomic clocks in the present have already demonstrated the accuracy that is about 100 times that of the cesium clocks serving as the primary standard of time. They make use of the mode-locked frequency combs that exhibit the highest stability and signal-to-noise, and are expected to replace the cesium clocks in the future redefinition of the SI second.

At the same time, there are growing interests to develop miniaturized optical clocks that can serve as secondary time standards. Some key characteristics of these miniaturized optical clocks include small size, weight and power (SWaP). These clocks can enhance the time-keeping ability in the environment where GPS signal cannot reach, and can be readily deployed in large-scales because of their portability.

Due to their SWaP requirement, microcombs are replacing the conventional mode-locked laser frequency combs, functioning as the frequency counter of the optical clock transition. For example, microcomb optical clocks based on the D1 transition (795 nm) and the two-photon clock transition[94] (778 nm) in rubidium have been proposed[53, 54]. In 2014, a microcomb clock using two-point locking to rubidium D1 and D2 lines has been demonstrated[9] by frequency doubling from the near-IR. Currently, our research group is actively developing soliton microcombs to be integrated in compact optical clocks based on the rubidium two-photon transition at 778 nm (See Figure 4.1).

It is also possible that these soliton microcombs operating at shorter wavelength could be applied in optical coherence tomography (OCT)[95–97]. Wavelength 600 - 1300 nm is viewed as the most promising spectral band for biomedical imaging because of the low absorption of the light by water and blood. Portable frequency combs covering this spectral window can therefore even find clinical applications.

So far, efforts directed towards short wavelength microcomb operation include 1 μm microcombs in silicon nitride microresonators[98] as well as harmonically-generated combs. The latter have successfully converted near IR comb light to shorter wavelength bands[99] and even into the visible band[100, 101] within the same resonator used to create the initial comb of near-IR frequencies. Also, crystalline resonators[102] and silica microbubble resonators[103] have been dispersion-engineered for comb generation in the 700 nm band. Finally, diamond-based microcombs afford the possibility of broad wavelength coverage[63]. However, none of the short wavelength microcomb systems have so far been able to generate stable mode-locked microcombs as required in all comb applications.

A key impediment to mode-locked microcomb operation at short wavelengths is material dispersion associated with the various dielectric materials used for microresonator fabrication. At shorter wavelengths, these materials feature large normal dispersion that dramatically increases into the visible and ultraviolet bands. Soliton-based mode-locking, on the other hand, requires anomalous dispersion. Dispersion engineering by proper design of the resonator geometry[53, 102–109] offers a possible way to offset the normal dispersion. Typically, by compressing a resonator's waveguide dimension, geometric dispersion will ultimately compensate a large normal material dispersion component to produce overall anomalous dispersion. For example, in silica, strong confinement in bubble resonators[103] and straight waveguides[110] has been used to push the anomalous dispersion transition

wavelength from the near-IR into the visible band. Phase matching to ultraviolet dispersive waves has also been demonstrated using this technique[110]. However, to compensate the rising material dispersion this compression must increase as operational wavelength is decreased, and as a side effect highly-confined waveguides tend to suffer increased optical losses. This happens because mode overlap with the dielectric waveguide interface is greater with reduced waveguide cross section. Consequently, the residual fabrication-induced roughness of that interface degrades the resonator Q factor and increases pumping power (i.e., comb threshold power varies inverse quadratically with Q factor[30]).

Minimizing material dispersion provides one way to ease the impact of these constraints. In this sense, silica offers an excellent material for short wavelength operation, because it has the lowest dispersion among all on-chip integrable materials. For example, at 778 nm, silica has a group velocity dispersion (GVD) equal to 38 ps²/km, which is over 5X smaller than the GVD of silicon nitride at this wavelength (> 200 ps²/km)[111]. Other integrable materials that are also transparent in the visible, such as diamond[63] and aluminum nitride[61], have dispersion that is similar to or higher than silicon nitride. Silica also features a spectrally-broad low-optical-loss window so that optical Q factors can be high at short wavelengths. Here we demonstrate soliton microcombs with pump wavelengths of 1064 nm and 778 nm. These are the shortest soliton microcomb wavelengths demonstrated to date. By engineering geometric dispersion and by employing mode hybridization, net anomalous dispersion has been achieved at these wavelengths while also maintaining high optical Q factors (80 million at 778 nm, 90 million at 1064 nm). The devices have large (millimeter-scale) diameters and produce single soliton pulse streams at rates that are both detectable and processible by low-cost electronic circuits. Besides illustrating the flexibility of silica for soliton microcomb generation across a range of short wavelengths, these results are relevant to potential secondary time standards based on transitions in rubidium[9, 53, 54]. Using dispersive-wave engineering in silica it might also be possible to extend the emission of these combs into the ultraviolet as recently demonstrated in compact silica waveguides[110]. As an aside, we note that a waveguide-integrated version of this design is also possible[112]. Adaptation of that device using the methods described here would enable full integration with other photonic elements on the silicon chip.

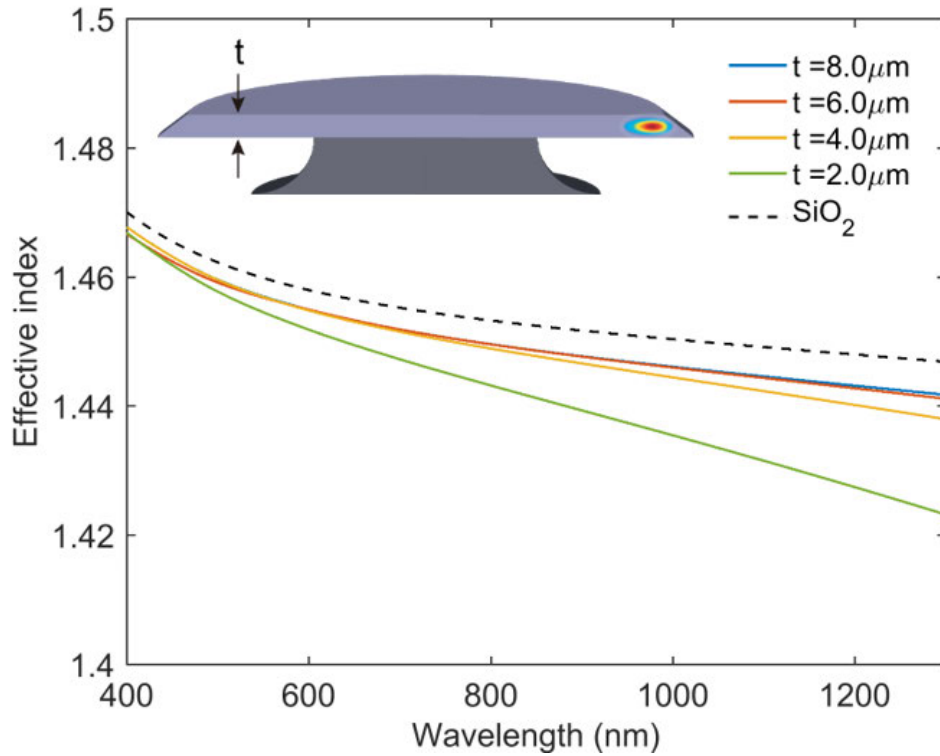


Figure 4.2: **Effective index of fundamental TM mode (TM1) of silica wedge resonators for various thickness t** Effective index of TM1 mode of the resonator versus wavelength is plotted for various thickness t . The dashed line is the refractive index of fused silica based on the Sellmeier equation. A schematics of silica wedge resonator is shown as an inset to the figure.

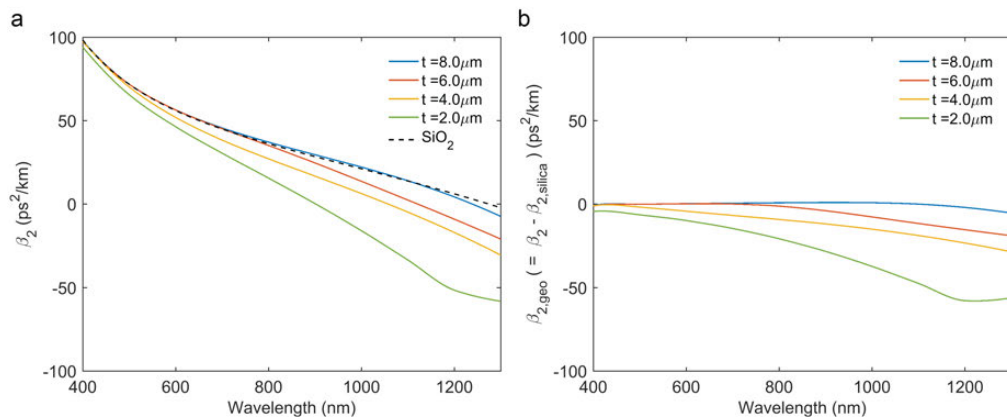


Figure 4.3: **Calculated dispersion of the TM1 mode** (a) Total dispersion(β_2) is plotted versus wavelength for various t . The dashed line indicates the material dispersion of silica (b) Geometrical dispersion($\beta_{2,geo}$), defined as the total dispersion(β_2) subtracted by the material dispersion of silica dispersion(β_{2,SiO_2})

4.3 Dispersion engineering of silica microresonators

The silica resonator used in this work is shown schematically as an inset to Figure 4.2. A fundamental mode profile is overlaid in the cross-sectional rendering. As described in detail below, the resonator thickness (t) is controlled to obtain net anomalous dispersion at the design wavelengths, a prerequisite for bright soliton generation. The resonator design is a variation on the wedge resonator[29] and precise thickness control (t -control) is possible because this layer is formed through thermal oxidation of a silicon wafer (See Section 2.5 and for further details). The diameter of all resonators in this work (and the assumed diameter in all simulations) is 3.2 mm, which corresponds to a free-spectral-range (FSR) of approximately 20 GHz.

Calculation of dispersion using FEM method

The group velocity dispersion β_2 is defined as the second derivative of the propagation constant β with respect to the angular frequency ω . (i.e., $\beta_2 = \frac{d^2\beta}{d\omega^2}$) Since the propagation constant is related to the effective index of the mode as $\beta = \frac{2\pi}{\lambda}n_{\text{eff}}$, the following relationship between the dispersion and the effective is found.

$$\beta_2(\lambda) = \frac{\lambda^3}{2\pi c^2} \frac{d^2 n_{\text{eff}}}{d\lambda^2} \quad (4.1)$$

The total dispersion is the sum of the material dispersion of silica (β_{2,SiO_2}) and the geometrical dispersion ($\beta_{2,\text{geo}}$) of the resonator mode. The material dispersion of silica can be derived from its Sellmeier equation:

$$\beta_{2,\text{SiO}_2}(\lambda) = \frac{\lambda^3}{4\pi n c^2} \sum_{i=1}^3 A_i B_i \left[\frac{1}{(\lambda - B_i)^3} - \frac{1}{(\lambda + B_i)^3} \right] \quad (4.2)$$

where $A_1 = 0.6961663$, $A_2 = 0.4079426$, $A_3 = 0.8974794$, $B_1 = 0.0684043\mu\text{m}$, $B_2 = 0.1162414\mu\text{m}$, and $B_3 = 9.896161\mu\text{m}$ for fused silica[113].

The effective indices of the fundamental TM mode of the silica wedge resonator for various thickness t and wavelength are calculated using an axisymmetric model in FEM simulations (COMSOL) and plotted in Figure 4.2. The corresponding total dispersion (β_2) and geometrical dispersion ($\beta_{2,\text{geo}} \equiv \beta_2 - \beta_{2,\text{SiO}_2}$) are obtained using Equation 4.1 and 4.2. The results are given in Figure 4.3.

Qualitative description of the dispersion

The geometrical dispersion of the silica wedge resonator is related to the position of the mode intensity maximum. First, let us consider the case of a $8\mu\text{m}$ -thick

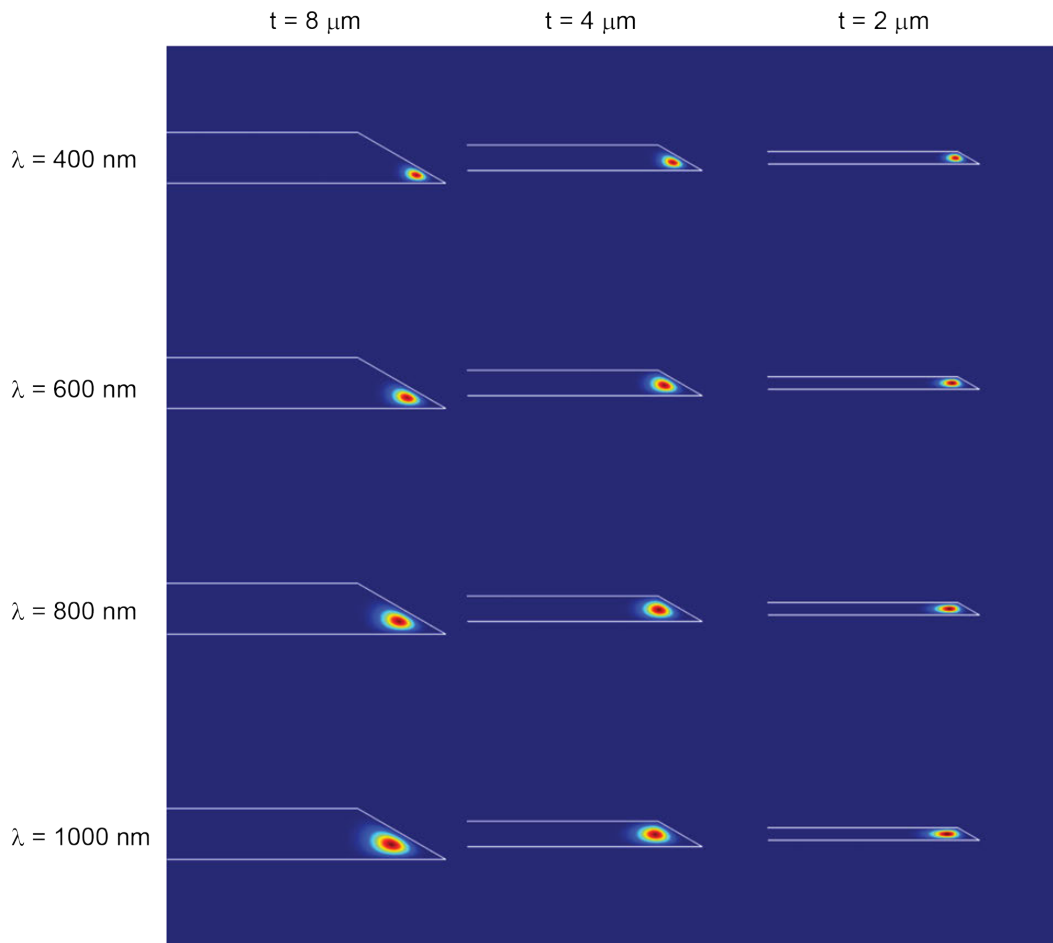


Figure 4.4: **Calculated electric field intensity of TM1 mode of the resonator for various thickness t and wavelengths λ .** Mode field intensity for $t = 8, 4, 2 \mu\text{m}$ and $\lambda = 400, 600, 800, 1000 \text{ nm}$ is shown. The wedge angle is fixed at 30 degree for these simulations. At small t and/or large λ , the radial position of the mode intensity maximum moves out of the wedge, and its vertical position does not change any more. In this regime, the geometrical dispersion of the mode is anomalous (See the main text for further details).

resonator (left column of Figure 4.4). At wavelength 400 nm, the mode is confined near the tip of the wedge. As the wavelength increases from 400 nm to 1000 nm, the mode area grows quadratically and the mode retreats inside a little bit. However, the geometrical dispersion of the mode is close to 0 in this case (See blue curve in Figure 4.3b). This is because the mode experiences the geometry of the resonator spatially close to the mode location, and the shape of the resonator further away does not influence the properties of the mode. Throughout wavelength 400 - 1000 nm, the mode sees the lateral and the bottom surfaces of the wedge, but it does not see the top surface. In this regime, the wedge mode can be approximated by the mode

of a conical resonator, the limiting case when the lateral wedge surface is extended to the end. In fact, if we normalize the resonator dimensions by the wavelength, the variation in the wavelength translates into the variation in the resonator radius. The effective index of the mode is insensitive to the variation in the resonator radius in this regime, which accounts for the near absence of geometrical dispersion.

However, as the wavelength further increases, the mode retreats inward and eventually starts seeing the top surface. Once the mode moves out of the wedge and mainly sees the top and the bottom surfaces but not the lateral surface, the effective index decreases quickly as the wavelength increases. In addition, the rate of the change of the effective index becomes faster at larger wavelength because the mode experiences a tight vertical confinement. As a result, the geometrical dispersion becomes anomalous in this regime.

Now, at a given wavelength, the mode becomes close to the top surface with reduced t . As t decreases, the wavelength at which the $\beta_{2,\text{geo}}$ changes from being normal ($\beta_{2,\text{geo}} > 0$) to anomalous ($\beta_{2,\text{geo}} < 0$) blue-shifts. With the augmented anomalous geometrical dispersion with small t , the net anomalous dispersion window can be pushed down to the near visible and even visible wavelengths.

4.4 Design of soliton devices at pump wavelength 1550 nm, 1064 nm and 778 nm

Figure 4.5a illustrates the dispersion design space by showing regions of anomalous and normal dispersion for the TM₁ mode family versus resonator thickness t and pumping wavelength. The plot shows that as the pump wavelength decreases the resonator needs to be thinner to access the anomalous dispersion regime. With this in mind, we have selected three different device types for soliton frequency comb operation at three different pump wavelengths. These are indicated in Figure 4.5a as I, II and III with colored dots. At a pump wavelength of 1550 nm, the anomalous dispersion window is wide because bulk silica possesses anomalous dispersion at wavelengths above 1270 nm. For this device (Type I), an 8- μm thickness was used. Devices of type II and III have thicknesses near 3.5 μm and 1.5 μm for operation with pump wavelengths of 1064 nm and 778 nm, respectively. Scanning electron microscope (SEM) images appear in Figure 4.5b and provide cross-sectional views of the three device types. Measured Q factors for the three device types are plotted in the upper panel of Figure 4.6. Maximum Q factors at thicknesses which also produce anomalous dispersion were 280 million (Type I, 1550 nm), 90 million

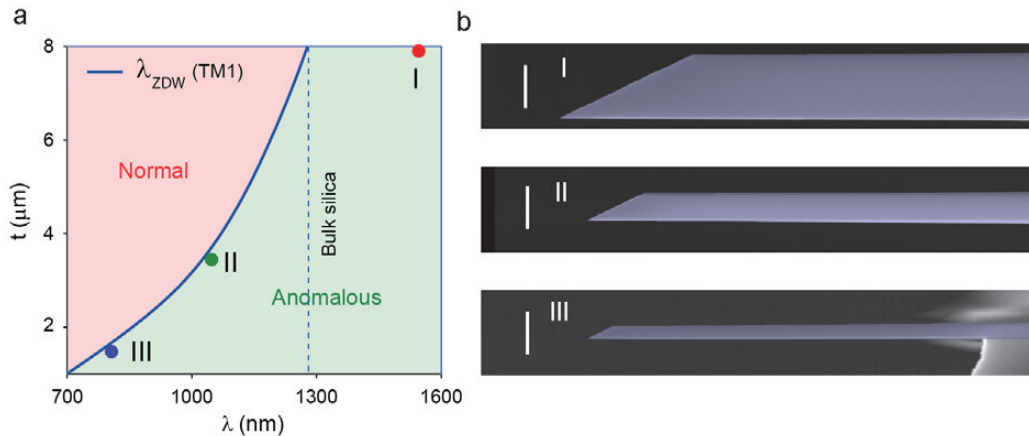


Figure 4.5: **Fabricated silica wedge resonator devices that feature anomalous dispersion at pump wavelength 1550 nm, 1064 nm and 778 nm.** (a) Regions of normal and anomalous dispersion are shown versus silica resonator thickness (t) and pump wavelength. The zero dispersion wavelength (λ_{ZDW}) for the TM1 mode appears as a blue curve. Plot is made for a 3.2-mm-diameter silica resonator. Three different device types I, II and III (corresponding to three oxide thicknesses) are indicated for soliton generation at 1550 nm, 1064 nm and 778 nm. (b) Cross-sectional SEM images of the fabricated resonators. White scale bar is $5 \mu\text{m}$.

(Type II, 1064 nm) and 80 million (Type III, 778 nm).

Using these three designs, soliton frequency combs were successfully generated with low threshold pump power. Figure 4.7 shows optical spectra of the soliton microcombs generated for each device type. A slight Raman-induced soliton self-frequency-shift is observable in the type I and type II devices[28, 114–116]. It is worthwhile to note that microcomb threshold power, expressed as $P_{th} \sim A_{eff}/\lambda_p Q^2$ (λ_p is pump wavelength and A_{eff} is effective mode area) remains within a close range of powers for all devices (lower panel of Figure 4.6). This can be understood to result from partial compensation of reduced Q factor in the shorter wavelength devices by reduced optical mode area (see plot in Figure 4.5). For example, from 1550 nm to 778 nm the mode area is reduced by roughly a factor of 9 and this helps to offset a decrease in Q factor of 3X. The resulting P_{th} increase (5.4 mW at 778 nm versus approximately 2.5 mW at 1550 nm) is therefore caused primarily by the decrease in pump wavelength λ_p . In the following sections additional details on the device design, dispersion and experimental techniques used to generate these solitons at $1 \mu\text{m}$ and 778 nm bands are presented.

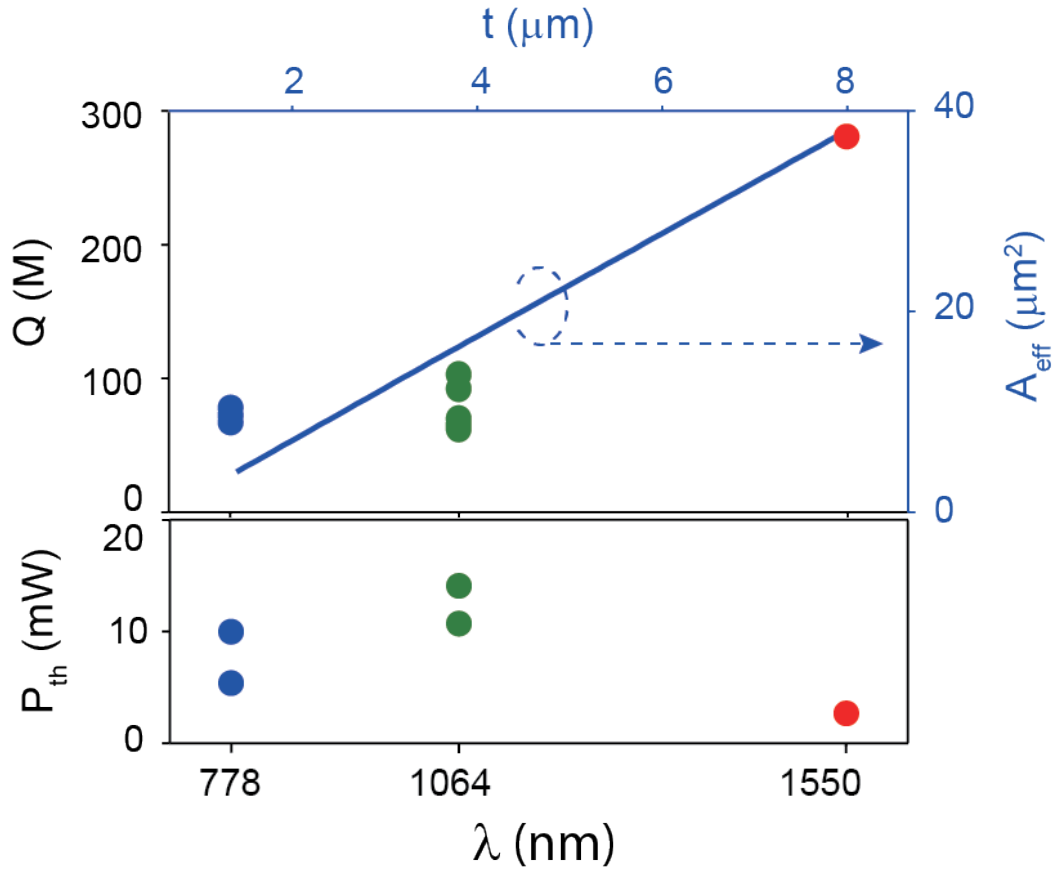


Figure 4.6: **Measured Q factors and comb threshold powers versus thickness and pump wavelength for the three device types.** Effective mode area (A_{eff}) of the TM1 mode family is also plotted as a function of wavelength and thickness.

4.5 Soliton frequency comb generation using 1 μm pump

Dispersion simulations for TM modes near 1064 nm are presented in Figure 4.8a and show that TM modes with anomalous dispersion occur in silica resonators having oxide thicknesses less than 3.7 μm . Aside from the thickness control, a secondary method to manipulate dispersion is by changing the wedge angle (see Figure 4.8). Here, wedge angles between 30 and 40 degrees were chosen in order to maximize the Q factors[29]. The resonator dispersion is characterized by measuring mode frequencies using a scanning external-cavity-diode-laser (ECDL) whose frequency is calibrated using a Mach-Zehnder interferometer. As described elsewhere[27, 28] the mode frequencies, ω_{μ} , are Taylor expanded to second order as $\omega_{\mu} = \omega_0 + \mu D_1 + \mu^2 D_2/2$, where ω_0 denotes the pumped mode frequency and $D_1/2\pi$ is the FSR. D_2 is related to the GVD, β_2 , by $D_2 = -cD_1^2\beta_2/n_0$ where c and n_0 are the speed of light and material refractive index, respectively. The measured frequency

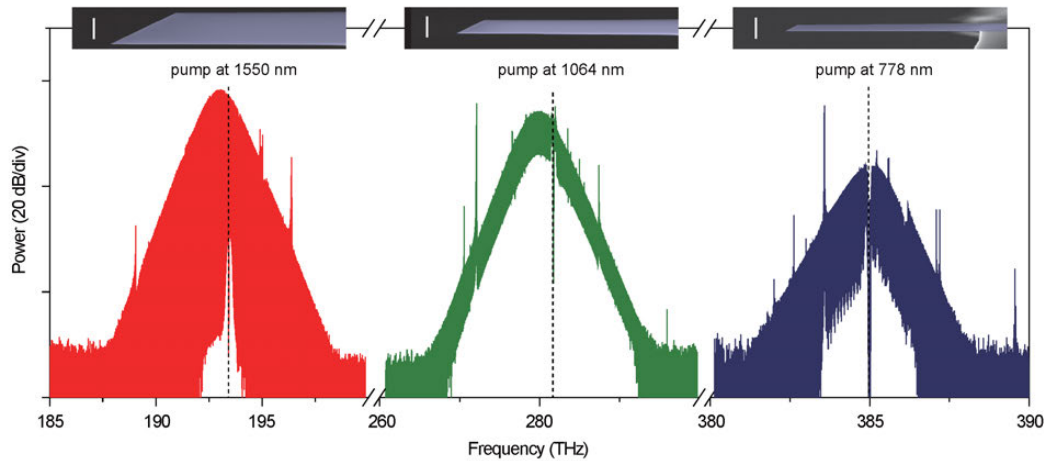


Figure 4.7: **Soliton frequency combs at pump wavelength 1550 nm, 1064 nm and 778 nm** Soliton frequency comb spectra measured using device types I, II and III designed for pump wavelengths 1550 nm, 1064 nm, and 778 nm, respectively. Pump frequency location is indicated by a dashed vertical line. The soliton pulse repetition rate of all devices is about 20 GHz. Insets: cross-sectional SEM images of the fabricated resonators. White scale bar is 5 μm .

spectrum of the TM1 mode family in a 3.4 μm thick resonator is plotted in Figure 4.8b. The plot gives the frequency as relative frequency (i.e., $\omega_\mu - \omega_0 - \mu D_1$) to make clear the second-order dispersion contribution. Also shown is a fitted parabola (red curve) revealing $D_2/2\pi = 3.3$ kHz (positive parabolic curvature indicates anomalous dispersion). Some avoided mode crossings are observed in the spectrum. The dispersion measured in resonators of different thicknesses, marked as solid dots in Figure 4.8a, is in good agreement with numerical simulations.

The experimental setup for generation of 1064 nm pumped solitons is shown in Figure 4.9. The microresonator is pumped by a CW laser amplified by a YDFA. The pump light and comb power are coupled to and from the resonator by a tapered fiber[49, 70]. Solitons are generated while scanning the laser from higher frequencies to lower frequencies across the pump mode[27, 28, 85]. The pump light is modulated by an electro-optic phase modulator to overcome the thermal transient during soliton generation[28, 78, 85]. A servo control referenced to the soliton power is employed to capture and stabilize the solitons[78]. Shown in Figure 4.10 are the optical spectra of solitons pumped at 1064 nm. These solitons are generated using the mode family whose dispersion is characterized in Figure 4.8b. Due to the relatively low dispersion (small D_2), these solitons have a short temporal pulsewidth. Using the hyperbolic-secant-squared fitting method (see orange and green curves in

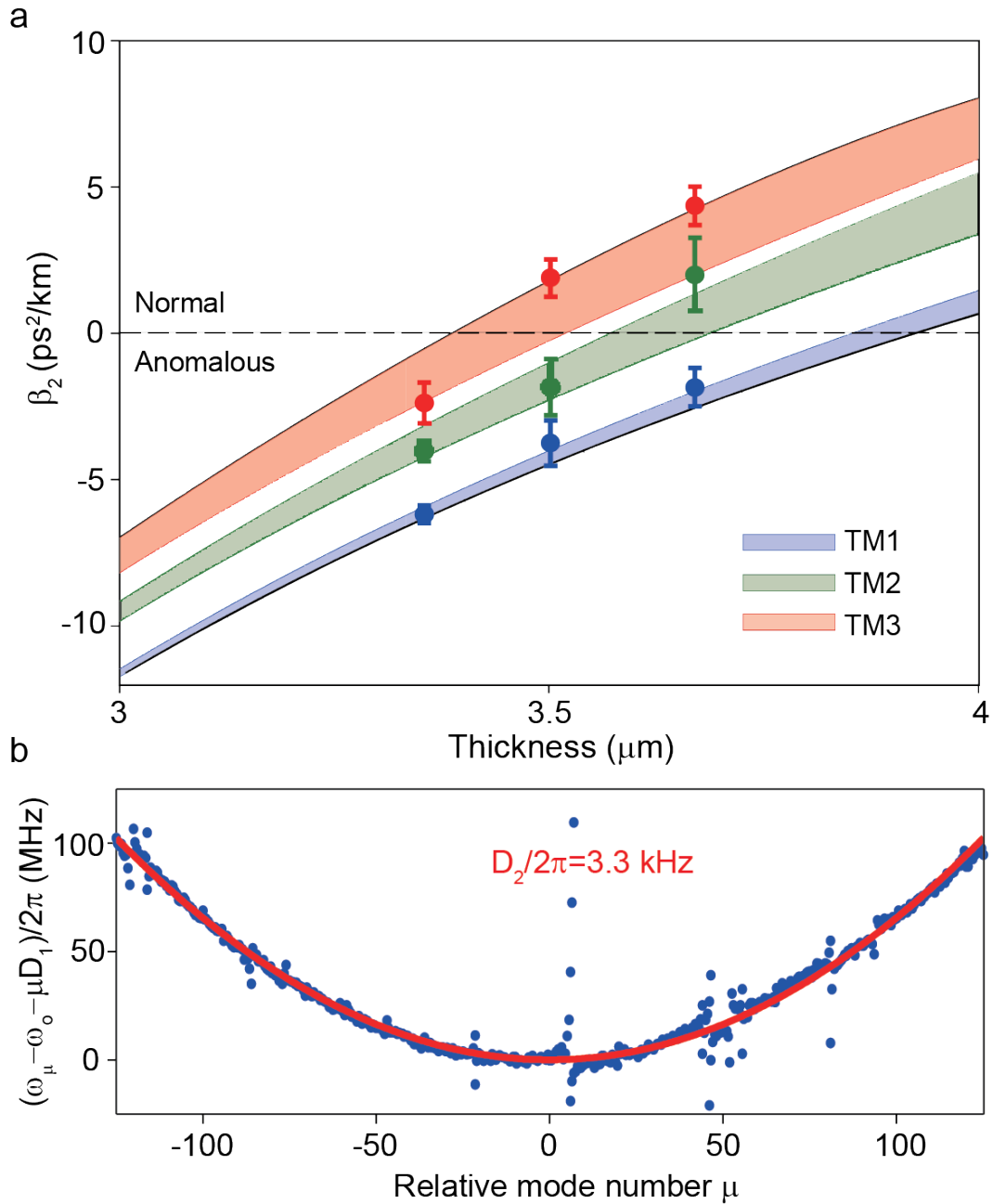


Figure 4.8: **Microresonator dispersion engineering at 1064 nm.** (a) Simulated dispersion (GVD) of TM mode families versus resonator thickness. The angle of the wedge ranges from 30° to 40° in the colored regions. Measured data points are indicated and agree well with the simulation. (b) Measured relative mode frequencies (blue points) plotted versus relative mode number of a soliton-forming TM1 mode family in a $3.4 \mu\text{m}$ thick resonator. The red curve is a parabolic fit yielding $D_2/2\pi = 3.3$ kHz.

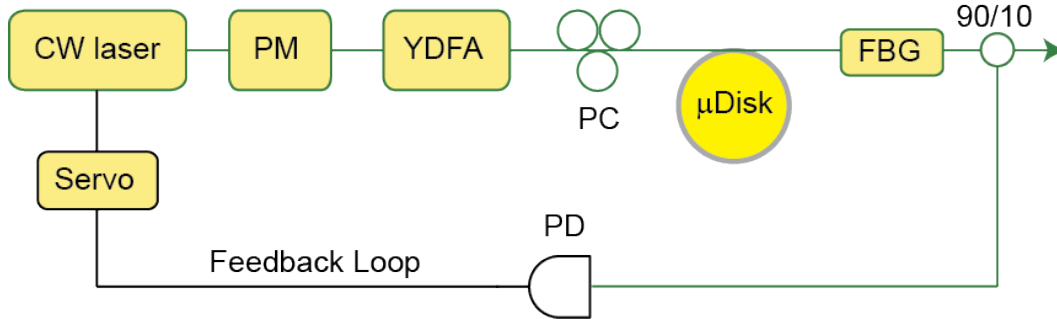


Figure 4.9: **Experimental setup for soliton generation.** A continuous-wave (CW) fiber laser is modulated by an electro-optic phase modulator (PM) before coupling to a ytterbium-doped-fiber-amplifier (YDFA). The pump light is then coupled to the resonator using a tapered fiber. Part of the comb power is used to servo-lock the pump laser frequency. FBG: fiber Bragg grating. PD: photodetector. PC: polarization controller.

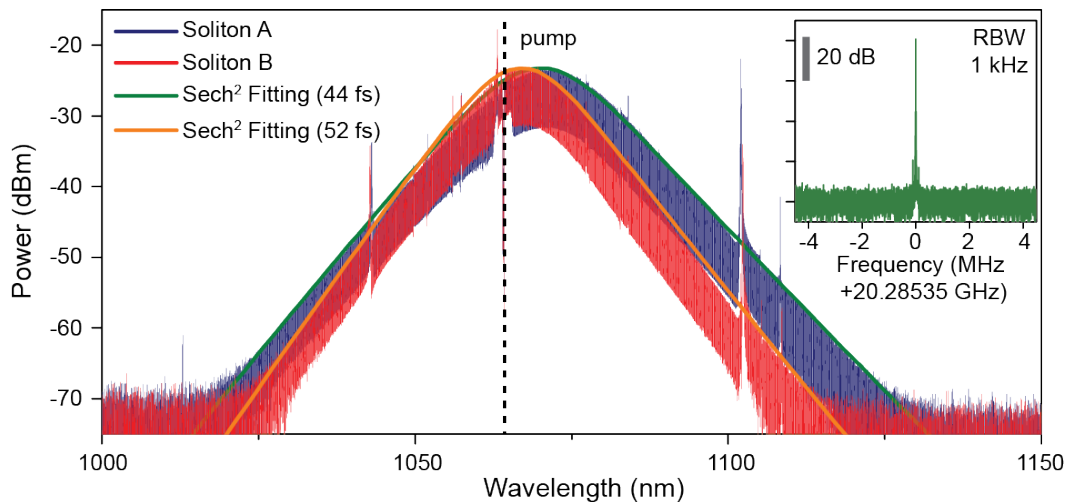


Figure 4.10: **Soliton generation at 1064 nm.** Optical spectra of solitons at 1064 nm generated from the mode family shown in 4.8 (b). The two soliton spectra correspond to different power levels with the blue spectrum being a higher power and wider bandwidth soliton. The dashed vertical line shows the location of the pump frequency. The solid curves are sech^2 fittings. Inset: typical detected electrical beatnote showing soliton repetition rate. RBW: resolution bandwidth.

Figure 4.10) a soliton pulse width of 52 fs is estimated for the red spectrum. By increasing the soliton power (blue spectrum) the soliton can be further compressed

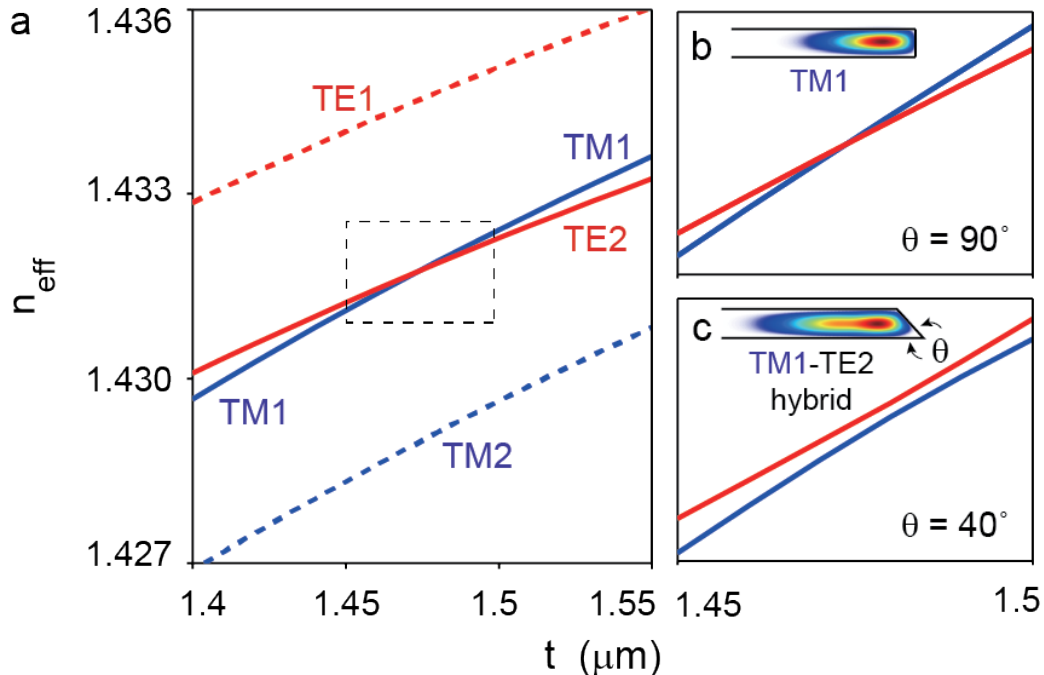


Figure 4.11: **Mode hybridization at 778 nm illustrated by the effective indices of the resonator modes** (a) Calculated effective indices for TE1, TE2, TM1 and TM2 modes at 778 nm plotted versus thickness for a silica resonator with reflection symmetry. The TM1 and TE2 modes cross each other without hybridization. The dashed box is the frame for the panel **b** zoom-in. (b) Zoom-in of the dashed box in panel **a**. Inset shows resonator with reflection symmetry (equivalent to wedge angle $\theta = 90^\circ$). (c) As in **b** but for resonator with $\theta = 40^\circ$. An avoided crossing of TM1 and TE2 occurs due to mode hybridization.

to 44 fs, which corresponds to a duty cycle of 0.09% at the 20 GHz repetition rate. Finally, the inset in Figure 4.10 shows the electrical spectrum of the photodetected soliton pulse stream. Besides confirming the repetition frequency, the spectrum is very stable with excellent signal-to-noise ratio (SNR) greater than 70 dB at 1 kHz RBW.

4.6 Soliton frequency comb generation using 778 nm pump

For soliton operation near the pump wavelength 778 nm, a resonator thickness around $1.5 \mu\text{m}$ is chosen, which is close to the zero GVD of the TM1 mode (see Figure 4.5a). Operation at this point provides thicker oxide and therefore higher optical Q factors. Under normal circumstances the near-zero GVD would prove challenging to control during fabrication, so mode coupling is used to further engineer the dispersion[53,

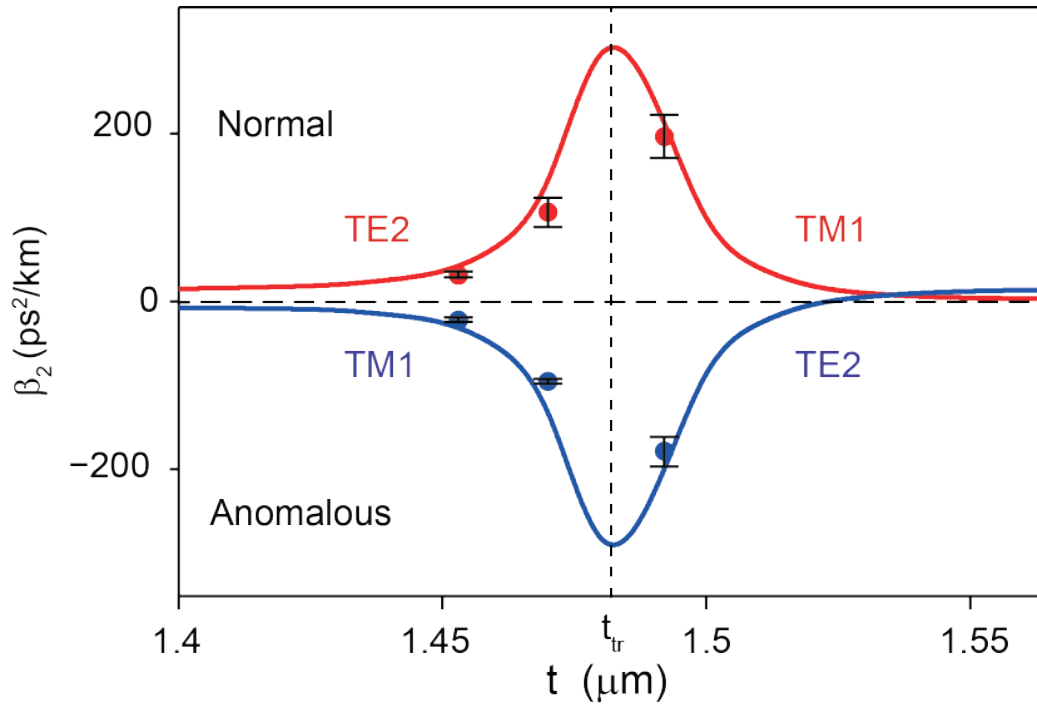


Figure 4.12: **Calculated GVD of the two hybrid modes for $\theta = 40^\circ$.** Hybridization causes a transition in the dispersion around the thickness $t_{tr} = 1.48\mu\text{m}$. The points are the measured dispersion values.

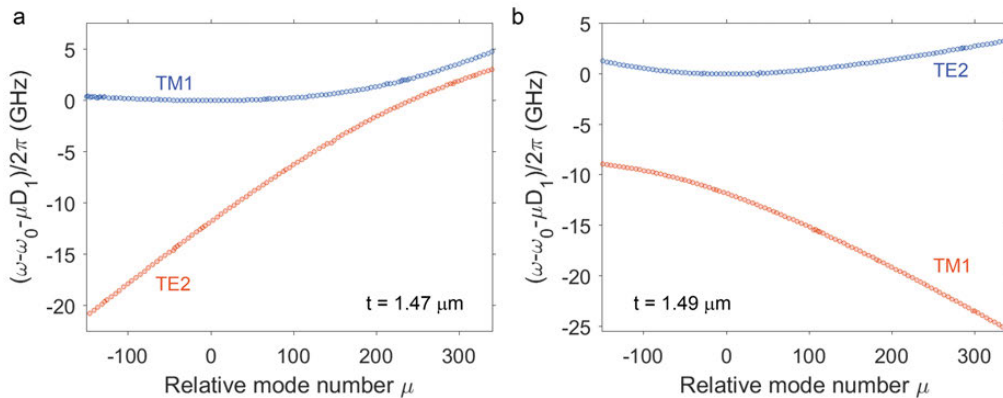


Figure 4.13: **Measured mode frequencies of the hybrid modes** (a) Measured relative mode frequencies of the TM1 and TE2 mode families versus relative mode number μ for devices with $t = 1.47$. The thickness is below the transition thickness t_{tr} and the TM1 mode is anomalous. (b) As in (a) but for $t = 1.49\mu\text{m}$. The thickness is above the transition thickness t_{tr} and the TE2 mode is anomalous.

106, 107, 118]. Specifically, the anomalous dispersion of the TM1 mode is boosted through hybridization with the TE2 mode. As now shown, this mode hybridization is caused by two factors: a degeneracy in the effective index at the pump wavelength

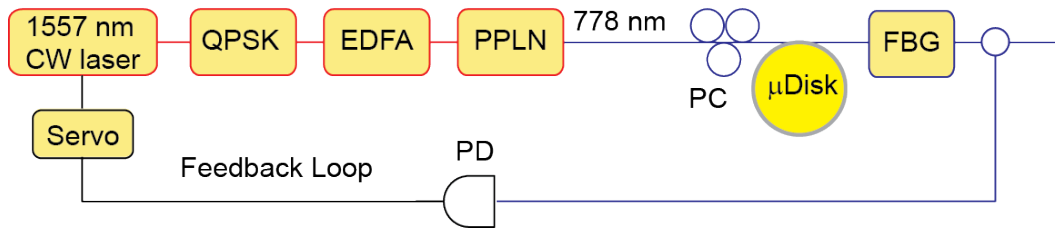


Figure 4.14: **Experimental setup for soliton generation at 778 nm.** A 1557 nm tunable laser is sent to a quadrature phase shift keying modulator (QPSK) to utilize frequency-kicking[117] and is then amplified by an erbium-doped-fiber-amplifier (EDFA). Then, a periodically poled lithium niobate (PPLN) waveguide frequency doubles the 1557 nm input into 778 nm output. The 778 nm pump light is coupled to the resonator for soliton generation. A servo loop is used to maintain pump locking[78].

of the two modes and a broken reflection symmetry of the resonator[119].

Finite element method (FEM) simulation in Figure 4.11 shows that at 778 nm the TM1 and TE2 modes are expected to have the same effective index at the thickness $1.48 \mu\text{m}$ when the resonator features a symmetry upon reflection through a plane that is both parallel to the resonator surface and that lies at the center of the of resonator. Such a symmetry exists when the resonator has vertical sidewalls or equivalently a wedge angle $\theta = 90^\circ$ in the current resonator design. A zoom-in of the effective index crossing is provided in Figure 4.11b. In this symmetrical case, the two modes cross in the effective-index plot without hybridization. However, in the case of $\theta = 40^\circ$ (Figure 4.11c, the symmetry is broken and the point of effective index degeneracy does not exist. Instead, near the resonator thickness $1.48 \mu\text{m}$, two hybrid modes exist and these modes experience an avoided crossing. The avoided crossing causes a sudden transition in the calculated group velocity dispersion as shown in Figure 4.12. One of the hybrid modes experiences enhanced anomalous dispersion, while the other mode experiences enhanced normal dispersion. At the thickness below the transition thickness $t_{tr} = 1.48 \mu\text{m}$, the dispersion of the TM1 mode is anomalous and that of the TE2 mode is normal. At the thickness above t_{tr} , however, the dispersion of each mode family changes its sign.

To verify this effect, resonators with three different thicknesses were fabricated and their dispersion was characterized using the same method as for the 1064 nm soliton device. The measured second-order dispersion values are plotted as solid circles in Figure 4.12 for comparison with the calculated values. In addition to second-order dispersion, the mode spectra of the two modes feature significant higher-order

dispersion (β_3 and β_4) around the thickness $1.48 \mu\text{m}$. Figure 4.13a and Figure 4.13b show the measured relative mode frequencies versus mode number of the two modes for devices with $t = 1.47 \mu\text{m}$ and $t = 1.49 \mu\text{m}$, respectively. A zoom-in of the TM1 mode spectrum for $t = 1.47 \mu\text{m}$ with a fit which includes third-order dispersion (red curve) is shown in Figure 4.15a. Despite the third-order dispersion, this dispersion curve is well suited for soliton formation.

For soliton generation, the microresonator is pumped at 778 nm by frequency-doubling from a CW ECDL operating at 1557 nm (see Figure 4.14). The 1557 nm laser is modulated by a QPSK modulator for frequency-kicking[117] and then amplified by an EDFA. The amplified light is sent into a PPLN device for second-harmonic generation. The frequency-doubled output pump power at 778 nm is coupled to the microresonator using a tapered fiber. The soliton capture and locking method was again used to stabilize the solitons[78]. The optical spectrum of a 778 nm pumped soliton is shown in Figure 4.15b. It features a temporal pulse width of 145 fs as derived from a sech^2 fit. The red line in the figure is the calculated comb envelope from the simulation of Lugiato-Lefever Equation (LLE). The corresponding soliton pulse width from the simulation is 139 fs , agreeing well with the pulse width estimation based on the measured spectrum. The electrical spectrum of the photodetected soliton stream is provided as the inset to Figure 4.15b and exhibits high stability.

The short wavelength extent of a soliton spectrum can further be pushed by using a resonator with a small D_2 value. Here, we choose a resonator with thickness $t = 1.51 \mu\text{m}$ whose TE2 mode features an anomalous dispersion with $D_2/2\pi = 4.8 \text{ kHz}$ (See Figure 4.16a). The soliton was captured using the same technique and its optical and electrical spectra are shown in Figure 4.16b. The asymmetry in the optical spectrum is caused by the strong third-order dispersion. A mode-interaction induced dispersive wave is located at 757 nm , boosting the spectral intensity of the soliton at the short wavelength edge.

4.7 Summary

In summary, soliton microcombs at 778 nm and 1064 nm using on-chip high-Q silica resonators were demonstrated for the first time. Material-limited normal dispersion, which is dominant at these wavelengths, was compensated by using geometric dispersion through control of the resonator thickness and wedge angle. At the shortest wavelength, 778 nm , mode hybridization was also utilized to

achieve anomalous dispersion while maintaining high optical Q. These results are the shortest wavelength soliton microcombs demonstrated to date. The generated solitons have pulse repetition rates of 20 GHz at both wavelengths. Such detectable and electronics-compatible repetition rate soliton microcombs at short wavelengths have direct applications in the development of miniature optical clocks[9, 53, 54] and potentially optical coherence tomography[95–97]. Also, any application requiring low-power near-visible mode-locked laser sources will benefit. The same dispersion control methods used here should be transferable to silica ridge resonator designs that contain silicon nitride waveguides for on-chip coupling to other photonic devices[112]. Also, it could be possible to design devices that use solitons formed at either 778 nm or 1064 nm for dispersive-wave generation into the visible and potentially into the ultraviolet as has been recently demonstrated using straight silica waveguides[110].

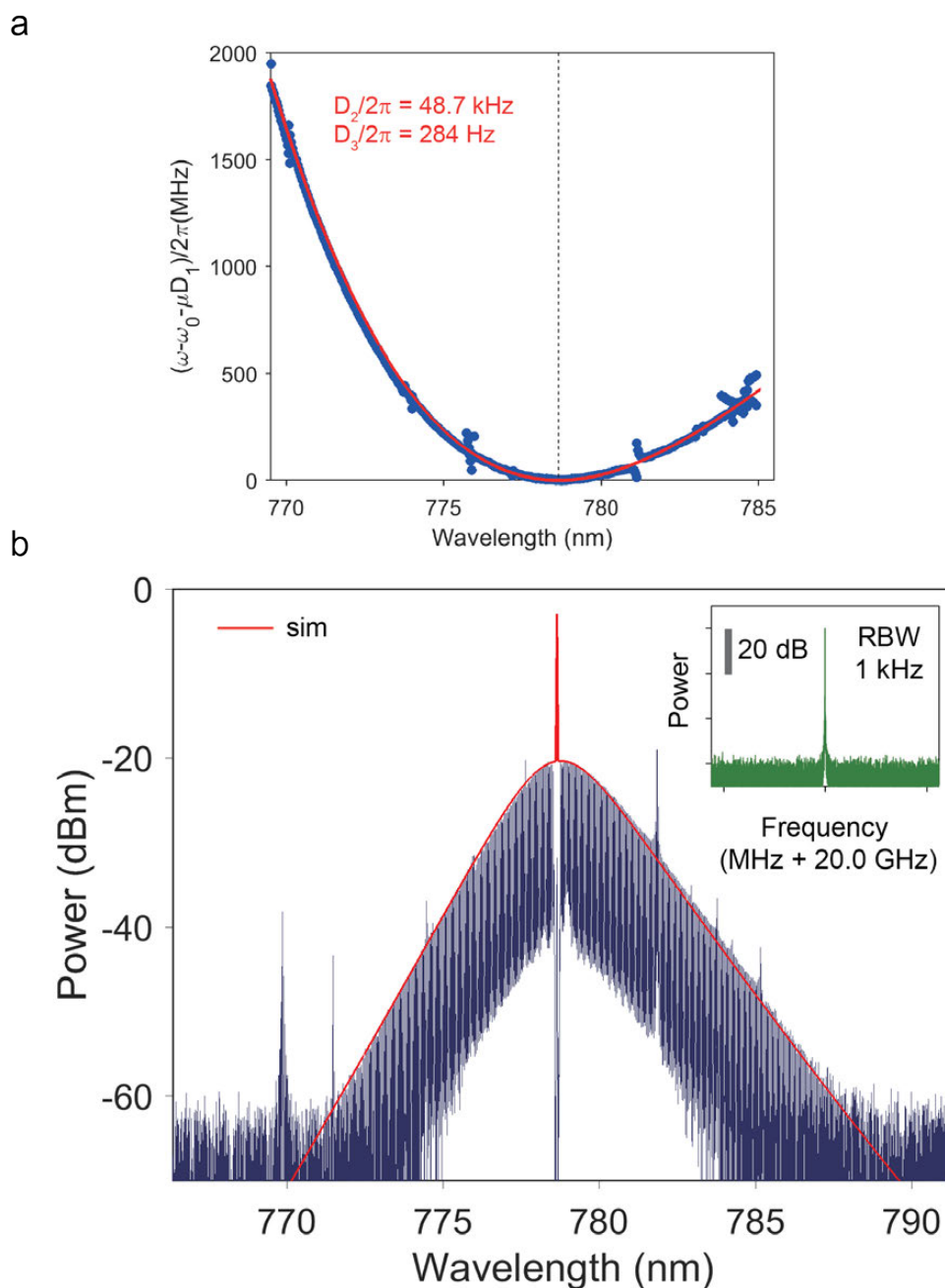


Figure 4.15: **First soliton microcomb demonstration at 778 nm** (a) Measured mode frequencies of the TM1 mode family plotted versus wavelength for a $t = 1.47 \mu\text{m}$ device. The pump wavelength is indicated as a dashed line. The spurs in the data are due to the crossing with other mode families. (b) Optical spectrum of a soliton with pump line (778.7 nm) indicated. The red curve is a simulation using the Lugiato-Lefever equation including the Raman terms, which deviates slightly from the sech^2 envelope due to the higher order dispersion. The spectral location of observed dispersive waves match well with the mode crossing locations in **a**, revealing that the dispersive waves are induced by spatial mode-interactions[[yang2016spatial.](#)] Inset shows the electrical spectrum of the detected soliton pulse stream.

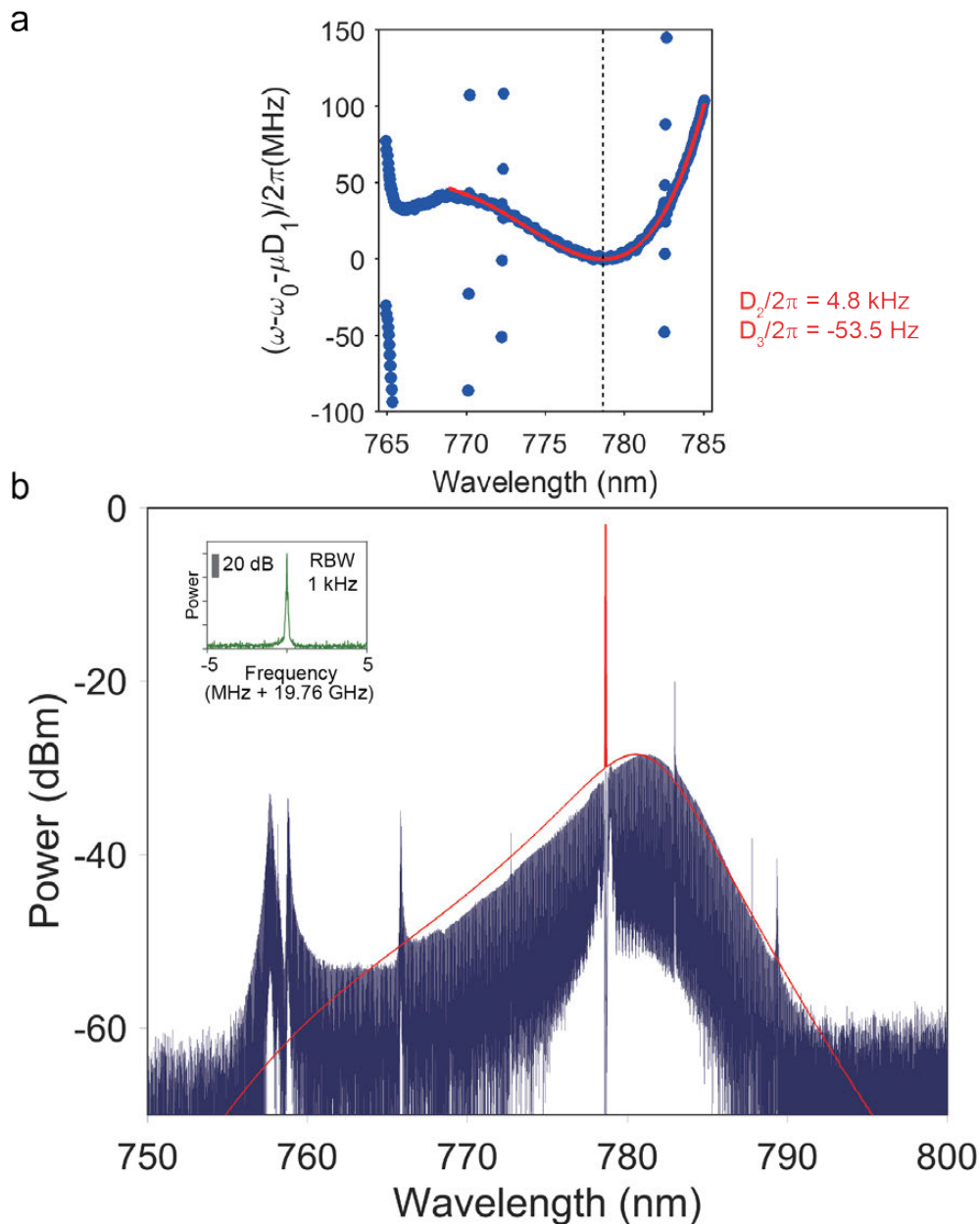


Figure 4.16: **Generation of a soliton microcomb that spans wavelengths 755 - 793 nm.** (a) Measured mode frequencies of the TM1 mode family plotted versus wavelength for a $t = 1.50 \mu\text{m}$ device. (b) Optical spectrum of a soliton with pump line (778.7 nm) indicated. The red curve is a simulation using Lugiato-Lefever equation including the Raman terms. Inset shows the electrical spectrum of the detected soliton pulse stream.

SUPERCONTINUUM GENERATION IN ULTRA-LOW-LOSS SILICA WAVEGUIDES

- [1] **D. Y. Oh**, D. Sell, H. Lee, K. Y. Yang, S. A. Diddams, and K. J. Vahala. “Supercontinuum generation in an on-chip silica waveguide”. In: *Optics letters* 39.4 (2014), pp. 1046–1048. DOI: 10.1364/OL.39.001046.

5.1 Abstract

Supercontinuum generation is demonstrated in an on-chip silica spiral waveguide by launching 180-fs pulses from an optical parametric oscillator at the center wavelength 1330 nm. With a coupled pulse energy of 2.17 nJ, the broadest spectrum in the fundamental TM mode extends from 936 nm to 1888 nm (162 THz) at -50 dB from peak. There is a good agreement between the measured spectrum and a simulation using a generalized nonlinear Schrödinger equation.

5.2 Introduction

A supercontinuum of light is generated when a narrow-band pulse undergoes an extreme spectral broadening due to nonlinear optical processes like self-phase modulation, cross-phase modulation, Raman scattering, soliton fission, dispersive wave generation, four-wave mixing and self-steepening[120]. Photonic crystal fiber has been remarkably successful in supercontinuum generation (SCG) due to the feasibility to control the dispersion and reduce the mode area by engineering its air-hole geometry[121–123]. Interest in SCG has been driven by applications including frequency combs[2, 71], optical coherence tomography[124] and wavelength division multiplexing[125, 126]. In the past few years, SCG has also been investigated in several chip-based systems including silicon photonic nanowires[127–129], chalcogenide waveguides[130, 131] and silicon nitride (Si_3N_4) waveguides[132, 133]. These chip-based waveguides for SCG will become important elements to expanding the functionality of photonic integrated circuits.

5.3 Experimental demonstration of supercontinuum generation

In this work, we demonstrate SCG using an on-chip silica (SiO_2) waveguide. Silica has a relatively small Kerr coefficient n_2 of $2.6 \times 10^{-20} \text{ m}^2\text{W}^{-1}$ [134], which is 10

times smaller than silicon nitride and more than 100 times smaller than silicon[62]. Compared to other materials, however, silica has a much lower linear loss, a feature central to the success of optical fiber based SCG devices. Recently, a chip-based, silica waveguide having record-low optical loss was demonstrated[29]. In addition to its function as an optical delay line, here the possibility of SCG in the waveguide harnessing its nonlinear interaction length is tested.

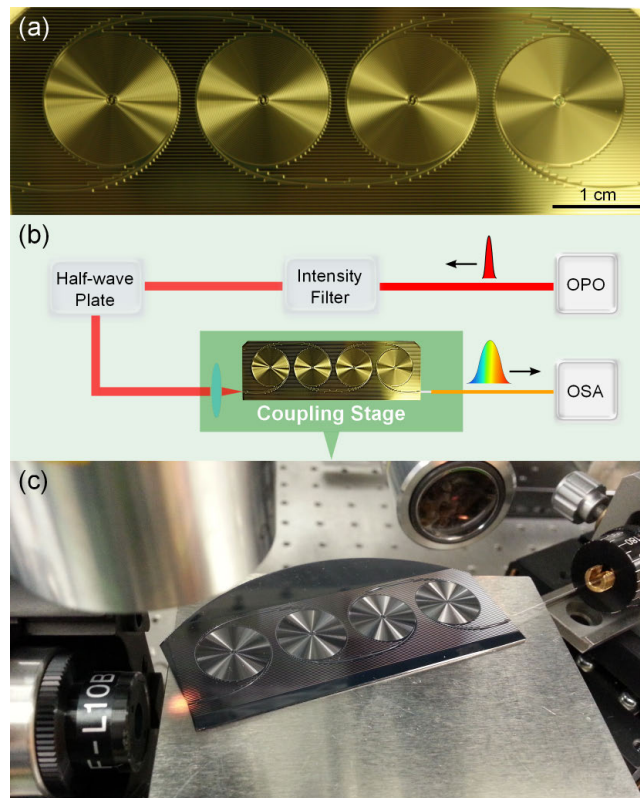


Figure 5.1: **Low-loss, silica-on-silicon waveguide and experimental setup.** (a) Photograph of the sample showing four, cascaded spiral waveguides. (b) Experimental setup for supercontinuum generation and characterization using the silica waveguide. OPO: optical parametric oscillator; OSA: optical spectrum analyzer. (c) Close-up view of the optical coupling stage, imaging objectives and spiral waveguide chip.

The silica waveguide used in the experiment has a total physical path length of 3.5 m and consists of four, cascaded sections (see Figure 5.1a). Each section contains two, interleaved waveguides configured in the form of an Archimedean spiral. For example, a lightwave traveling from left-to-right would enter the far-left spiral of Figure 5.1a at the bottom, take a counter-clockwise path towards the spiral center, execute a turn on an S-shaped waveguide at the spiral center and then exit on a

clockwise path. A connection waveguide then conveys the lightwave to the next spiral where entry now occurs on a clockwise path. Each spiral has an outer radius of 7.0 mm. The chip size is 2.5 cm \times 6.9 cm. The details of the fabrication method and waveguide design principles can be found in[29, 135].

To test spectral broadening using the spiral waveguide, an optical parametric oscillator (Spectra-Physics OPAL) is used to generate an 80 MHz-repetition rate and 180 fs-long (FWHM) pulse. The peak power of the pulse is controlled by a variable neutral density filter and the polarization by a half-wave plate as shown in Figure 5.1b. Both TE and TM mode SCG were studied and exhibited qualitatively similar behavior both in the measurements and modeling. However, only data for the TM modes are presented as their spectra are slightly broader on account of a reduced modal, cross-sectional area relative to the TE modes. An objective lens with 12 mm-focal length is mounted on a piezo-controlled xyz -stage for the coupling of OPO pulses into the waveguide. Due to the cleave angle of the front facet of the waveguide (introduced to minimize back reflection), the sample is rotated by 35-40° for efficient coupling. At the end facet, a cleaved multimode fiber is closely positioned to receive the light coming out of the waveguide. The coupling loss at the input and the output end of the waveguide is estimated to be around 3 dB and 10 dB, respectively. The other end of the multimode fiber is connected to an OSA. Two OSAs were used to separately record the spectra in the wavelength range 600-1700 nm (Agilent 86141B) and 1200-2400 nm (Yokogawa AQ6375). As the center wavelength of the input pulse is varied from 1250 nm to 1350 nm, the broadest spectrum is observed near 1330 nm. Measured TM mode spectra for various coupled pulse energies are presented in Figure 5.2. At the maximum energy of 2.17 nJ, an octave spanning continuum extending from 936 nm to 1888 nm (162 THz) at -50 dB from peak is generated.

5.4 Modeling ultra-low-loss silica spiral waveguides

The pulse propagation in the waveguide is modeled by implementing a generalized nonlinear Schrödinger equation[136].

$$\frac{\partial \tilde{A}'}{\partial z} = i\gamma(z, \omega)e^{-\mathcal{L}(z, \omega)z} \times \mathcal{F}\left\{A(z, T) \int_{-\infty}^{\infty} R(T')|A(z, T - T')|^2 dT'\right\} \quad (5.1)$$

$A(z, T)$ is the pulse envelope in a frame of reference moving along the z -direction at the group velocity at the pump frequency ω_0 ; $\tilde{A}(z, \omega - \omega_0)$ is its Fourier transform(\mathcal{F}),

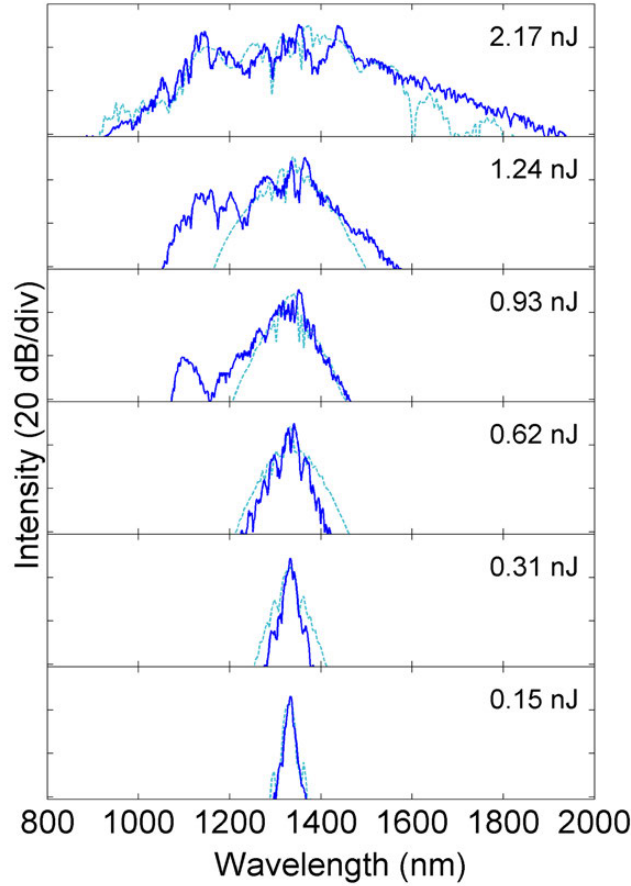


Figure 5.2: **Spectral broadening in the fundamental TM mode measured at a series of pulse energies.** The blue curves are measured spectra, and the dashed curves in light blue are spectra from the simulation.

and $\tilde{A}'(z, \omega - \omega_0)$ is defined as $\tilde{A}(z, \omega - \omega_0)e^{-\mathcal{L}(z, \omega)z}$. The function $\mathcal{L}(z, \omega) = \sum_{k=2}^M \frac{\beta_k(z, \omega_0)}{k!} (\omega - \omega_0)^k - \frac{\alpha(z, \omega)}{2}$ has contributions from the dispersion (first term) and the optical loss (second term), where β is the propagation constant and $\beta_k = \frac{\partial^k \beta}{\partial \omega^k}$. Once $\beta_2(z, \omega)$ is known, then $\beta_k(z, \omega_0)$ for $k \geq 3$ can be obtained by fitting $\beta_2(z, \omega)$ to a polynomial in $\Delta\omega = \omega - \omega_0$. In the simulation, the fitting is taken to 13-th order in the summation. Lastly, $\gamma(z, \omega)$ is the frequency-dependent nonlinearity and $R(T)$ is the nonlinear response function which has an instantaneous electronic contribution and a contribution from the delayed Raman response[137].

The dispersion, nonlinearity, and scattering loss of the waveguide as a function of waveguide radius in the spiral are calculated using a finite element solver. In Figure 5.3, the group velocity dispersion ($-\frac{2\pi c}{\lambda^2} \beta_2$) and nonlinearity at selected values of waveguide radius r are shown. The outermost part (at $r = 7.0$ mm) of

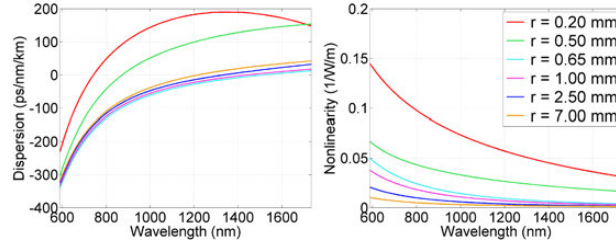


Figure 5.3: **Calculated dispersion and nonlinearity of the fundamental TM mode at a series of bending radii that occur at the inner and outer waveguides within each spiral.**

a spiral waveguide has a $8 \mu\text{m}$ -thick, 30° wedge-shaped cross section. It has a zero-dispersion wavelength of 1230 nm and a nonlinearity of $0.001\text{-}0.010 \text{ W}^{-1}\text{m}^{-1}$ over the wavelength range $600\text{-}1700 \text{ nm}$. As the waveguide spirals inside, the zero-dispersion wavelength increases up to 1510 nm because of the more negative geometric dispersion of the waveguide at smaller radius. Proceeding further inside ($r < 0.7 \text{ mm}$), the wave experiences a drop of the zero-dispersion wavelength due to a tapering of the waveguide for the minimization of the transition loss over the S-shaped waveguide at the spiral center. At $r = 0.2 \text{ mm}$ where the wave enters the S-shaped waveguide that couples light between clockwise and counterclockwise spirals, the waveguide has a triangular cross section with $1.4 \mu\text{m}$ -thickness. There, the zero-dispersion wavelength is as short as 720 nm and nonlinearity is as high as $0.0313\text{-}0.145 \text{ W}^{-1}\text{m}^{-1}$ over the wavelength range $600\text{-}1700 \text{ nm}$. Since the length of the tapered section is negligible, however, most of the spectral broadening occurs in the non-tapered outer region of the spiral.

On account of the radial dependences in Figure 5.3, there is a corresponding z -dependence for quantities within Eq. (1) which is accounted for as follows. The equation for an Archimedean spiral is $r = b\theta + r_c$ in polar coordinates where r is the bending radius, θ is the rotational angle, and the origin is taken to be the spiral center. The parameter $b = 0.056 \text{ mm}$ is the distance between successive turnings divided by 2π , and $r_c = 0.2 \text{ mm}$ is the radius at which the spiral ends and the S-shaped waveguide starts near the center. Defining $r_0 = 7.0 \text{ mm}$ as the radius at the waveguide entrance ($z = 0$), the radius of the waveguide at the inward propagation length z is $r(z) = \sqrt{r_0^2 - bz}$. Outward propagation is modeled in a similar way. Quantities in Eq.(1) are then evaluated at twenty-two chosen values of radii directly from FEM simulations and interpolated at all the other radii encountered in the waveguide. The resulting spectra from a simulation match well with the measured

ones (See Figure 5.3).

In conclusion, we have experimentally demonstrated a supercontinuum using an on-chip silica waveguide pumped by femtosecond pulses from an OPO. An octave spanning spectrum in the telecommunication band is generated in the fundamental TM mode. The modeling of the pulse propagation in the spiral waveguide is discussed and a good agreement between the measured spectrum and a simulation is found. With further dispersion engineering and tighter modal confinement, a silica waveguide is expected to be a viable platform for nonlinear optics on a chip.

DISPERSION-ENGINEERED PHOTONIC WAVEGUIDES FOR SUPERCONTINUUM GENERATION

- [1] **D. Y. Oh***, K. Y. Yang*, C. Fredrick*, G. Ycas, S. A. Diddams, and K. J. Vahala. “Coherent ultra-violet to near-infrared generation in silica ridge waveguides”. In: *Nature Communications* 8 (2017), p. 13922. doi: 10.1038/ncomms13922.

6.1 Abstract

Short duration, intense pulses of light can experience dramatic spectral broadening when propagating through lengths of optical fiber. This continuum generation process is caused by a combination of nonlinear optical effects including the formation of dispersive waves. Optical analogues of Cherenkov radiation, these waves allow a pulse to radiate power into a distant spectral region. In this work, efficient and coherent dispersive wave generation of visible to ultraviolet light is demonstrated in silica waveguide arrays on a silicon chip. Unlike fiber broadeners, the arrays provide a wide range of emission wavelength choices on a single, compact chip. This new capability is used to simplify offset frequency measurements of a mode-locked frequency comb. The arrays can also enable mode-locked lasers to attain unprecedented tunable spectral reach for spectroscopy, bioimaging, tomography and metrology.

6.2 Introduction

Continuum generation in microstructured optical fiber[122] gained importance with the generation of broad spectra[121] for application in optical frequency combs. There, a mode-locked laser is broadened as a precursor to f - $2f$ measurement of the comb offset frequency[2] and self-referencing[71]. The advent of frequency microcombs[8] and most recently the demonstration of femtosecond pulse generation in microcavities[27, 28, 58, 138] has focused attention on techniques for supercontinuum generation on a chip. Beginning with studies of Raman and four-wave-mixing effects in monolithic waveguides[139], there has been steady progress towards supercontinuum generation using a variety of on-chip waveguide materials[127, 130, 140–144]. An overview of waveguide materials used for supercontinuum generation

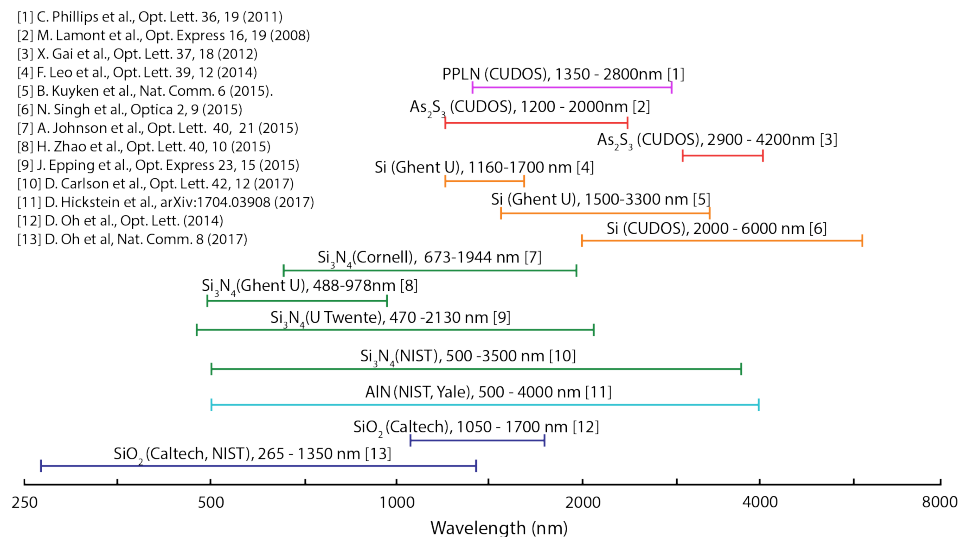


Figure 6.1: Overview of on-chip waveguide platforms for supercontinuum generation. The spectral extents of supercontinua of light generated in various waveguide platforms are shown. It does not include all the supercontinuum waveguides reported in the literature as the body of the work in the field continues to grow.

is provided in Figure 6.1. Low pulse energies for efficient broadening have been demonstrated on account of large nonlinear coefficients combined with nano-scale waveguide cross sections[141, 142, 145, 146], and devices operating in the mid-infrared[147, 148] are possible. Moreover, self-referencing has been achieved using a silicon nitride based, monolithic waveguide on silicon[149, 150].

However, while there has been remarkable progress on visible[151, 152] and ultra-violet (UV) band[153–155] continuum generation in microstructured optical fibers, as well as harmonic UV and deep UV generation in gas-filled fibers[156, 157], there have been no reports of chip-based UV generation. Furthermore, widely tunable emission in a single device is a feature of monolithic arrays that has no parallel in optical fibers. Arrays enable precisely targeted wavelength emission for optimal self-referencing. As shown here, their compactness also eliminates the need for delay lines in these systems. Finally, this class of devices can be combined with microcombs and compact mode-locked lasers to provide user-designed coherent, short pulse light for optical clocks[158], laser cooling[159], quantum manipulation of atoms and ions[160] and bioimaging[161].

After describing the silicon ridge waveguide array fabrication process, measurements of dispersive-wave generation are presented that include a study of the phase

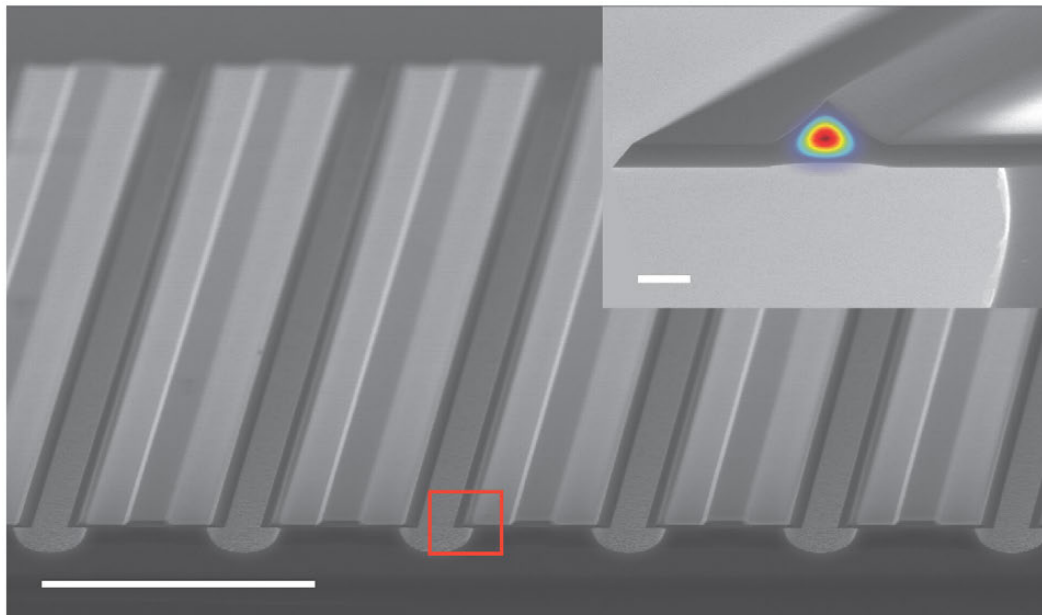


Figure 6.2: **Silica ridge waveguide structure.** Scanning electron microscope images of an array of silica ridge waveguides on a silicon chip. Silicon pillars support silica layers containing waveguides. The red box in panel (a) contains a silica waveguide whose cross section is shown as the inset. The cross section shows the calculated mode profile of the TM mode at wavelength 830 nm superimposed. Scale bar is 100 μm for (a) and 1 μm for the inset.

matching wavelength dependence upon the waveguide geometry. Application of the waveguide array to optimized self-referencing of a mode-locked Yb fiber laser is then presented. Here, the dispersive wave phase matching wavelength is precisely matched to the $2f$ frequency so as to provide maximum signal-to-noise in the frequency-comb offset-frequency measurement. Also, the approach eliminates the delay line used in the standard self-referencing method. Finally, the continuum spectra produced by the waveguide arrays are analyzed and modeled in detail.

Continuum generation in waveguides results from a combination of nonlinear processes[123, 139]. Self-phase modulation in combination with second-order anomalous dispersion induces temporal compression of an input pulse. As the pulse spectrally broadens, higher-order dispersion and Raman interactions become important and the pulse undergoes soliton fission. The resulting series of fundamental solitons experiences Raman self-frequency shifting towards longer wavelengths. If the soliton spectrum has significant overlap with spectral regions that feature normal dispersion, then it can radiate energy into a dispersive wave that phase matches to the soliton phase[162]. The dispersive wave, which can also be understood in

terms of an analogy to Cherenkov radiation[163], provides a powerful way to both engineer the spectral extent of the resulting optical continuum and to also spectrally concentrate optical power in new bands[152, 164]. The waveguides demonstrated here apply lithographic control to engineer the generation of coherent UV to visible dispersive-wave radiation.

6.3 Silica ridge waveguide array

Fabrication process

The waveguide geometry is shown in Figure 6.2 and features a silica ridge design that is air-clad on three sides. The air-cladding enables a high level of optical confinement to both increase the optical nonlinearity and shift the wavelength for zero group velocity dispersion towards visible wavelengths. The fabrication of the waveguides is similar to the process used for the integrated ultrahigh- Q silica ridge ring resonator (see Chapter 2). The process flow is presented in Figure 6.3. Waveguide arrays are fabricated on (100) prime-grade float-zone silicon wafers. The initial oxide layer is thermally grown at 1000 °C with 2 μm thickness. The photoresist is patterned on the oxide layer (Figure 6.3a), and acts as etch mask during hydrofluoric acid (HF) immersion. HF wet-etching creates the wedge surfaces at the edge of the photoresist pattern, and the further wet-etching results in the triangular-cross-section ridge stripe of silica as the two angled wedge surfaces meet each other (Figure 6.3b). The wet-etching duration is around 45 min. Then, an additional thermal oxidation creates an under-layer of silica (Figure 6.3c). The waveguide chips used for data in this chapter had the under-layer thickness of either 310 nm or 450 nm. Striped openings (Figure 6.3d) are etched after a second lithography step (Figure 6.3e). As a final step, the silicon under the oxide structure is isotropically etched (Figure 6.3f). Both numerical calculation and measurement confirmed that an undercut of 10 μm is sufficient to eliminate the silicon structure interaction as a result of modal confinement. The average spacing between two waveguides is about 35 μm , and 725 waveguides per inch can be fabricated in an array.

The ability to lithographically define ridge dimension enables precise control of waveguide dispersion, and, in turn, precise tuning of the dispersive wave wavelength. Figure 6.4 shows the dependence of the ridge dimension parameters(H,w) on the mask width. Here, the mask width is the width of the red rectangular strip patterned on photoresist in Figure 6.3a. The ridge height (H) and width (w) increase by about 0.5 μm and 1 μm , respectively, as the mask width increases by 1 μm .

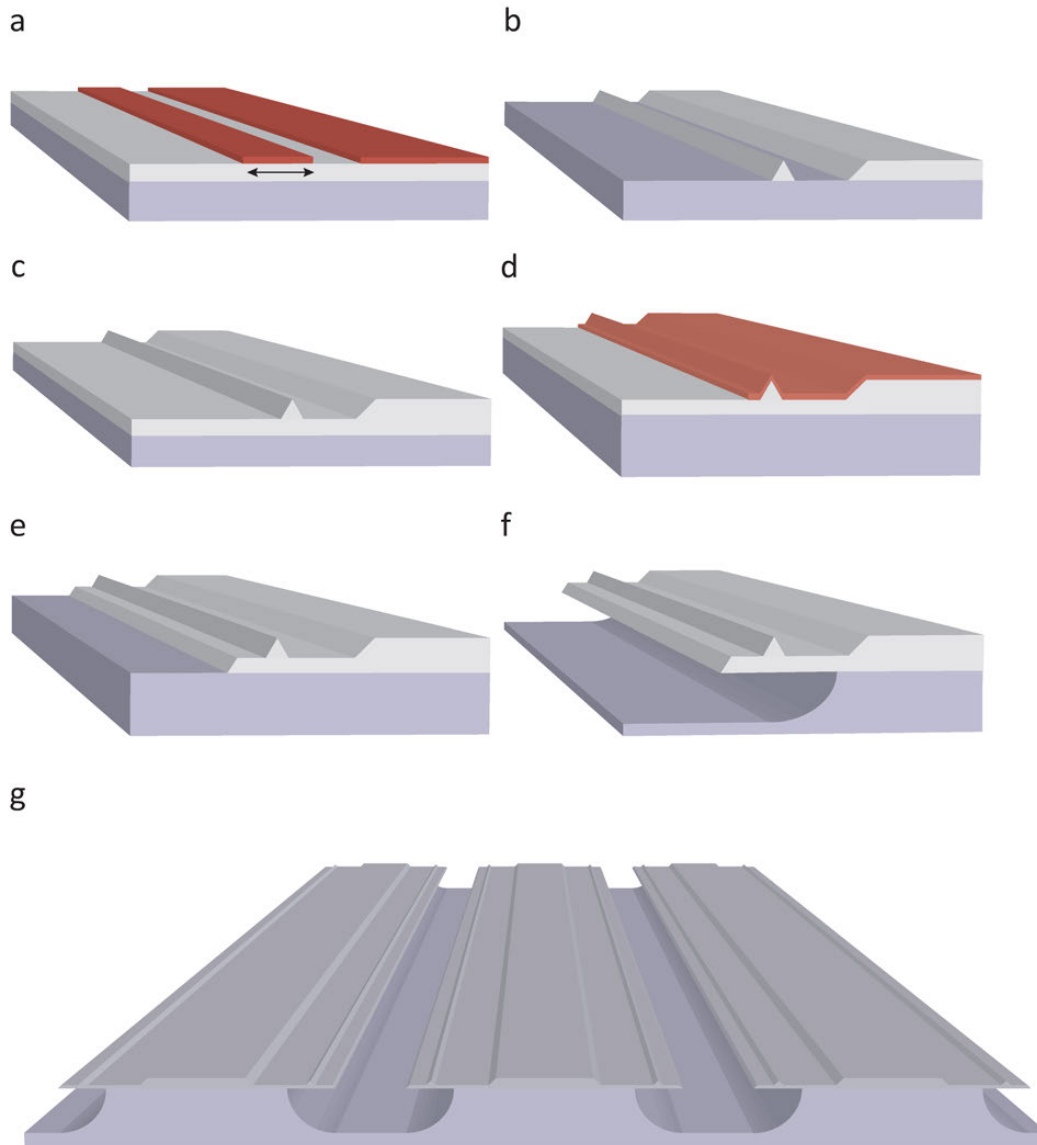


Figure 6.3: **Ridge waveguide array microfabrication process.** (a) Photolithography on thermal silica layer. Mask width is denoted by the double-arrow line. (b) HF wet-etching to define silica ridge. (c) Additional oxide layer is grown by thermal oxidation. (d) Supporting structure is patterned by photolithography. (e) HF wet-etching creates striped openings in the silica layer. (f) Isotropic etching of the silicon (XeF_2) is performed to undercut the silica layer. (g) Rendering of final ridge waveguide array structure. Dependence of ridge dimension on mask width is shown in Figure 6.4.

Dispersion-engineering

The waveguides support both transverse electric (TE) and transverse magnetic (TM) polarizations. They are also multimode waveguides. However, pulses of Gaussian

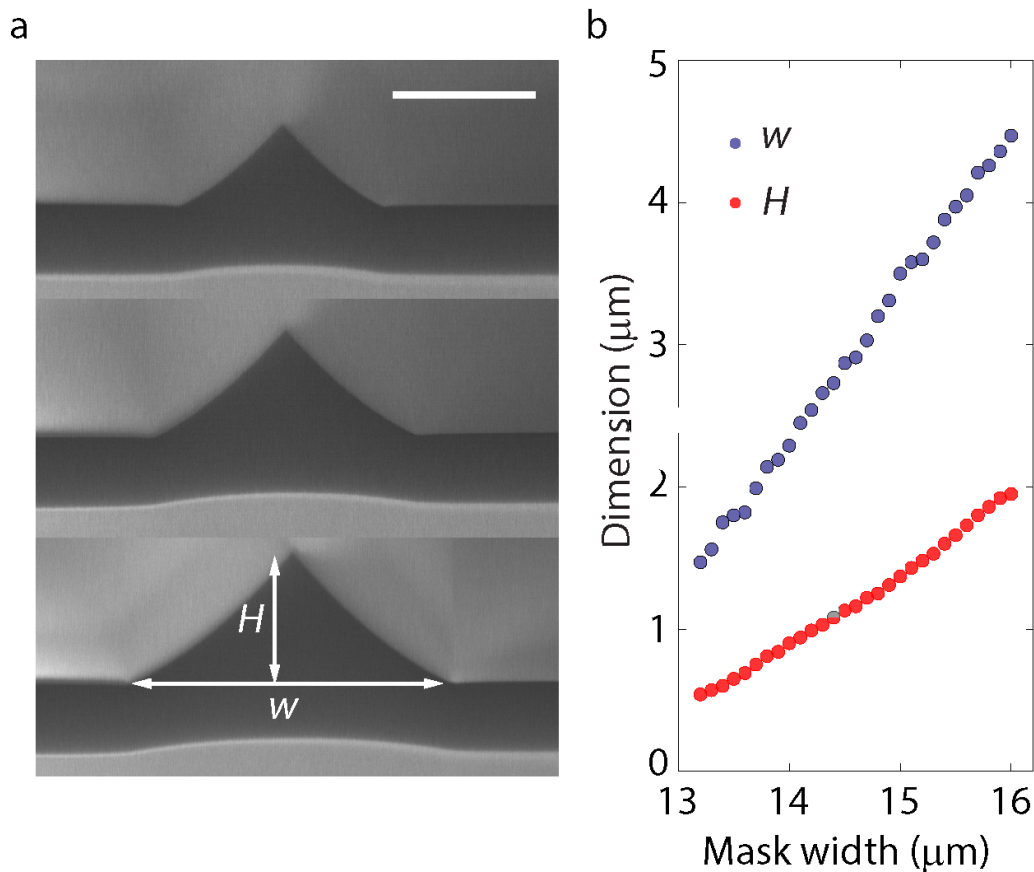


Figure 6.4: **Dependence of ridge dimension on mask width** (a) SEM images of a series of ridges in a fabricated silica waveguide array. The thickness of the base silica layer is $0.45 \mu\text{m}$. Scale bar is $1 \mu\text{m}$. The definition of ridge height(H) and ridge width(w) is shown in the panel. (b) Measured ridge dimensions based on SEM images as a function of mask width

beam profiles couple most efficiently to the fundamental mode families and the effect of higher order modes in the waveguides was negligible in the results presented in this chapter. Therefore, we limit our discussion to the fundamental mode families supported by the silica ridge waveguides. We also find that the electric field intensity of the TM mode family at the surface of the ridge is greater than that of the TE mode family, and therefore the TM mode experiences stronger anomalous dispersion contributed from the waveguide geometry. As a result, the TM mode provides dispersive wave generation at shorter wavelengths. To describe the dispersion engineering in this section and the scheme of dispersive wave phase-matching condition in Section 6.4, we present the numerical simulation results of the TM mode family. However, the same design principles can be used for dispersive wave

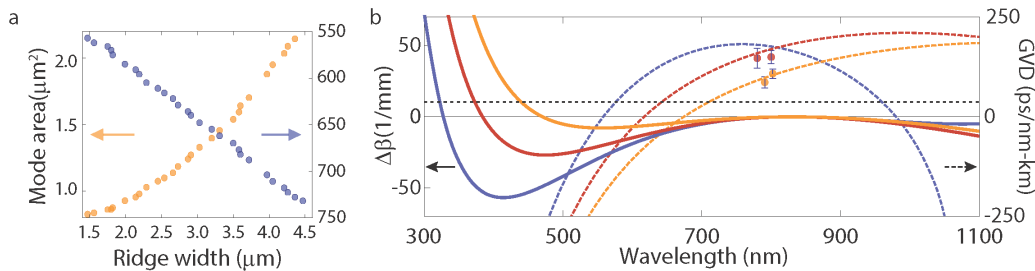


Figure 6.5: Dispersion engineering of ridge waveguides. (a) Calculated mode area and zero dispersion wavelength (λ_{ZDW}) are plotted versus the ridge base width. (b) Calculated mode area and zero dispersion wavelength (λ_{ZDW}) are plotted versus the ridge base width. Calculated group velocity dispersion (GVD, dashed lines) and phase-matching parameter $\Delta\beta$ (solid lines) for dispersive wave generation in TM polarization are plotted versus wavelength. Blue, red and yellow solid and dashed lines correspond to mode areas of 0.83 μm^2 , 1.03 μm^2 , 1.69 μm^2 respectively. The phase matching condition $\Delta\beta = \frac{1}{2}\gamma P_p$ (830 nm pump) is satisfied at the intersections of the colored solid lines and the black dashed line. The points with error bars are measured dispersion values obtained from sets of ten scans of spectral fringes measured using a Mach-Zehnder interferometer (see the text).

generation using the TE mode.

Waveguide arrays of varying mode area (0.76 μm^2 to 2.22 μm^2) were fabricated on the silicon chip. The effective mode areas are determined by input of waveguide cross sections (measured in a scanning electron microscope, SEM) into a finite-element-method (FEM) solver. The wavelength dependence of the second-order dispersion is also calculated using the FEM solver. The Sellmeier equation was used to include the wavelength dependence of the silica refractive index[113]. While bulk silica features anomalous dispersion only for wavelengths beyond 1270 nm, the geometrical dispersion introduced by the strong optical confinement of the ridge waveguide enables anomalous dispersion at much shorter wavelengths. In particular, the zero crossing of the dispersion (λ_{ZDW}) can be engineered to occur over a wide range of wavelengths from 557 nm to 731 nm as is apparent in Figure 6.5. Importantly, these lie well below the pumping wavelengths of 830 nm and 1064 nm that we employ.

To verify that the waveguide exhibits anomalous dispersion near the value predicted by the FEM simulations, the group velocity dispersion is characterized using a Mach-Zehnder interferometer having one arm with an adjustable delay[165]. In the dispersion measurement, a probe pulse is attenuated to a low enough pulse

energy (< 30 pJ) so as to prevent significant nonlinear phase shifts in the waveguide. The pulse is split using a beamsplitter and propagates into two arms of a Mach-Zehnder interferometer. One pulse is coupled to the waveguide and the other one propagates through the adjustable delay line in the air. The light emitted from the waveguide is collimated and the pulses from the two arms are combined using a second beamsplitter. The combined beams are then focused into a single mode fiber and sent to a spectrometer. The time delay between the two pulses is calculated using the Fourier-transform of the measured spectrum which shows spectral fringes[166]. By tuning the laser wavelength from 770 nm to 810 nm, the dispersion of the waveguide is then measured from the observed wavelength-dependence of the group delay in the waveguide arm. The measured dispersion is plotted in Figure 6.5b and agrees well with the FEM simulation. The error bars in Figure 6.5b are derived from the standard deviation of group delay from 10 spectral measurement at each wavelength.

6.4 Dispersive wave generation

Phase matching condition for the dispersive wave generation

The phase matching condition for the dispersive wave generation satisfies the following equation[167]:

$$\beta(\omega_{\text{DW}}) - \beta(\omega_{\text{p}}) - \frac{1}{v_{\text{g}}} \times (\omega_{\text{DW}} - \omega_{\text{p}}) - \frac{1}{2} \gamma P_{\text{p}} = 0 \quad (6.1)$$

where $\beta(\omega_{\text{DW}})$ and $\beta(\omega_{\text{p}})$ are the propagation constants at the dispersive wave frequency (ω_{DW}) and the pump frequency (ω_{p}), respectively, and v_{g} is the group velocity at the pump frequency. P_{p} is the peak power of the pulse when the dispersive wave is generated. γ is the nonlinearity of the waveguide at the pump frequency and is given by $\gamma = \omega_{\text{p}} n_2 / (c A_{\text{eff}})$ where n_2 is the Kerr coefficient and A_{eff} is the effective mode area. Defining $\Delta\beta(\omega) = \beta(\omega) - \beta(\omega_{\text{p}}) - (\omega - \omega_{\text{p}})/v_{\text{g}}$, the dispersive wave phase matching condition is given by $\Delta\beta(\omega_{\text{DW}}) = \gamma P_{\text{p}}/2$ and is plotted in Figure 6.5b for an 830 nm pump. At this pump wavelength, the phase matching wavelength can be engineered to vary from 310 nm to 576 nm.

The colormap in Figure 6.6 illustrates the TM-polarized dispersive wave wavelength (λ_{DW}) as a function of pump wavelength and ridge width in the waveguide array of Figure 6.5a. The black lines in the figure give the zero crossing of the group velocity dispersion ($\lambda_{\text{ZDW},1}$ and $\lambda_{\text{ZDW},2}$) as a function of the ridge width. For waveguides with $w < 2.19 \mu\text{m}$, there is a second zero crossing ($\lambda_{\text{ZDW},2}$), allowing for formation

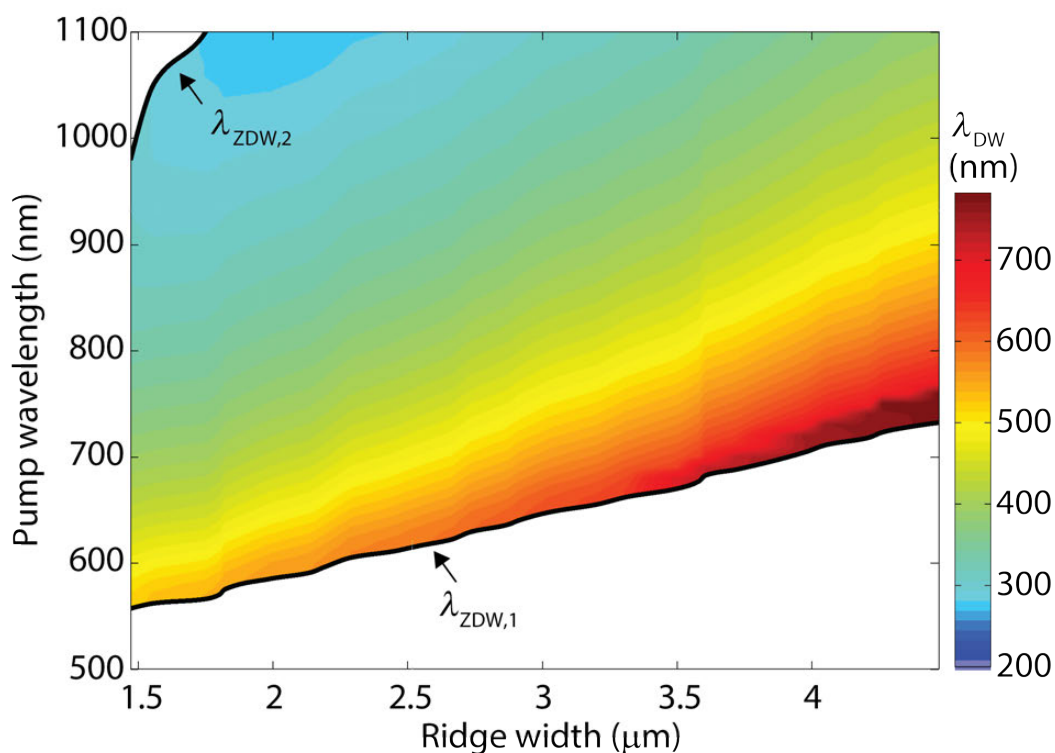


Figure 6.6: **Phase-matching dispersive wave wavelength in a waveguide array.** Calculated TM dispersive wave wavelength (λ_{DW}) as a function of pump wavelength and ridge width is plotted as a colormap for the waveguide array chip used in Figure 6.8e. The black lines are the zero crossing of the group velocity dispersion ($\lambda_{ZDW,1}$ and $\lambda_{ZDW,2}$). The white area is where dispersive waves do not exist.

of a second dispersive wave. However, a second dispersive wave was not observed in our experiment due to the loss of modal confinement at long wavelengths for the waveguides with small cross section.

An upper bound on λ_{DW} for a given ridge width is provided by $\lambda_{ZDW,1}$. λ_{DW} will approach this wavelength as the pump wavelength approaches $\lambda_{ZDW,1}$. On the other hand, a lower bound on λ_{DW} is determined by the longest pump wavelength possible in the anomalous dispersion regime (colorized region). Color shading is used in Figure 6.6 to indicate the dispersive wave wavelengths that are possible. λ_{DW} shifts toward shorter wavelength as the pump wavelength increases. This is understood from the phase-matching condition. At longer pump wavelengths, the group velocity is smaller, and hence the propagation constant of the dispersive wave must be larger (shorter wavelength) for the phase-matching to occur. The upper bound on the

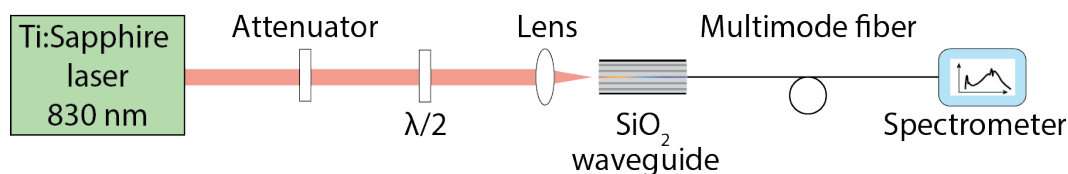


Figure 6.7: **Experimental setup for supercontinuum generation using a titanium sapphire laser centered at 830 nm.** The pulses entering the ridge waveguides have FWHM temporal width of 60 fs.

pump wavelength in the anomalous dispersion regime is given by $\lambda_{ZDW,2}$ if it exists. The calculation is consistent with our demonstration of dispersive wave generation at wavelength $\lambda_{DW} < 300$ nm using a 1064 nm pump wavelength as compared to the shortest λ_{DW} of 310 nm generated using an 830 nm pump wavelength. Lastly, smaller mode area results in smaller λ_{DW} and can be achieved with smaller ridge width. However, there is a threshold value of ridge width below which the mode area increases because of weak modal confinement. For the array waveguide chip with lower silica layer thickness $0.45 \mu\text{m}$, the threshold ridge width is $1.47 \mu\text{m}$ using 830 nm pump.

Imaging dispersive waves in the array.

To demonstrate the controlled UV-visible light emission using the array, a pulse from a mode-locked titanium-sapphire laser (830 nm emission, 60 fs pulse width measured on an autocorrelator, and 81 MHz repetition frequency) is coupled into the silica ridge waveguides using a $60\times$ objective lens as shown in Figure 6.7. The coupling efficiency is measured to be 25-35%. Photographs of pumped waveguides on a single chip are combined in Figure 6.8. As the laser pulse propagates along a given waveguide (left-to-right in the image), the infrared pulse is initially invisible. The pulse undergoes temporal compression and spectral broadening due to the self phase modulation and anomalous second-order dispersion. As broadening occurs, portions of the pulse's spectrum become visible. Soliton fission and dispersive wave generation occur at the bright orange spot. Waveguide areas are larger for upper waveguides in the photograph and decrease towards the lower portion of the plot. Decreasing mode areas shift the phase matching condition to shorter wavelengths so that the dispersive wave generation transitions from the visible to ultraviolet. For wavelengths below 400 nm the dispersive wave is not visible in the photograph.

More details about the pulse propagation in the waveguide are provided in Figure 6.9. Here, calculated spectra are plotted versus propagation length for pulse energies

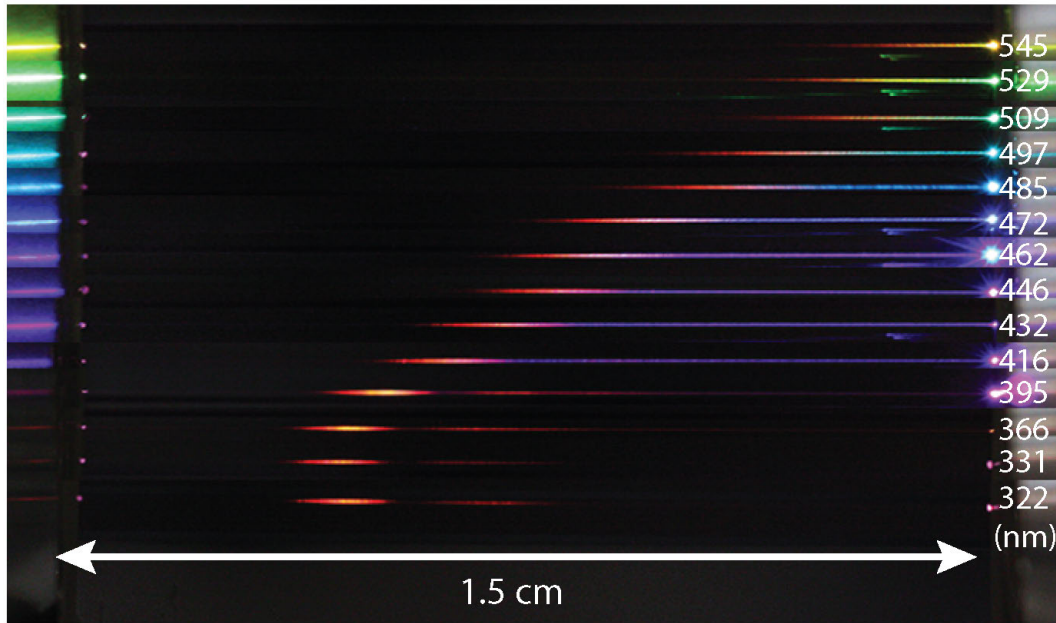


Figure 6.8: **Direct observation of dispersive wave generation** UV-visible dispersive wave generation in a silicon chip containing an array of waveguides with varying mode area (322 nm emission has area of $0.83 \mu\text{m}^2$ and 545 nm emission has area of $2.09 \mu\text{m}^2$) is directly observed. Image represents a photograph of scattered light taken from above the 1.5 cm long chip in which infrared pulses are launched at the left side of each waveguide. Pulse energies are set to the threshold pulse energy for dispersive wave generation. The color emission at the left side of the image is dispersive wave emission that has been reflected at the far right facet of the chip. The initial spectral broadening of the input pulse can be seen as the orange-red emission that gradually shifts diagonally upward right. The visible scattered light shown in the figure is a very small amount of the total generated. The vast majority of the light is forward propagating and collected into a multimode fiber (not shown).

of 330 pJ (Figure 6.9a) and 1100 pJ (Figure 6.9c). The pulse initially propagates as a higher-order soliton that undergoes temporal compression and spectral broadening until experiencing soliton fission and dispersive wave generation at a fission length, L_f , that depends upon the pulse energy (330 pJ: $L_f = 0.39$ cm; 1100 pJ: $L_f = 0.16$ cm). As the input pulse energy increases, the calculated fission length decreases. This behavior is observable in Figure 6.9b where a composite of photographs of the waveguide is shown at coupled pulse energies from 330 pJ to 1100 pJ. Soliton fission is observable as the reddish-orange emission. The observed soliton fission length agrees well with a numerical simulation shown as the grey line.

The dispersive wave initially overlaps with the soliton pulse but walks off from the soliton with continued propagation because of group velocity mismatch (see Figure

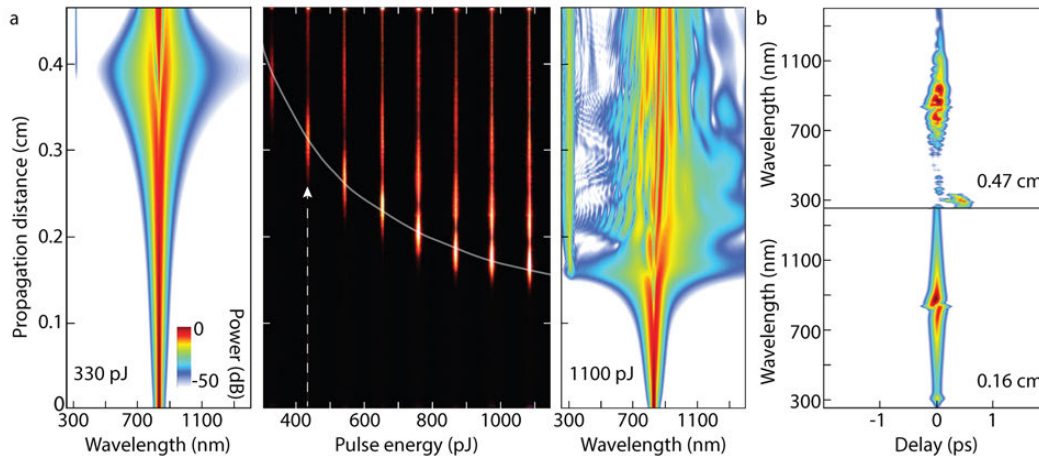


Figure 6.9: Numerical simulation of pulse propagation in the waveguide and comparison with measurement. (a) Calculated continuum spectra as a function of waveguide position at a coupled pulse energy of 330 pJ. The pulse is launched in the TM mode of the waveguide with mode area $0.76 \mu\text{m}^2$. The color bar (inset) applies to panels (a), (c), (d) and (e). (b) Top-view photographs of scattered light from the surface of the waveguide. The photographs were taken at pulse energies ranging from 330 pJ to 1100 pJ (left to right side). As indicated by the dashed line, the pulse travels in the waveguide from the bottom to the top of the image. Dispersive wave generation occurs in the UV and is therefore not visible in the image. The grey line superimposed on the photographs is the length at which dispersive wave generation occurs as predicted by the simulation. The spectral breathing of the input pulse results in a periodically visible orange-red emission that correlates with the calculation. (c) Calculated continuum spectra as a function of waveguide position at a pulse energy of 1100 pJ. (d-e) Calculated spectrograms of the optical pulse propagating in the waveguide corresponding to (c). The spectrogram in (d) is at waveguide position 0.16 cm where dispersive wave is generated. The spectrogram in (e) is at the waveguide output.

6.9d,e). Also, the dispersive wave is temporally stretched as it propagates in the waveguide due to the normal dispersion it experiences. Walk-off is a typical feature of fiber broadeners and requires a delay line to spatially overlap the octave wave (2f) and dispersive wave. However, as shown in the next section, the waveguide length can be adjusted to optimize overlap between 2f and dispersive-wave pulses. Moreover, the array itself provides the user with the ability to optimize the dispersive wave efficiency around a specific laser source.

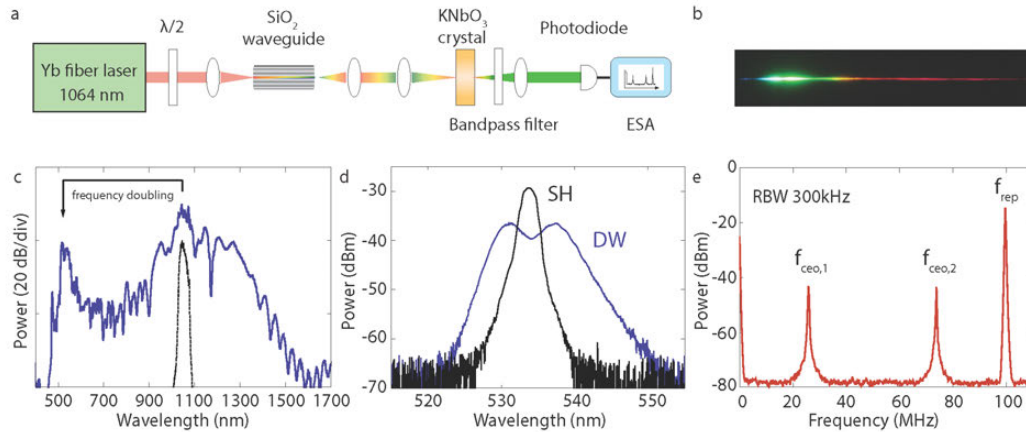


Figure 6.10: Application of dispersive wave engineering to self-referencing a Yb fiber laser frequency comb. (a) Experimental setup for measuring f_{ceo} of the Yb fiber laser. The ridge waveguide has a mode area $3.13 \mu\text{m}^2$ and length 1.50 cm. (b) Photograph of the emitted light dispersed through a prism and reflected on a white screen. Scale bar is 5 cm. (c) Measured optical spectrum of the collimated beam at the output facet of the waveguide. The coupled pulse energy is 2300 pJ and the input spectrum is shown in black. (d) Spectra of the dispersive wave (DW, blue) and second harmonic light (SH, black) filtered by a bandpass filter. (e) Radio-frequency spectrum measured with an electrical spectrum analyzer (ESA) shows the pulse repetition rate f_{rep} and the carrier-envelope-offset beat frequency $f_{\text{ceo},1}$ and $f_{\text{ceo},2}$. The resolution bandwidth (RBW) is 300 kHz.

6.5 Application: self-referencing of a frequency comb

Walk-off-free, dispersive-wave-enhanced octave generation for self-referencing of a Yb laser comb

Beyond the generation of broadly tunable visible light, precise dispersive-wave engineering in a monolithic waveguide can be applied both to enhance the signal-to-noise ratio as well as simplify the setup for detection of the carrier-envelope offset frequency of a laser frequency comb[2]. As a demonstration, f-2f offset frequency generation of a Yb fiber laser comb is performed using a silica ridge waveguide. The waveguide having a mode area of $3.13 \mu\text{m}^2$ and length of 1.50 cm is dispersion engineered so as to enhance dispersive wave formation at twice the frequency of the Yb laser comb. The experimental setup is shown in Figure 6.10a. The Yb laser emits 90 fs pulses with center wavelength of 1064 nm (100 MHz repetition rate). Prior to waveguide coupling, a halfwave plate rotates the Yb laser polarization so that 80% of the total coupled pulse energy (2300 pJ) is transmitted in the TE mode and 20% is transmitted in the TM mode of the waveguide.

The TE wave forms a dispersive wave near 532 nm. A photograph of the spectrum of the continuum is shown in Figure 6.10b and a spectral scan is provided in 6.10c. Both the TE and TM waves are subsequently coupled to a potassium niobate (KNbO₃) crystal where the TM component is phase matched for second harmonic generation. The phase-matching condition generates a second-harmonic beam that is rotated by 90 degrees relative to the TM fundamental so that the second-harmonic polarization is aligned with the TE polarized dispersive wave. The measured doubled spectrum and the dispersive-wave spectrum are shown in Figure 6.10d. After spectral filtering around 532 nm the two waves are mixed on a photodiode for offset frequency (f_{ceo}) beatnote generation. In this final step, the enhanced dispersive wave comb lines increase the beatnote strength. The electrical spectrum of the beatnotes at $f_{\text{ceo},1} = 25.8$ MHz and $f_{\text{ceo},2} = f_{\text{rep}} - f_{\text{ceo},1} = 73.8$ MHz are shown in Figure 6.10e. Both signals have a signal-to-noise ratio > 34 dB at an electrical resolution bandwidth of 300 kHz. This establishes the coherent nature of the dispersive wave and is more than sufficient for subsequent self-referenced servo control of the comb.

Beyond the enhanced signal-to-noise provided by the ability to select an optimal waveguide in the array for matching to the $2f$ frequency, there is a key simplification enabled by collinear generation of dispersive and second harmonic waves. The overall group velocity dispersion between the TE dispersive wave and the TM wave at 1064 nm in both the waveguide array and the KNbO₃ crystal is such that both the dispersive wave and the second-harmonic pulses emerge from the doubling crystal with a high degree of spatial overlap (i.e., walk-off-free). As a result, a major simplification is possible by eliminating the traditional step of path-length balancing using a Michelson interferometer. Instead, the two pulses (the dispersive wave and the second-harmonic pulse) can be directly coupled to the photodetector[168].

Temporal overlap between the dispersive and the second harmonic waves

The f - $2f$ offset frequency measurement in the collinear geometry could be done because the dispersive wave and the second harmonic temporally overlapped after the KNbO₃ crystal. Here, a calculation is provided that supports our experimental results. First, the group delay of a pulse after propagation in the TE mode and the TM mode of the waveguide is plotted in Figure 6.11. Defining $T_{\text{TE,wg}}^{1064}$ and $T_{\text{TM,wg}}^{1064}$ as the group delay for the TE and TM mode at pump wavelength 1064 nm, the relative delay between the two is $T_{\text{TM,wg}}^{1064} - T_{\text{TE,wg}}^{1064} = 0.18$ ps. Secondly, the group delay of the dispersive wave is calculated using the spectrogram in Figure 6.11. From the spectrogram, we estimate $T_{\text{TE,wg}}^{532} - T_{\text{TE,wg}}^{1064} = 0.5$ ps. Therefore, the temporal

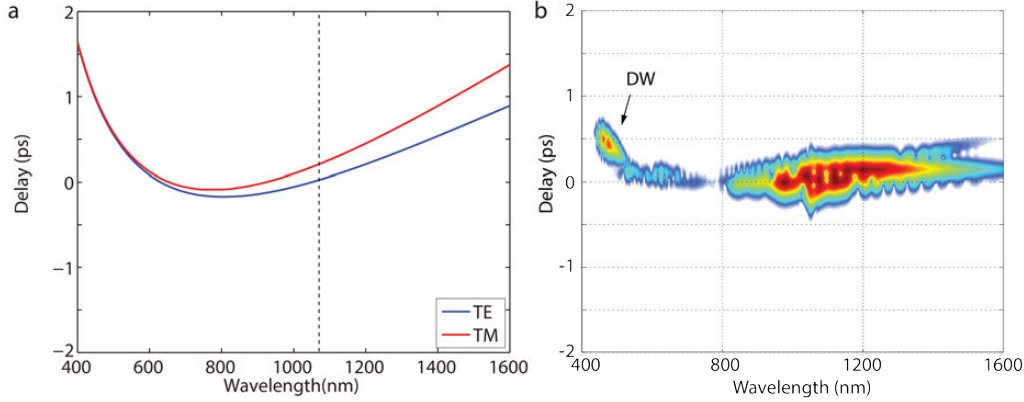


Figure 6.11: **Calculated temporal delay of the pulse used for f-2f measurement.** (a) Relative group delay between TE and TM mode at the end of the waveguide of length 1.5 cm. Delay is set to 0 for TE mode at the pump wavelength of 1064 nm. The dashed line is located at the pump wavelength of 1064 nm. (b) Spectrogram of the TE portion of the pulse at the end of the waveguide. As in panel (a), y-axis represents the relative group delay with respect to the group delay at the pump wavelength 1064 nm

delay between the TM fundamental and TE dispersive wave after the waveguide is $T_{TE,wg}^{532} - T_{TM,wg}^{1064} = 0.32$ ps.

Now we consider the temporal delay caused in KNbO_3 crystal, in which Type-I phase matching is used for efficient second harmonic generation[169]. The TM fundamental wave propagates along the b-axis of the crystal, and its second harmonic is generated and propagates in the c-axis. The TE dispersive wave also propagates in the c-axis. Based on the reported Sellmeier coefficients of KNbO_3 in literature[170], group index for b-axis and that for c-axis are calculated at 1064 nm and 532 nm, respectively: $n_{g,b}^{1064} = 2.3421$ and $n_{g,c}^{532} = 2.1788$. With these values, the relative delay between the fundamental TM wave and the TE dispersive wave caused by the crystal is given by $T_{TE,KNbO_3}^{532} - T_{TM,KNbO_3}^{1064} = -0.38[\text{ps/mm}] \times d$ where d is the distance that the pulse has propagated inside the crystal.

Propagation inside KNbO_3 crystal thus negates the relative delay caused by the waveguide. By adding the contribution by the waveguide and the crystal, we find the relative delay between the TE dispersive wave and the second harmonic of the TM wave to be $T_{TE}^{532} - T_{TM}^{1064} = T_{TE,wg}^{532} - T_{TM,wg}^{1064} + T_{TE,KNbO_3}^{532} - T_{TM,KNbO_3}^{1064} = 0.32 - 0.38[\text{ps/mm}] \times d$. Thus, the portion of the TM second harmonic generated

after the pulse propagates about 0.84 mm in the crystal overlaps temporally with the TE dispersive wave when they exit the crystal. The length of the KNbO_3 crystal used in the experiment is 2 mm but it is okay since the second harmonic of the TM fundamental travels at the same group velocity with the TE dispersive wave after its generation.

6.6 Spectral measurements

Precisely tuned dispersive wave emission in UV-visible bands

To further probe the behavior of the dispersive wave generation process, spectral measurements were performed at varying waveguide cross sectional areas. For these measurements, the titanium sapphire laser was used (see earlier discussion) and the experimental setup included an attenuator to vary the input pulse energy as well as a half-wave plate to control polarization. The light output from the waveguides is endfire-coupled to a multimode fiber for the measurement on a spectrometer. To cover the entire spectral range of interest two spectrometers were used: a Yokogawa (AQ6370D, 600-1700 nm) and an Ocean Optics (HR4000, 200-900 nm).

Measured supercontinuum spectra are shown in Figure 6.12 for TM and TE polarized pulses launched into waveguides of varying mode area in the waveguide array shown in Figure 6.8. Conversion of pump light in the near IR to visible and UV wavelength dispersive waves is apparent in each spectrum. A summary of measured dispersive wave emission wavelengths λ_{DW} versus mode area is provided in Figure 6.13. Controlled tuning of the dispersive wave from 310 nm to 576 nm with an average 8 nm interval is demonstrated in the TM mode and from 475 to 613 nm in the TE mode. Also included in Figure 6.13 is the predicted dispersive wave emission wavelength using the phase matching condition 6.1. The measurement result agrees well with the calculation.

To investigate the conversion efficiency of the input pulse from the near infrared into UV-visible wavelengths (300-650 nm), a UV fused silica aspheric lens (transmission 200-2000 nm) was used to collect the light exiting the waveguides. The optical power in the UV-visible wavelengths was then filtered out with a bandpass filter and measured by a thermopile power meter (nearly uniform spectral response). The power was calibrated using the wavelength-dependent transmission curves of the bandpass filter and the measured supercontinuum spectra. The scatter plot of measured conversion efficiency (and average dispersive wave power) plotted versus dispersive wave peak wavelength for both polarizations is shown in Figure

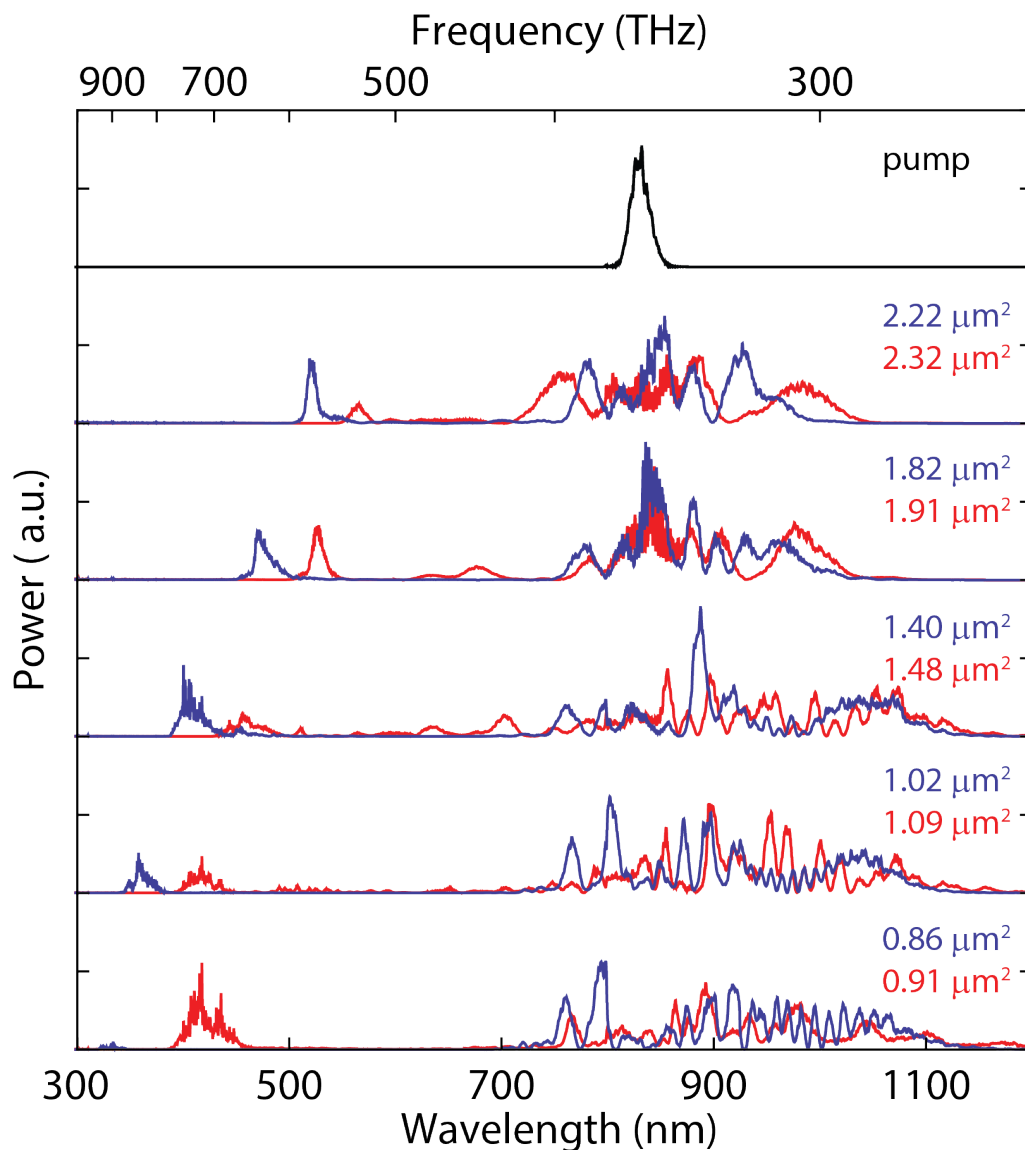


Figure 6.12: **Supercontinuum spectra generated in the TE and TM mode of the waveguides.** Supercontinuum spectra for a series of ridge waveguides on a single waveguide array chip shown in Figure 6.8 when the titanium sapphire laser pulse is coupled to the TM mode (blue line) and TE mode (red line) of the waveguides. The coupled pulse energy is 1000 pJ. The mode area of the waveguide is indicated in the panel. All the continuum spectra are normalized such that the areas under the spectra are the same.

6.13b. For this measurement, conversion efficiency is defined as the dispersive wave power at the waveguide output divided by the total collected spectral power at the waveguide output. The spectral extent of the dispersive wave was defined by selecting wavelengths where the power spectral density of the dispersive wave had

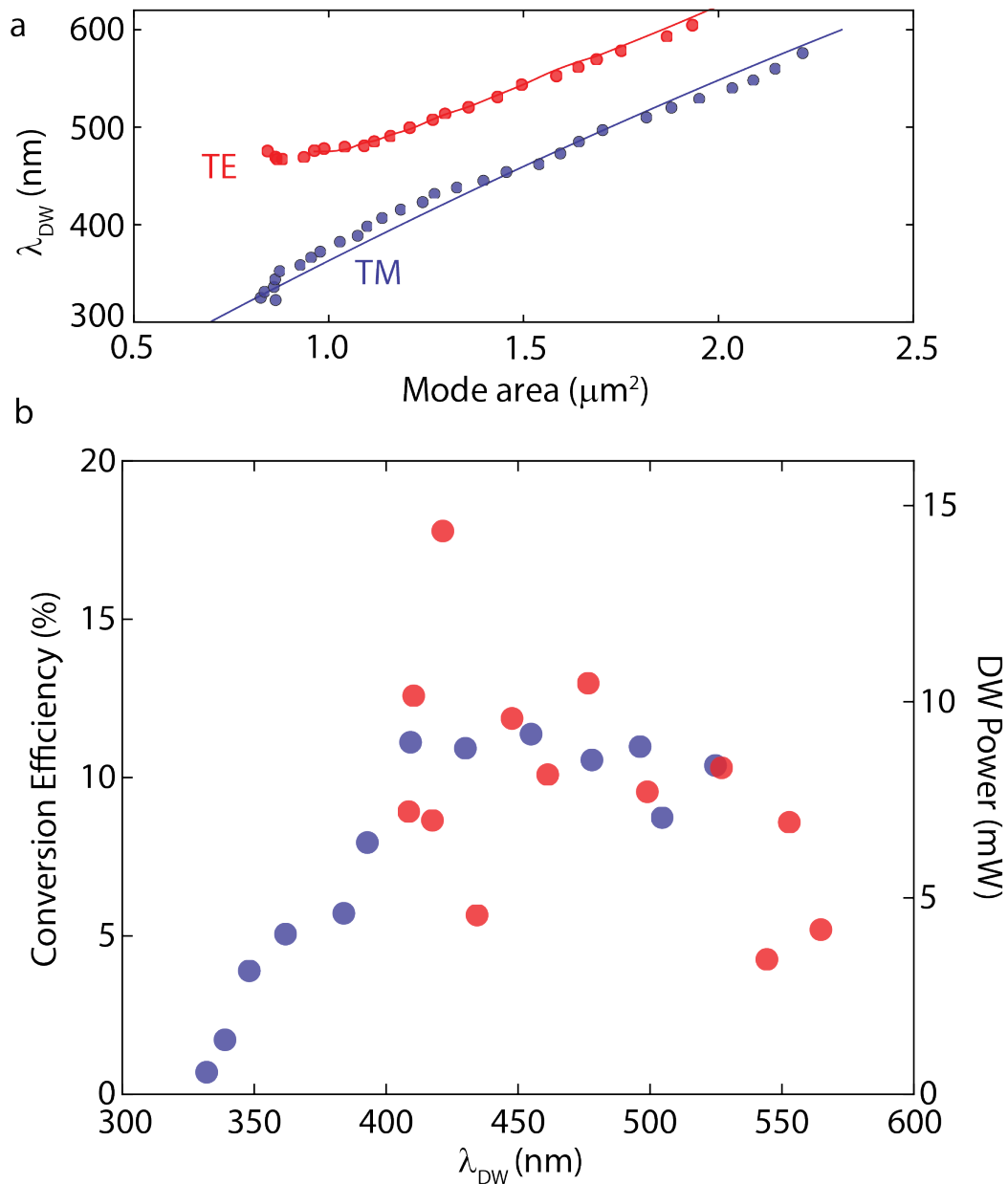


Figure 6.13: **Precisely tuned and efficient emission of dispersive waves in the UV-visible wavelengths.** (a) Measured tuning of the dispersive wave peak wavelength (λ_{DW}) by lithographic control of the waveguide mode effective area. The data are taken for a pulse energy at the dispersive wave generation threshold. The solid line is the phase matching condition obtained from FEM simulations. (b) Scatter plot of measured conversion efficiency (left axis) and dispersive-wave average power (right axis) versus the dispersive wave peak wavelength for the waveguide array in Figure 6.8. Blue and red markers correspond to the TM mode and the TE mode. The coupled pulse energy is 1000 pJ.

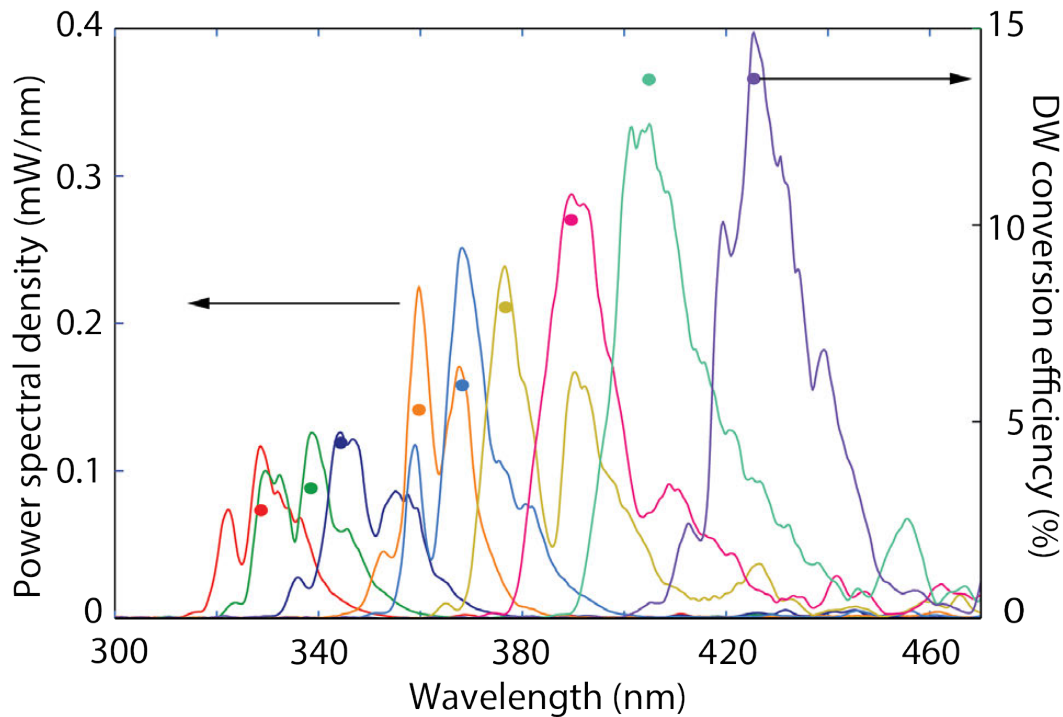


Figure 6.14: **Measured UV dispersive wave spectra and the conversion efficiency.** The TM mode dispersive wave spectra (lines) and the conversion efficiency (solid circles) are shown for the waveguides of various mode area in a waveguide array chip with the under layer thickness 310 nm

fallen to 5% of the maximum value.

Practicality of UV generation using silica ridge waveguides : current status and prospects

As mentioned in the introduction to the chapter, waveguide-based continuum generation has not been performed in the UV band previously. The generation of coherent and wavelength-selected UV light can be potentially very useful for many applications including optical clock technology and quantum manipulation of atoms and ions. For the silica ridge waveguide to be practical as a UV generating device, however, some key device qualities need to be confirmed: reliability and efficiency. It has been reported that silica-based fibers suffer from degradation due to UV-induced color center formation and solarization. To test whether our silica ridge waveguide has a similar problem upon UV exposure, a continuous measurement of UV power generated from the waveguide was performed. For a waveguide generating deep UV light with wavelength below 350 nm, a deformation was observed when the launched pulse energy was around 1 nJ. The waveguide was laterally bent with the

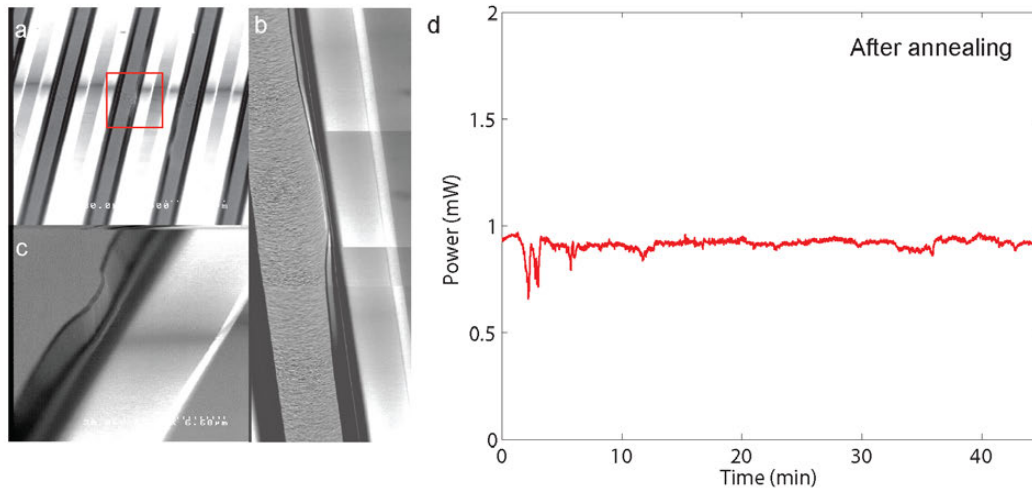


Figure 6.15: **Waveguide deformation and its remedy by annealing (a-c)** SEM images showing the deformation at the position where soliton fission point occurs. The waveguide of mode area $0.86 \mu\text{m}^2$ was used and the dispersive wave peak was located at 345 nm. **(d)** Continuous measurement of UV power generated from an annealed waveguide of similar dimension as in **a-c**. A fresh waveguide without deformation was annealed at 1000 degree for 24 hr. The average coupled power was 41 mW.

base silica layer wrapping up around the ridge near the soliton fission point as shown in Figure 6.15a. A possible cause of the deformation is heat. The increased peak power due to the soliton compression and the small mode area contribute to the high optical intensity at the position at which the soliton fission occurs. This can induce a thermal stress, which then leads to the deformation of the waveguide[47]. To resolve this issue, we tried annealing a fresh waveguide of mode area $0.86 \mu\text{m}^2$ and length 0.80 cm with nitrogen gas for 24 hr. After the annealing, the waveguide remained intact without a deformation after a pulse of the same pulse energy was launched. The result of a continuous UV power measurement is shown in Figure 6.15b.

In the silica ridge waveguide of mode area $1.03 \mu\text{m}^2$, up to 4.8 mW in UV dispersive wave was measured. This is among the largest values for directly measured power in UV part of supercontinuum without using gas molecules reported in literature. As a comparison, the NKT's commercial supercontinuum laser with UV extension unit (SuperK EXTEND-UV) produces light in UV, but the reported power is less than $200 \mu\text{W}$ ($3\text{-}30 \mu\text{W}$ at 260-350 nm and $70\text{-}170 \mu\text{W}$ at 350-480 nm). That unit uses a second harmonic generation stage to generate the UV light. Another direct measurement of UV power is reported by Tu *et. al.*[171]. Here, the authors

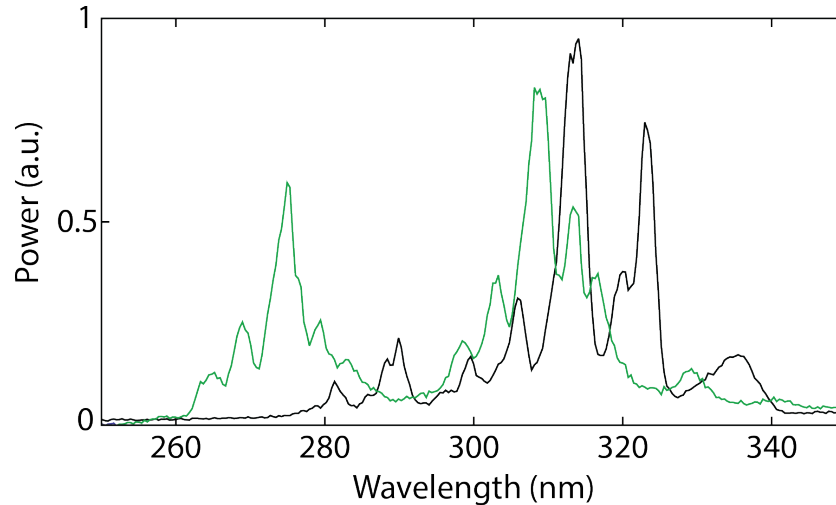


Figure 6.16: **265 nm generation.** Measured dispersive wave spectra in deep UV when the Yb laser pulse is launched into the TM mode of 0.75 cm-long ridge waveguides having mode areas of $1.09 \mu\text{m}^2$ (green) and $1.12 \mu\text{m}^2$ (black). The coupled pulse energy is 2000 pJ.

measured 3.1 mW of the dispersive wave centered at 348 nm. Therefore, the silica waveguide is a promising platform for applications requiring milliwatt level UV light.

Nevertheless, a sudden drop in the dispersive wave conversion efficiency with decreasing dispersive wave peak wavelength is observed in the UV band. (See Figure 6.13b) This observation is consistent in all the waveguide array chips tested. The power spectral density and conversion efficiency of dispersive waves generated using another waveguide array chip (the under-layer thickness 310 nm) are presented in Figure 6.14. The drop in the efficiency at deep UV wavelengths does not agree with the numerical simulations which predicts that the efficiency should still be around 10%. The exact cause is yet to be found. If it is an existence of impurities in the silica ridge surface, surface passivation might mitigate the effect. Resolving this issue will be a critical advance towards the important applications of the silica ridge waveguides.

Using the Yb laser emission at 1064 nm, it was also possible to investigate even deeper UV dispersive wave generation below 300 nm. This observation is consistent with the phase-matching condition for dispersive wave generation (See Supplementary 6.6). Figure 6.16 shows supercontinuum spectra measured in the TM mode of two waveguides having cross-sectional areas of $1.09 \mu\text{m}^2$ and $1.12 \mu\text{m}^2$ using a

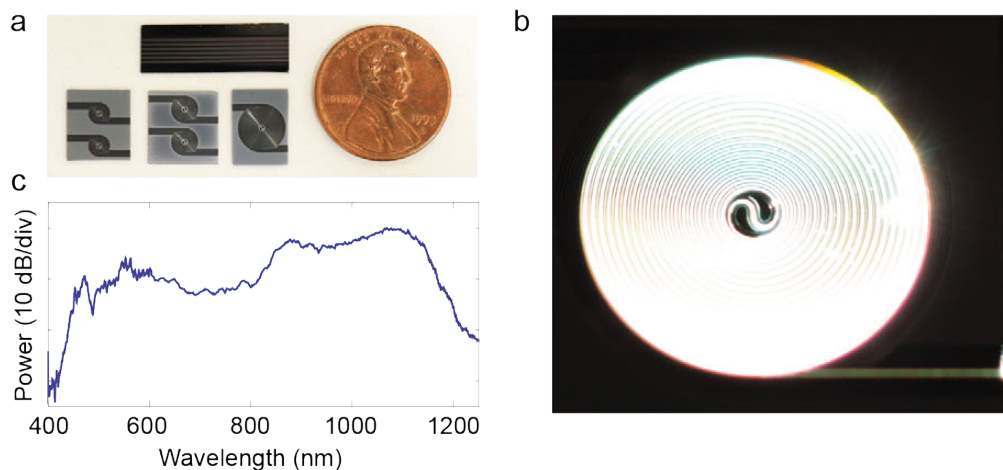


Figure 6.17: **Spiral silica ridge waveguides.** (a) Photographs of silica ridge waveguides of various lengths (from the bottom left to the bottom right: 10 cm, 15 cm, 40 cm). (b) Photograph of a 40 cm-long spiral ridge waveguide generating a white-light supercontinuum. (c) The spectrum of the generated supercontinuum using the device shown in b.

coupled pulse energy of approximately 2000 pJ. The spectra feature multiple peaks due to soliton breathing and subsequent dispersive wave emission. The shortest wavelength edge of the spectrum is nearly 265 nm for the case of the waveguide with mode area $1.09 \mu\text{m}^2$.

6.7 Summary

A silicon chip based waveguide array has been applied to generate UV to visible light by conversion of an input pulse into a dispersive wave. The dispersive wave emission wavelength is precisely tuned from UV to visible by lithographic control of the waveguide dimensions. Generation of UV emission as short as 265 nm has been demonstrated. The measured and predicted dispersive wave emission wavelengths are in excellent agreement. Arrays-on-a-chip containing hundreds of waveguides are easily fabricated and provide ready access to a range of emission wavelengths using a single pump laser. This chip-based tuning control allows for optimization of emission for spectroscopy and metrology using a single device. As a demonstration, offset frequency generation in a Yb mode-locked laser frequency comb was demonstrated by designing a waveguide to generate a dispersive wave that is optimally matched to the second harmonic of the original $1 \mu\text{m}$ comb. Significantly,

this demonstration also confirms the high coherence of the dispersive wave generated by these waveguides. Moreover, the ability to tailor the chip length to provide walk-off-free self-referencing was demonstrated. Monolithic waveguide arrays for wide-band coherent optical generation (up to two octaves) provide a new capability for integration with other optical elements on a chip and can also find application in other areas including bioimaging.

Finally, octave-span supercontinuum generation with input pulse energy as low as 100 pJ is, in principle, possible using a silica ridge waveguide tens of centimeters long. The waveguide can be fabricated in a spiral format to reduce the device footprint as shown in Figure 6.17. Further work to reduce the waveguide loss from mode leakage is required to make the spiral ridge waveguide a viable device.

BIBLIOGRAPHY

- [1] B. Bloom, T. Nicholson, J. Williams, S. Campbell, M. Bishof, X. Zhang, W. Zhang, S. Bromley, and J. Ye. “An optical lattice clock with accuracy and stability at the 10^{-18} level”. In: *arXiv preprint arXiv:1309.1137* (2013).
- [2] S. A. Diddams, D. J. Jones, J. Ye, S. T. Cundiff, J. L. Hall, J. K. Ranka, R. S. Windeler, R. Holzwarth, T. Udem, and T. Hänsch. “Direct link between microwave and optical frequencies with a 300 THz femtosecond laser comb”. In: *Physical Review Letters* 84.22 (2000), pp. 5102–5105.
- [3] T. Steinmetz, T. Wilken, C. Araujo-Hauck, R. Holzwarth, T. W. Hänsch, L. Pasquini, A. Manescau, S. D’odorico, M. T. Murphy, T. Kentischer, et al. “Laser frequency combs for astronomical observations”. In: *Science* 321.5894 (2008), pp. 1335–1337.
- [4] M. Lezius, T. Wilken, C. Deutsch, M. Giunta, O. Mandel, A. Thaller, V. Schkolnik, M. Schiemangk, A. Dinkelaker, A. Kohfeldt, et al. “Space-borne frequency comb metrology”. In: *Optica* 3.12 (2016), pp. 1381–1387.
- [5] P. Marin-Palomo, J. N. Kemal, M. Karpov, A. Kordts, J. Pfeifle, M. H. Pfeiffer, P. Trocha, S. Wolf, V. Brasch, M. H. Anderson, et al. “Microresonator-based solitons for massively parallel coherent optical communications”. In: *Nature* 546.7657 (2017), pp. 274–279.
- [6] R. W. Boyd. “Nonlinear optics”. In: *Handbook of Laser Technology and Applications (Three-Volume Set)*. Academic Press, 2008, pp. 1–613.
- [7] K. J. Vahala. “Optical microcavities”. In: *Nature* 424.6950 (2003), pp. 839–846.
- [8] T. J. Kippenberg, R. Holzwarth, and S. A. Diddams. “Microresonator-based optical frequency combs”. In: *Science* 332.6029 (2011), pp. 555–559.
- [9] S. B. Papp, K. Beha, P. Del’Haye, F. Quinlan, H. Lee, K. J. Vahala, and S. A. Diddams. “Microresonator frequency comb optical clock”. In: *Optica* 1.1 (2014), pp. 10–14.
- [10] F. Vollmer and S. Arnold. “Whispering-gallery-mode biosensing: label-free detection down to single molecules”. In: *Nature Methods* 5.7 (2008), pp. 591–596.
- [11] T. Lu, H. Lee, T. Chen, S. Herchak, J.-H. Kim, S. E. Fraser, R. C. Flagan, and K. Vahala. “High sensitivity nanoparticle detection using optical microcavities”. In: *Proceedings of the National Academy of Sciences* 108.15 (2011), pp. 5976–5979.
- [12] F. Vollmer and L. Yang. “Label-free detection with high-Q microcavities: a review of biosensing mechanisms for integrated devices”. In: *Nanophotonics* 1.3-4 (2012), pp. 267–291.

- [13] H. J. Kimble. “The quantum internet”. In: *Nature* 453.7198 (2008), pp. 1023–1030.
- [14] T. J. Kippenberg and K. J. Vahala. “Cavity optomechanics: back-action at the mesoscale”. In: *Science* 321.5893 (2008), pp. 1172–1176.
- [15] F. Dell’Olio, T. Tatoli, C. Ciminelli, and M. Armenise. “Recent advances in miniaturized optical gyroscopes”. In: *Journal of the European Optical Society - Rapid publications* 9 (2014).
- [16] J. Li, M.-G. Suh, and K. Vahala. “Microresonator Brillouin gyroscope”. In: *Optica* 4.3 (Mar. 2017), pp. 346–348.
- [17] W. Liang, V. S. Ilchenko, A. A. Savchenkov, E. Dale, D. Eliyahu, A. B. Matsko, and L. Maleki. “Resonant microphotonic gyroscope”. In: *Optica* 4.1 (2017), pp. 114–117.
- [18] L. Maleki. “Sources: The optoelectronic oscillator”. In: *Nature Photonics* 5.12 (2011), p. 728.
- [19] J. Li, H. Lee, and K. J. Vahala. “Microwave synthesizer using an on-chip Brillouin oscillator”. In: *Nature Communications* 4 (2013).
- [20] J. Li, X. Yi, H. Lee, S. A. Diddams, and K. J. Vahala. “Electro-optical frequency division and stable microwave synthesis”. In: *Science* 345.6194 (2014), pp. 309–313. doi: 10.1126/science.1252909.
- [21] W. Liang, D. Eliyahu, V. S. Ilchenko, A. A. Savchenkov, A. B. Matsko, D. Seidel, and L. Maleki. “High spectral purity Kerr frequency comb radio frequency photonic oscillator”. In: *Nat. Commun.* 6 (2015), p. 7957.
- [22] A. B. Matsko, A. A. Savchenkov, N. Yu, and L. Maleki. “Whispering-gallery-mode resonators as frequency references. I. Fundamental limitations”. In: *J. Opt. Soc. Am. B* 24.6 (June 2007), pp. 1324–1335.
- [23] J. Alnis, A. Schliesser, C. Y. Wang, J. Hofer, T. J. Kippenberg, and T. W. Hänsch. “Thermal-noise-limited crystalline whispering-gallery-mode resonator for laser stabilization”. In: *Phys. Rev. A* 84 (1 July 2011), p. 011804. doi: 10.1103/PhysRevA.84.011804.
- [24] H. Lee, M.-G. Suh, T. Chen, J. Li, S. A. Diddams, and K. J. Vahala. “Spiral resonators for on-chip laser frequency stabilization”. In: *Nature communications* 4 (2013).
- [25] W. Loh, A. A. Green, F. N. Baynes, D. C. Cole, F. J. Quinlan, H. Lee, K. J. Vahala, S. B. Papp, and S. A. Diddams. “Dual-microcavity narrow-linewidth Brillouin laser”. In: *Optica* 2.3 (2015), pp. 225–232.
- [26] P. Del’Haye, A. Schliesser, O. Arcizet, T. Wilken, R. Holzwarth, and T. Kippenberg. “Optical frequency comb generation from a monolithic microresonator”. In: *Nature* 450.7173 (2007), pp. 1214–1217.

- [27] T. Herr, V. Brasch, J. D. Jost, C. Y. Wang, N. M. Kondratiev, M. L. Gorodetsky, and T. J. Kippenberg. “Temporal solitons in optical microresonators”. In: *Nat. Photon.* 8.2 (2014), pp. 145–152.
- [28] X. Yi, Q.-F. Yang, K. Y. Yang, M.-G. Suh, and K. Vahala. “Soliton frequency comb at microwave rates in a high-Q silica microresonator”. In: *Optica* 2.12 (2015), pp. 1078–1085.
- [29] H. Lee, T. Chen, J. Li, K. Y. Yang, S. Jeon, O. Painter, and K. J. Vahala. “Chemically etched ultrahigh-Q wedge-resonator on a silicon chip”. In: *Nature Photonics* 6.6 (2012), pp. 369–373.
- [30] T. J. Kippenberg, S. M. Spillane, and K. J. Vahala. “Kerr-Nonlinearity Optical Parametric Oscillation in an Ultrahigh-Q Toroid Microcavity”. In: *Physical Review Letters* 93 (8 Aug. 2004), p. 083904.
- [31] A. A. Savchenkov, A. B. Matsko, D. Strekalov, M. Mohageg, V. S. Ilchenko, and L. Maleki. “Low Threshold Optical Oscillations in a Whispering Gallery Mode CaF₂ Resonator”. In: *Physical Review Letters* 93 (2004), p. 243905.
- [32] S. Spillane, T. Kippenberg, and K. Vahala. “Ultralow-threshold Raman laser using a spherical dielectric microcavity”. In: *Nature* 415.6872 (2002), pp. 621–623.
- [33] T. Aoki, B. Dayan, E. Wilcut, W. P. Bowen, A. S. Parkins, T. Kippenberg, K. Vahala, and H. Kimble. “Observation of strong coupling between one atom and a monolithic microresonator”. In: *Nature* 443.7112 (2006), pp. 671–674.
- [34] A. A. Savchenkov, A. B. Matsko, V. S. Ilchenko, and L. Maleki. “Optical resonators with ten million finesse”. In: *Optics Express* 15.11 (2007), pp. 6768–6773.
- [35] I. S. Grudin, V. S. Ilchenko, and L. Maleki. “Ultrahigh optical Q factors of crystalline resonators in the linear regime”. In: *Physical Review A* 74.6 (2006), p. 063806.
- [36] C. Lecaplain, C. Javerzac-Galy, M. Gorodetsky, and T. Kippenberg. “Mid-Infrared ultra-high-Q resonators based on fluoride crystalline materials”. In: *Nature Communications* 7 (2016).
- [37] M. L. Gorodetsky, A. A. Savchenkov, and V. S. Ilchenko. “Ultimate Q of optical microsphere resonators”. In: *Optics Letters* 21.7 (1996), pp. 453–455.
- [38] P. Del’Haye, S. A. Diddams, and S. B. Papp. “Laser-machined ultra-high-Q microrod resonators for nonlinear optics”. In: *Applied Physics Letters* 102.22 (2013), p. 221119.
- [39] D. Armani, T. Kippenberg, S. Spillane, and K. Vahala. “Ultra-high-Q toroid microcavity on a chip”. In: *Nature* 421.6926 (2003), pp. 925–928.

- [40] D. T. Spencer, J. F. Bauters, M. J. Heck, and J. E. Bowers. “Integrated waveguide coupled Si₃N₄ resonators in the ultrahigh-Q regime”. In: *Optica* 1.3 (2014), pp. 153–157.
- [41] X. Ji, F. A. Barbosa, S. P. Roberts, A. Dutt, J. Cardenas, Y. Okawachi, A. Bryant, A. L. Gaeta, and M. Lipson. “Breaking the Loss Limitation of On-chip High-confinement Resonators”. In: *arXiv preprint arXiv:1609.08699* (2016).
- [42] Y. Xuan, Y. Liu, L. T. Varghese, A. J. Metcalf, X. Xue, P.-H. Wang, K. Han, J. A. Jaramillo-Villegas, A. Al Noman, C. Wang, et al. “High-Q silicon nitride microresonators exhibiting low-power frequency comb initiation”. In: *Optica* 3.11 (2016), pp. 1171–1180.
- [43] M. H. Pfeiffer, A. Kordts, V. Brasch, M. Zervas, M. Geiselmann, J. D. Jost, and T. J. Kippenberg. “Photonic Damascene process for integrated high-Q microresonator based nonlinear photonics”. In: *Optica* 3.1 (2016), pp. 20–25.
- [44] A. Naiman, B. Desiatov, L. Stern, N. Mazurski, J. Shappir, and U. Levy. “Ultrahigh-Q silicon resonators in a planarized local oxidation of silicon platform”. In: *Optics letters* 40.9 (2015), pp. 1892–1895.
- [45] M. Borselli, T. J. Johnson, and O. Painter. “Beyond the Rayleigh scattering limit in high-Q silicon microdisks: theory and experiment”. In: *Optics express* 13.5 (2005), pp. 1515–1530.
- [46] H. Lee, T. Chen, J. Li, O. Painter, and K. J. Vahala. “Ultra-low-loss optical delay line on a silicon chip”. In: *Nature communications* 3 (2012), p. 867.
- [47] T. Chen, H. Lee, and K. J. Vahala. “Thermal stress in silica-on-silicon disk resonators”. In: *Applied Physics Letters* 102.3 (2013), p. 031113.
- [48] M. H. Pfeiffer, J. Liu, M. Geiselmann, and T. J. Kippenberg. “Coupling ideality of integrated planar high-Q microresonators”. In: *Physical Review Applied* 7.2 (2017), p. 024026.
- [49] S. M. Spillane, T. J. Kippenberg, O. J. Painter, and V. K. J. “Ideality in a Fiber-Taper-Coupled Microresonator System for Application to Cavity Quantum Electrodynamics”. In: *Physical Review Letters* 91 (2003), p. 043902.
- [50] G. E. McGuire. *Semiconductor materials and process technology handbook*. William Andrew, 1988.
- [51] V. R. Almeida, R. R. Panepucci, and M. Lipson. “Nanotaper for compact mode conversion”. In: *Optics letters* 28.15 (2003), pp. 1302–1304.
- [52] D. T. Spencer et al. “Towards an Integrated-Photonics Optical-Frequency Synthesizer With <1 Hz Residual Frequency Noise”. In: *Optical Fiber Communication Conference*. 2017, M2J.2.

- [53] M. Soltani, A. Matsko, and L. Maleki. “Enabling arbitrary wavelength frequency combs on chip”. In: *Laser & Photonics Reviews* 10.1 (2016), pp. 158–162.
- [54] I. Frank et al. “A low-power, chip-scale optical atomic clock with enhanced stability”. In: *Joint Navigation Conference*. 2017.
- [55] M.-G. Suh, Q.-F. Yang, K. Y. Yang, X. Yi, and K. J. Vahala. “Microresonator soliton dual-comb spectroscopy”. In: *Science* 354.6312 (2016), pp. 600–603.
- [56] A. Dutt, C. Joshi, X. Ji, J. Cardenas, Y. Okawachi, K. Luke, A. L. Gaeta, and M. Lipson. “On-chip dual comb source for spectroscopy”. In: *arXiv preprint arXiv:1611.07673* (2016).
- [57] N. Pavlov, G. Lihachev, S. Koptyaev, E. Lucas, M. Karpov, N. Kondratiev, I. Bilenko, T. Kippenberg, and M. Gorodetsky. “Soliton dual frequency combs in crystalline microresonators”. In: *Optics Letters* 42.3 (2017), pp. 514–517.
- [58] V. Brasch, M. Geiselmann, T. Herr, G. Lihachev, M. Pfeiffer, M. Gorodetsky, and T. Kippenberg. “Photonic chip-based optical frequency comb using soliton Cherenkov radiation”. In: *Science* 351.6271 (2016), pp. 357–360.
- [59] C. Joshi, J. K. Jang, K. Luke, X. Ji, S. A. Miller, A. Klenner, Y. Okawachi, M. Lipson, and A. L. Gaeta. “Thermally controlled comb generation and soliton modelocking in microresonators”. In: *Optics Letters* 41.11 (2016), pp. 2565–2568.
- [60] P.-H. Wang, J. A. Jaramillo-Villegas, Y. Xuan, X. Xue, C. Bao, D. E. Leaird, M. Qi, and A. M. Weiner. “Intracavity characterization of micro-comb generation in the single-soliton regime”. In: *Optics Express* 24.10 (2016), pp. 10890–10897.
- [61] C. Xiong, W. H. Pernice, X. Sun, C. Schuck, K. Y. Fong, and H. X. Tang. “Aluminum nitride as a new material for chip-scale optomechanics and nonlinear optics”. In: *New Journal of Physics* 14.9 (2012), p. 095014.
- [62] D. J. Moss, R. Morandotti, A. L. Gaeta, and M. Lipson. “New CMOS-compatible platforms based on silicon nitride and Hydex for nonlinear optics”. In: *Nature Photonics* 7.8 (2013), pp. 597–607.
- [63] B. Hausmann, I. Bulu, V. Venkataraman, P. Deotare, and M. Lončar. “Diamond nonlinear photonics”. In: *Nature Photonics* 8.5 (2014), pp. 369–374.
- [64] X. Lu, J. Y. Lee, and Q. Lin. “High-frequency and high-quality silicon carbide optomechanical microresonators”. In: *Scientific Reports* 5 (2015), p. 17005.
- [65] X. Lu, S. Rogers, T. Gerrits, W. C. Jiang, S. W. Nam, and Q. Lin. “Heralding single photons from a high-Q silicon microdisk”. In: *Optica* 3.12 (2016), pp. 1331–1338.

- [66] J. S. Levy, A. Gondarenko, M. A. Foster, A. C. Turner-Foster, A. L. Gaeta, and M. Lipson. “CMOS-compatible multiple-wavelength oscillator for on-chip optical interconnects”. In: *Nature photonics* 4.1 (2010), pp. 37–40.
- [67] H. Jung, C. Xiong, K. Y. Fong, X. Zhang, and H. X. Tang. “Optical frequency comb generation from aluminum nitride microring resonator”. In: *Optics letters* 38.15 (2013), pp. 2810–2813.
- [68] X. Ji, F. A. S. Barbosa, S. P. Roberts, A. Dutt, J. Cardenas, Y. Okawachi, A. Bryant, A. L. Gaeta, and M. Lipson. “Ultra-low-loss on-chip resonators with sub-milliwatt parametric oscillation threshold”. In: *Optica* 4.6 (June 2017), pp. 619–624.
- [69] S. B. Papp and S. A. Diddams. “Spectral and temporal characterization of a fused-quartz-microresonator optical frequency comb”. In: *Physical Review A* 84.5 (2011), p. 053833.
- [70] M. Cai, O. Painter, and K. J. Vahala. “Observation of Critical Coupling in a Fiber Taper to a Silica-Microsphere Whispering-Gallery Mode System”. In: *Physical Review Letters* 85 (1 July 2000), pp. 74–77.
- [71] D. J. Jones, S. A. Diddams, J. K. Ranka, A. Stentz, R. S. Windeler, J. L. Hall, and S. T. Cundiff. “Carrier-Envelope Phase Control of Femtosecond Mode-Locked Lasers and Direct Optical Frequency Synthesis”. In: *Science* 288 (2000), p. 635.
- [72] Q. Li, T. C. Briles, D. A. Westly, T. E. Drake, J. R. Stone, B. R. Ilic, S. A. Diddams, S. B. Papp, and K. Srinivasan. “Stably accessing octave-spanning microresonator frequency combs in the soliton regime”. In: *arXiv preprint arXiv:1611.09229* (2016).
- [73] M. H. Pfeiffer, C. Herkommer, J. Liu, H. Guo, M. Karpov, E. Lucas, M. Zervas, and T. J. Kippenberg. “Octave-spanning dissipative Kerr soliton frequency combs in Si_3N_4 microresonators”. In: *arXiv preprint arXiv:1701.08594* (2017).
- [74] J. Li, H. Lee, T. Chen, and K. J. Vahala. “Characterization of a high coherence, Brillouin microcavity laser on silicon”. In: *Optics express* 20.18 (2012), pp. 20170–20180.
- [75] M. L. Gorodetsky and I. S. Grudinin. “Fundamental thermal fluctuations in microspheres”. In: *J. Opt. Soc. Am. B* 21.4 (Apr. 2004), pp. 697–705.
- [76] A. B. Matsko and L. Maleki. “On timing jitter of mode locked Kerr frequency combs”. In: *Opt. Express* 21.23 (Nov. 2013), pp. 28862–28876.
- [77] X. Yi, Q.-F. Yang, X. Zhang, K. Y. Yang, X. Li, and K. Vahala. “Single-mode dispersive waves and soliton microcomb dynamics”. In: *Nat. Commun.* 8 (2017), p. 14869.

- [78] X. Yi, Q.-F. Yang, K. Y. Yang, and K. Vahala. “Active capture and stabilization of temporal solitons in microresonators”. In: *Optics Letters* 41.9 (2016), pp. 2037–2040.
- [79] B. J. Eggleton, C. G. Poulton, and R. Pant. “Inducing and harnessing stimulated Brillouin scattering in photonic integrated circuits”. In: *Advances in Optics and Photonics* 5.4 (2013), pp. 536–587.
- [80] M. Tomes and T. Carmon. “Photonic micro-electromechanical systems vibrating at X-band (11-GHz) rates”. In: *Physical Review Letters* 102.11 (2009), p. 113601.
- [81] I. S. Grudinin, A. B. Matsko, and L. Maleki. “Brillouin lasing with a CaF₂ whispering gallery mode resonator”. In: *Physical review letters* 102.4 (2009), p. 043902.
- [82] N. T. Otterstrom, R. O. Behunin, E. A. Kittlaus, Z. Wang, and P. T. Rakich. “A silicon Brillouin laser”. In: *ArXiv e-prints* (May 2017). arXiv: 1705.05813 [physics.optics].
- [83] B. Morrison, A. Casas-Bedoya, G. Ren, K. Vu, Y. Liu, A. Zarifi, T. Nguyen, D. Choi, D. Marpaung, S. Madden, et al. “Compact Brillouin devices through hybrid integration on Silicon”. In: *arXiv preprint arXiv:1702.05233* (2017).
- [84] J. Li, H. Lee, and K. J. Vahala. “Microwave synthesizer using an on-chip Brillouin oscillator”. In: *Nature communications* 4 (2013).
- [85] V. Brasch, M. Geiselmann, T. Herr, G. Lihachev, M. Pfeiffer, M. Gorodetsky, and T. Kippenberg. “Photonic chip-based optical frequency comb using soliton Cherenkov radiation”. In: *Science* 351.6271 (2016), pp. 357–360.
- [86] Q.-F. Yang, X. Yi, K. Y. Yang, and K. Vahala. “Stokes solitons in optical microcavities”. In: *Nature Physics* 13 (2017), pp. 53–57.
- [87] S. B. Papp and S. A. Diddams. “Spectral and temporal characterization of a fused-quartz-microresonator optical frequency comb”. In: *Physical Review A* 84.5 (2011), p. 053833.
- [88] Q. Li, T. C. Briles, D. A. Westly, T. E. Drake, J. R. Stone, B. R. Ilic, S. A. Diddams, S. B. Papp, and K. Srinivasan. “Stably accessing octave-spanning microresonator frequency combs in the soliton regime”. In: *Optica* 4.2 (2017), pp. 193–203.
- [89] K. Luke, Y. Okawachi, M. R. Lamont, A. L. Gaeta, and M. Lipson. “Broadband mid-infrared frequency comb generation in a Si₃N₄ microresonator”. In: *Optics Letters* 40.21 (2015), pp. 4823–4826.
- [90] A. A. Savchenkov, V. S. Ilchenko, F. Di Teodoro, P. M. Belden, W. T. Lotshaw, A. B. Matsko, and L. Maleki. “Generation of Kerr combs centered at 4.5 μm in crystalline microresonators pumped with quantum-cascade lasers”. In: *Optics Letters* 40.15 (2015), pp. 3468–3471.

- [91] M. Yu, Y. Okawachi, A. G. Griffith, M. Lipson, and A. L. Gaeta. “Mode-locked mid-infrared frequency combs in a silicon microresonator”. In: *Optica* 3.8 (2016), pp. 854–860.
- [92] A. Hugi, G. Villares, S. Blaser, H. Liu, and J. Faist. “Mid-infrared frequency comb based on a quantum cascade laser”. In: *Nature* 492.7428 (2012), pp. 229–233.
- [93] A. D. Ludlow, M. M. Boyd, J. Ye, E. Peik, and P. O. Schmidt. “Optical atomic clocks”. In: *Reviews of Modern Physics* 87.2 (2015), p. 637.
- [94] F. Nez, F. Biraben, R. Felder, and Y. Millerioux. “Optical frequency determination of the hyperfine components of the $5S_{1/2}$ - $5D_{3/2}$ two-photon transitions in rubidium”. In: *Optics Communications* 102.5,6 (1993), pp. 432–438.
- [95] S.-J. Lee, B. Widiyatmoko, M. Kouroggi, and M. Ohtsu. “Ultrahigh scanning speed optical coherence tomography using optical frequency comb generators”. In: *Japanese Journal of Applied Physics* 40.8B (2001), p. L878.
- [96] S. Kray, F. Spöler, M. Först, and H. Kurz. “Dual femtosecond laser multi-heterodyne optical coherence tomography”. In: *Optics Letters* 33.18 (2008), pp. 2092–2094.
- [97] T. Bajraszewski, M. Wojtkowski, M. Szkulmowski, A. Szkulmowska, R. Huber, and A. Kowalczyk. “Improved spectral optical coherence tomography using optical frequency comb”. In: *Optics Express* 16.6 (2008), pp. 4163–4176.
- [98] K. Saha, Y. Okawachi, J. S. Levy, R. K. Lau, K. Luke, M. A. Foster, M. Lipson, and A. L. Gaeta. “Broadband parametric frequency comb generation with a 1- μm pump source”. In: *Optics Express* 20.24 (2012), pp. 26935–26941.
- [99] X. Xue, F. Leo, Y. Xuan, J. A. Jaramillo-Villegas, P.-H. Wang, D. E. Leaird, M. Erkintalo, M. Qi, and A. M. Weiner. “Second-harmonic-assisted four-wave mixing in chip-based microresonator frequency comb generation”. In: *Light: Science & Applications* 6 (Apr. 2017), e16253.
- [100] H. Jung, R. Stoll, X. Guo, D. Fischer, and H. X. Tang. “Green, red, and IR frequency comb line generation from single IR pump in AlN microring resonator”. In: *Optica* 1.6 (2014), pp. 396–399.
- [101] L. Wang, L. Chang, N. Volet, M. H. Pfeiffer, M. Zervas, H. Guo, T. J. Kippenberg, and J. E. Bowers. “Frequency comb generation in the green using silicon nitride microresonators”. In: *Laser & Photonics Reviews* 10.4 (2016), pp. 631–638.
- [102] A. Savchenkov, A. Matsko, W. Liang, V. Ilchenko, D. Seidel, and L. Maleki. “Kerr combs with selectable central frequency”. In: *Nature Photonics* 5.5 (2011), pp. 293–296.

- [103] Y. Yang, X. Jiang, S. Kasumie, G. Zhao, L. Xu, J. M. Ward, L. Yang, and S. N. Chormaic. “Four-wave mixing parametric oscillation and frequency comb generation at visible wavelengths in a silica microbubble resonator”. In: *Optics Letters* 41.22 (2016), pp. 5266–5269.
- [104] J. Riemensberger, K. Hartinger, T. Herr, V. Brasch, R. Holzwarth, and T. J. Kippenberg. “Dispersion engineering of thick high-Q silicon nitride ring-resonators via atomic layer deposition”. In: *Optics Express* 20.25 (2012), pp. 27661–27669.
- [105] Y. Okawachi, M. R. Lamont, K. Luke, D. O. Carvalho, M. Yu, M. Lipson, and A. L. Gaeta. “Bandwidth shaping of microresonator-based frequency combs via dispersion engineering”. In: *Optics Letters* 39.12 (2014), pp. 3535–3538.
- [106] Y. Liu, Y. Xuan, X. Xue, P.-H. Wang, S. Chen, A. J. Metcalf, J. Wang, D. E. Leaird, M. Qi, and A. M. Weiner. “Investigation of mode coupling in normal-dispersion silicon nitride microresonators for Kerr frequency comb generation”. In: *Optica* 1.3 (2014), pp. 137–144.
- [107] S. Ramelow, A. Farsi, S. Clemmen, J. S. Levy, A. R. Johnson, Y. Okawachi, M. R. E. Lamont, M. Lipson, and A. L. Gaeta. “Strong polarization mode coupling in microresonators”. In: *Optics Letters* 39.17 (Sept. 2014), pp. 5134–5137.
- [108] I. S. Grudinin and N. Yu. “Dispersion engineering of crystalline resonators via microstructuring”. In: *Optica* 2.3 (2015), pp. 221–224.
- [109] K. Y. Yang, K. Beha, D. C. Cole, X. Yi, P. Del’Haye, H. Lee, J. Li, D. Y. Oh, S. A. Diddams, S. B. Papp, et al. “Broadband dispersion-engineered microresonator on a chip”. In: *Nature Photonics* 10.5 (2016), pp. 316–320.
- [110] D. Y. Oh, K. Y. Yang, C. Fredrick, G. Ycas, S. A. Diddams, and K. J. Vahala. “Coherent ultra-violet to near-infrared generation in silica ridge waveguides”. In: *Nature Communications* 8 (2017), p. 13922. doi: 10.1038/ncomms13922.
- [111] D. J. Moss, R. Morandotti, A. L. Gaeta, and M. Lipson. “New CMOS-compatible platforms based on silicon nitride and Hydex for nonlinear optics”. In: *Nature Photonics* 7.8 (2013), pp. 597–607.
- [112] K. Y. Yang, D. Y. Oh, S. H. Lee, Q.-F. Yang, X. Yi, and K. Vahala. “Integrated ultra-high-Q optical resonator”. In: *ArXiv e-prints* (Feb. 2017). arXiv: 1702.05076 [physics.optics].
- [113] I. Malitson. “Interspecimen Comparison of the Refractive Index of Fused Silica”. In: *J. Opt. Soc. Am.* 55.10 (1965), pp. 1205–1209.
- [114] C. Milián, A. V. Gorbach, M. Taki, A. V. Yulin, and D. V. Skryabin. “Solitons and frequency combs in silica microring resonators: Interplay of the Raman and higher-order dispersion effects”. In: *Physical Review A* 92.3 (2015), p. 033851.

- [115] M. Karpov, H. Guo, A. Kordts, V. Brasch, M. H. Pfeiffer, M. Zervas, M. Geiselmann, and T. J. Kippenberg. “Raman self-frequency shift of dissipative Kerr solitons in an optical microresonator”. In: *Physics Review Letters* 116.10 (2016), p. 103902.
- [116] X. Yi, Q.-F. Yang, K. Y. Yang, and K. Vahala. “Theory and measurement of the soliton self-frequency shift and efficiency in optical microcavities”. In: *Optics Letters* 41.15 (2016), pp. 3419–3422.
- [117] J. R. Stone, T. Briles, T. Drake, D. Spencer, X. Yi, K. Y. Yang, K. Vahala, S. Diddams, and S. Papp. “Initiating Kerr-Soliton Frequency Combs Apart from Thermal Bistability and Mode Perturbation Effects”. In: *Conference on Lasers and Electro-Optics*. 2017, STu4J.4.
- [118] S. A. Miller, Y. Okawachi, S. Ramelow, K. Luke, A. Dutt, A. Farsi, A. L. Gaeta, and M. Lipson. “Tunable frequency combs based on dual microring resonators”. In: *Optics Express* 23.16 (2015), pp. 21527–21540.
- [119] D. Dai and J. E. Bowers. “Novel concept for ultracompact polarization splitter-rotator based on silicon nanowires”. In: *Optics Express* 19.11 (2011), pp. 10940–10949.
- [120] G. P. Agrawal. *Nonlinear fiber optics*. Academic press, 2007.
- [121] J. K. Ranka, R. S. Windeler, and A. J. Stentz. “Optical properties of high-delta air silica microstructure optical fibers”. In: *Opt. Lett.* 25.11 (2000), pp. 796–798.
- [122] P. S. J. Russell. “Photonic crystal fibers”. In: *Science* 299.5605 (2003), pp. 358–362.
- [123] J. M. Dudley, G. Genty, and S. Coen. “Supercontinuum generation in photonic crystal fiber”. In: *Rev. Mod. Phys.* 78.4 (2006), pp. 1135–1184.
- [124] I. Hartl, X. Li, C. Chudoba, R. Ghanta, T. Ko, J. Fujimoto, J. Ranka, and R. Windeler. “Ultrahigh-resolution optical coherence tomography using continuum generation in an air-silica microstructure optical fiber”. In: *Optics letters* 26.9 (2001), pp. 608–610.
- [125] T. Morioka, H. Takara, S. Kawanishi, O. Kamatani, K. Takiguchi, K. Uchiyama, M. Saruwatari, H. Takahashi, M. Yamada, T. Kanamori, et al. “1 Tbit/s (100 Gbit/s/spl times/10 channel) OTDM/WDM transmission using a single supercontinuum WDM source”. In: *Electronics Letters* 32.10 (1996), pp. 906–907.
- [126] S. Kawanishi, H. Takara, K. Uchiyama, I. Shake, and K. Mori. “3 Tbit/s (160 Gbit/s/spl times/19 channel) optical TDM and WDM transmission experiment”. In: *Electronics Letters* 35.10 (1999), pp. 826–827.
- [127] I.-W. Hsieh, X. Chen, X. Liu, J. I. Dadap, N. C. Panoiu, C.-Y. Chou, F. Xia, W. M. Green, Y. A. Vlasov, and R. M. Osgood. “Supercontinuum generation in silicon photonic wires”. In: *Opt. Express* 15.23 (2007), pp. 15242–15249.

- [128] L. Yin, Q. Lin, and G. P. Agrawal. “Soliton fission and supercontinuum generation in silicon waveguides”. In: *Optics letters* 32.4 (2007), pp. 391–393.
- [129] Q. Lin, O. J. Painter, and G. P. Agrawal. “Nonlinear optical phenomena in silicon waveguides: modeling and applications”. In: *Optics Express* 15.25 (2007), pp. 16604–16644.
- [130] M. R. Lamont, B. Luther-Davies, D.-Y. Choi, S. Madden, and B. J. Eggleton. “Supercontinuum generation in dispersion engineered highly nonlinear ($\gamma=10/\text{W/m}$) As_2S_3 chalcogenide planar waveguide”. In: *Opt. Express* 16.19 (2008), pp. 14938–14944.
- [131] A. C. Judge, S. A. Dekker, R. Pant, C. M. de Sterke, and B. J. Eggleton. “Soliton self-frequency shift performance in As_2S_3 waveguides”. In: *Optics express* 18.14 (2010), pp. 14960–14968.
- [132] L. Zhang, Y. Yan, Y. Yue, Q. Lin, O. Painter, R. G. Beausoleil, and A. E. Willner. “On-chip two-octave supercontinuum generation by enhancing self-steepening of optical pulses”. In: *Optics express* 19.12 (2011), pp. 11584–11590.
- [133] R. Halir, Y. Okawachi, J. Levy, M. Foster, M. Lipson, and A. Gaeta. “Ultra-broadband supercontinuum generation in a CMOS-compatible platform”. In: *Optics letters* 37.10 (2012), pp. 1685–1687.
- [134] D. Milam. “Review and assessment of measured values of the nonlinear refractive-index coefficient of fused silica”. In: *Applied optics* 37.3 (1998), pp. 546–550.
- [135] T. Chen, H. Lee, and K. J. Vahala. “Design and characterization of whispering-gallery spiral waveguides”. In: *Optics express* 22.5 (2014), pp. 5196–5208.
- [136] J. M. Dudley and J. R. Taylor. *Supercontinuum generation in optical fibers*. Cambridge University Press, 2010.
- [137] Q. Lin and G. P. Agrawal. “Raman response function for silica fibers”. In: *Optics letters* 31.21 (2006), pp. 3086–3088.
- [138] K. Saha, Y. Okawachi, B. Shim, J. S. Levy, R. Salem, A. R. Johnson, M. A. Foster, M. R. Lamont, M. Lipson, and A. L. Gaeta. “Modelocking and femtosecond pulse generation in chip-based frequency combs”. In: *Opt. Express* 21.1 (2013), pp. 1335–1343.
- [139] M. A. Foster, A. C. Turner, M. Lipson, and A. L. Gaeta. “Nonlinear optics in photonic nanowires”. In: *Opt. Express* 16.2 (2008), pp. 1300–1320.
- [140] D. Y. Oh, D. Sell, H. Lee, K. Y. Yang, S. A. Diddams, and K. J. Vahala. “Supercontinuum generation in an on-chip silica waveguide”. In: *Opt. Lett.* 39.4 (2014), pp. 1046–1048.

- [141] A. R. Johnson et al. “Octave-spanning coherent supercontinuum generation in a silicon nitride waveguide”. In: *Opt. Lett.* 40.21 (2015), pp. 5117–5120.
- [142] F. Leo, J. Safioui, B. Kuyken, G. Roelkens, and S.-P. Gorza. “Generation of coherent supercontinuum in a-Si: H waveguides: experiment and modeling based on measured dispersion profile”. In: *Opt. Express* 22.23 (2014), pp. 28997–29007.
- [143] F. Leo, S.-P. Gorza, S. Coen, B. Kuyken, and G. Roelkens. “Coherent supercontinuum generation in a silicon photonic wire in the telecommunication wavelength range”. In: *Opt. Lett.* 40.1 (2015), pp. 123–126.
- [144] H. Zhao et al. “Visible-to-near-infrared octave spanning supercontinuum generation in a silicon nitride waveguide”. In: *Opt. Lett.* 40.10 (2015), pp. 2177–2180.
- [145] D. D. Hickstein, H. Jung, D. R. Carlson, A. Lind, I. Coddington, K. Srinivasan, G. G. Ycas, D. C. Cole, A. Kowligy, C. Fredrick, et al. “Ultrabroadband supercontinuum generation and frequency-comb stabilization using on-chip waveguides with both cubic and quadratic nonlinearities”. In: *arXiv preprint arXiv:1704.03908* (2017).
- [146] D. Carlson, D. Hickstein, A. Lind, J. Olson, R. Fox, R. Brown, A. Ludlow, Q. Li, D. Westly, H. Leopardi, et al. “Photonic-chip supercontinuum with tailored spectra for precision frequency metrology”. In: *arXiv preprint arXiv:1702.03269* (2017).
- [147] R. K. Lau, M. R. Lamont, A. G. Griffith, Y. Okawachi, M. Lipson, and A. L. Gaeta. “Octave-spanning mid-infrared supercontinuum generation in silicon nanowaveguides”. In: *Opt. Lett.* 39.15 (2014), pp. 4518–4521.
- [148] B. Kuyken, T. Ideguchi, S. Holzner, M. Yan, T. W. Hänsch, J. Van Campenhout, P. Verheyen, S. Coen, F. Leo, R. Baets, et al. “An octave-spanning mid-infrared frequency comb generated in a silicon nanophotonic wire waveguide”. In: *Nat. Commun.* 6 (2015), p. 6310.
- [149] A. S. Mayer, A. Klenner, A. R. Johnson, K. Luke, M. R. E. Lamont, Y. Okawachi, M. Lipson, A. L. Gaeta, and U. Keller. “Frequency comb offset detection using supercontinuum generation in silicon nitride waveguides”. In: *Opt. Express* 23.12 (2015), pp. 15440–15451.
- [150] D. R. Carlson, D. D. Hickstein, A. Lind, S. Droste, D. Westly, N. Nader, I. Coddington, N. R. Newbury, K. Srinivasan, S. A. Diddams, et al. “Self-referenced frequency combs using high-efficiency silicon-nitride waveguides”. In: *Optics Letters* 42.12 (2017), pp. 2314–2317.
- [151] I. Cristiani, R. Tediosi, L. Tartara, and V. Degiorgio. “Dispersive wave generation by solitons in microstructured optical fibers”. In: *Opt. Express* 12.1 (2004), pp. 124–135.

- [152] G. Chang, L.-J. Chen, and F. X. Kärtner. “Highly efficient Cherenkov radiation in photonic crystal fibers for broadband visible wavelength generation”. In: *Opt. Lett.* 35.14 (2010), pp. 2361–2363.
- [153] M. Hu, C.-y. Wang, Y. Li, Z. Wang, L. Chai, and A. Zheltikov. “Multiplex frequency conversion of unamplified 30-fs Ti: sapphire laser pulses by an array of waveguiding wires in a random-hole microstructure fiber”. In: *Opt. Express* 12.25 (2004), pp. 6129–6134.
- [154] S. Stark, J. Travers, and P. S. J. Russell. “Extreme supercontinuum generation to the deep UV”. In: *Opt. Lett.* 37.5 (2012), pp. 770–772.
- [155] X. Jiang, N. Y. Joly, M. A. Finger, F. Babic, G. K. Wong, J. C. Travers, and P. S. J. Russell. “Deep-ultraviolet to mid-infrared supercontinuum generated in solid-core ZBLAN photonic crystal fibre”. In: *Nat. Photon.* 9.2 (2015), pp. 133–139.
- [156] N. Joly, J. Nold, W. Chang, P. Hölzer, A. Nazarkin, G. Wong, F. Biancalana, and P. S. J. Russell. “Bright spatially coherent wavelength-tunable deep-UV laser source using an Ar-filled photonic crystal fiber”. In: *Phys. Rev. Lett.* 106.20 (2011), p. 203901.
- [157] F. Belli, A. Abdolvand, W. Chang, J. C. Travers, and P. S. J. Russell. “Vacuum-ultraviolet to infrared supercontinuum in hydrogen-filled photonic crystal fiber”. In: *Optica* 2.4 (2015), pp. 292–300.
- [158] S. Diddams, T. Udem, J. Bergquist, E. Curtis, R. Drullinger, L. Hollberg, W. Itano, W. Lee, C. Oates, K. Vogel, et al. “An optical clock based on a single trapped $^{199}\text{Hg}^+$ ion”. In: *Science* 293.5531 (2001), pp. 825–828.
- [159] J. Davila-Rodriguez, A. Ozawa, T. W. Hänsch, and T. Udem. “Doppler Cooling Trapped Ions with a UV Frequency Comb”. In: *Phys. Rev. Lett.* 116.4 (2016), p. 043002.
- [160] D. Hayes, D. Matsukevich, P. Maunz, D. Hucul, Q. Quraishi, S. Olmschenk, W. Campbell, J. Mizrahi, C. Senko, and C. Monroe. “Entanglement of atomic qubits using an optical frequency comb”. In: *Phys. Rev. Lett.* 104.14 (2010), p. 140501.
- [161] D. Träutlein, F. Adler, K. Moutzouris, A. Jeromin, A. Leitenstorfer, and E. Ferrando-May. “Highly versatile confocal microscopy system based on a tunable femtosecond Er: fiber source”. In: *J. Biophoton.* 1.1 (2008), pp. 53–61.
- [162] P. K. A. Wai, C. R. Menyuk, Y. C. Lee, and H. H. Chen. “Nonlinear pulse propagation in the neighborhood of the zero-dispersion wavelength of monomode optical fibers”. In: *Opt. Lett.* 11.7 (1986), pp. 464–466.
- [163] N. Akhmediev and M. Karlsson. “Cherenkov radiation emitted by solitons in optical fibers”. In: *Phys. Rev. A* 51.3 (1995), pp. 2602–2607.

- [164] G. Chang, L.-J. Chen, and F. X. Kärtner. “Fiber-optic Cherenkov radiation in the few-cycle regime”. In: *Opt. Express* 19.7 (2011), pp. 6635–6647.
- [165] L. Lepetit, G. Cheriaux, and M. Joffre. “Linear techniques of phase measurement by femtosecond spectral interferometry for applications in spectroscopy”. In: *J. Opt. Soc. Am. B* 12.12 (1995), pp. 2467–2474.
- [166] M. Takeda, H. Ina, and S. Kobayashi. “Fourier-transform method of fringe-pattern analysis for computer-based topography and interferometry”. In: *J. Opt. Soc. Am.* 72.1 (1982), pp. 156–160.
- [167] A. Husakou and J. Herrmann. “Supercontinuum generation of higher-order solitons by fission in photonic crystal fibers”. In: *Phys. Rev. Lett.* 87.20 (2001), p. 203901.
- [168] T. R. Schibli, K. Minoshima, F.-L. Hong, H. Inaba, A. Onae, H. Matsumoto, I. Hartl, and M. E. Fermann. “Frequency metrology with a turnkey all-fiber system”. In: *Opt. Lett.* 29.21 (2004), pp. 2467–2469.
- [169] J.-C. Baumert, P. Günter, and H. Melchior. “High efficiency second-harmonic generation in KNbO₃ crystals”. In: *Opt. Commun.* 48.3 (1983), pp. 215–220.
- [170] B. Zysset, I. Biaggio, and P. Günter. “Refractive indices of orthorhombic KNbO₃. I. Dispersion and temperature dependence”. In: *J. Opt. Soc. Am. B* 9.3 (1992), pp. 380–386.
- [171] H. Tu and S. A. Boppart. “Ultraviolet-visible non-supercontinuum ultrafast source enabled by switching single silicon strand-like photonic crystal fibers”. In: *Opt. Express* 17.20 (2009), pp. 17983–17988.